Spin Electronics in Metallic Nanoparticles

A Thesis
Presented to
The Academic Faculty

by

Felipe Tijiwa Birk

In Partial Fulfillment
of the Requirements for the Degree
Doctor of Philosophy

School of Physics
Georgia Institute of Technology
May 2011

Spin Electronics in Metallic Nanoparticles

Approved by:

Professor Dragomir Davidovic, Adviser
School of Physics
Georgia Institute of Technology

Professor Edward H. Conrad
School of Physics
Georgia Institute of Technology

Professor Phillip N. First
School of Physics
Georgia Institute of Technology

Professor Walter A. de Heer
School of Physics
Georgia Institute of Technology

Professor Christopher J. Summers
School of Materials Science and
Engineering
Georgia Institute of Technology

Date Approved: March, 15, 2011

To my lovely wife,

my wonderful parents,

and my loyal pets.

ACKNOWLEDGMENTS

I am grateful to so many people for their help and support during my PhD journey, that all I can do is to try my best to include every one. First I would like to thank my parents, without whom I would not be here, of course, for providing me with the necessary initial and boundary conditions to become a good human being (which I believe I managed to do). I thank my wife, Sara, for being a true inspiration in all aspects of my life. Without her, I would probably be selling goods on the streets of São Paulo, living under a nice cozy bridge. OK, maybe that was a little too far, but you never know. I would like to thank my advisor, Dr. Dragomir Davidovic, for trusting me with his lab's key. It literally opened the doors to many research project opportunities, which I am very grateful for. Thanks for the help and hard work of previous and current students in our lab, including Liyuan Zhang, Xia Liu, Wenchao Jiang, and specially to Yaguang Wei for his work legacy, and to Chris Malec for sharing his experience and for being such a great lab mate to work with. I thank all my committee members: Dr. Walter de Heer, Dr. Edward Conrad, Dr. Phillip First, and Dr. Christopher Summers, for their time and consideration. I would like to thank Judy Melton for her kindness and helpful "gentle reminders"; to Felicia Goolsby, Lori Federico, Jennifer Fairchild-Pierce, and Samantha King for making hard work look easy; to Vicky Speights, Debby James, and Tia Richardson for solving many financial paperwork for me generated; to Sam Mize and Scott Centers for their valuable technical advices; and to all other School of Physics staff members for their outstanding service, keeping the department always functional. Finally, I thank all my friends for their unconditional friendship and for making me feel at home from the very beginning. They know who they are.

TABLE OF CONTENTS

LIST OF FIGURES

SUMMARY

The work described in this thesis reflects a through investigation of spin-dependent transport through metallic nanoparticles, via tunnel junctions. Our devices consist of metallic nanoparticles embedded in an insulating matrix tunnel coupled to two metallic electrodes. At low temperatures, the small dimensions of the particles provide the necessary conditions to study the role played by discrete energy levels in the transport properties of these devices. In Chapter 1, a brief introduction to some of the relevant background topics related to this work, will be presented. Chapter 2 gives a detailed description of measurement procedures used on the experiments, and the adopted techniques for sample fabrication. In some of the devices presented here, the electrodes are made of ferromagnetic materials, which are used as source of spin-polarized current. The case where both electrodes are ferromagnetic, in a *spin-valve* configuration, will be discussed in Chapter 3, showing that spin accumulation mechanisms are responsible for the observed spin-polarized current. It will also be shown that the effect of an applied perpendicular magnetic field, relative to the magnetization orientation of the electrodes, indicates the suppression of spin precession in such small particles. Moreover, in the presence of an external non-collinear magnetic field, it is the local field "felt" by the particle that determines the character of the tunnel current. Even in samples where only one of the electrodes is ferromagnetic, spin-polarization of the tunnel current due to spin accumulation in the particle is observed. Asymmetries in the current-voltage (IV) characteristics as well as in the tunnel magnetoresistance (TMR) of these devices will be presented in Chapter 4. Another type of device, which will be addressed in Chapter 5, consists of ferromagnetic nanoparticles coupled to normal-metal electrodes. The rich electronic structure as well as a complex set of relaxation mechanisms in these *nanomagnets*, are reflected in their energy spectrum, and magnetic/electric field response. Temperature and voltage dependence of the particle's switching field, indicates

a complex interplay between electronic and magnetic excitations within such small particles. Alternative contributions to magnetic damping in metallic systems, is presented in Appendix A. Finally, Chapter 6 discusses preliminary results of experiments involving microwave-induced switching in ferromagnetic nanoparticles. These results have already shown the promising potential of this powerful technique. By using it as a complementary tool for real time investigations of magnetization dynamics in magnetic nanostructures, a wide range of options for future experiments have been made available.

CHAPTER I

SPIN ELECTRONICS AND NANOPARTICLES

1.1 Introduction

Although the concept of *spin* has been known for almost a century, the building blocks for computer logic (transistors) completely ignore the spin degree of freedom of charge carriers. As advances in nanotechnology continue to allow consistent miniaturization of electronic devices, new technological challenges will certainly arise [97, 98]. Since the discovery of Giant Magnetoresistance (GMR) more than a decade ago, a better control over this "extra" degree of freedom has been extensively pursued, mainly due to the huge potential for practical applications. This emerging field, so-called "spintronics", opens the possibility to create devices with new functionalities, faster switching times, and lower power consumption [97, 78], to name a few of the short term motivations making this research field extremely active and interesting. As an example, the reliability of data storage devices, such as computer hard drives, depends on the ability to maintain thermal stability in small metallic grains [26]. Typical "bits" of information consist of magnetic grains containing $\sim 10^5$ atoms. In order to obtain acceptable control over the physical properties of such small grains, a deeper understanding about the fundamental limits of magnetic mechanisms at the nanoscale, becomes necessary. Although technological applications have been the main driving force behind spintronics, there are numerous theoretical open challenges. The most ambitious ones, make use of spin states as quantum bits (qubits) [34, 62, 21] in single and double quantum dot systems [41]. Therefore, fundamental studies on metallic quantum dots in general, are crucial for further understanding the effects caused by the interplay between spin and charge. In this chapter, relevant topics concerning spin-dependent phenomena will be introduced and used in the arguments throughout subsequent chapters.

1.2 Spin-Dependent Tunneling

Electron tunneling is a quantum mechanical phenomena, corresponding to the finite probability of an electron *tunneling* through an insulating layer, between two metal electrodes. Such a process is classically forbidden, since the incoming electron's energy is lower than the potential energy barrier imposed by the insulating layer (Figure 1a). When a voltage is applied across the tunnel junction, the Fermi level of the electrodes are shifted accordingly, and empty states at one of the electrodes become available for tunneling.

Spin polarized tunneling occurs whenever the physical properties of a tunneling device, allow an imbalance of spin orientations to take place. One way to achieve such imbalance is by choosing a tunnel barrier which act as a *spin filter*, giving transport preference only to a given spin orientation. Another way is to use ferromagnetic electrodes (one or both) as the source of polarized electrons. This approach relies on spin conserving properties of the tunnel barrier, which for the case of Al_2O_3, is a realistic assumption [72].

1.2.1 Tunnel Magnetoresistance

The pioneering works on normal metal-insulator-superconductor tunnel junctions, from Giaever [36] in the late 60's, followed by Meservey and Tedrow [69] in the early 70's, marked the beginning of the new field of spin-polarized tunneling, which holds the fundamental framework behind many spin-dependent effects, including magnetoresistance in magnetic tunnel junctions (MTJ). Meservey and Tedrow cleverly used the Zeeman-split density of states of the superconductor electrode, to probe the conduction electron spin polarization of the second ferromagnetic electrode. In 1975, Julliere [49] was the first to report spin-polarized tunneling on Fe-Ge-Co tunnel junctions. He followed the analysis from Meservey and Tedrow to obtain the conductance of the tunnel junction. The tunneling current is found using Fermi's golden rule, which states that this current is proportional to the product between the density of occupied states in F_1 (at a given energy), and the density of available states on F_2 (at the same energy), multiplied by the matrix element, $|M_{12}|^2$, corresponding to the given transition:

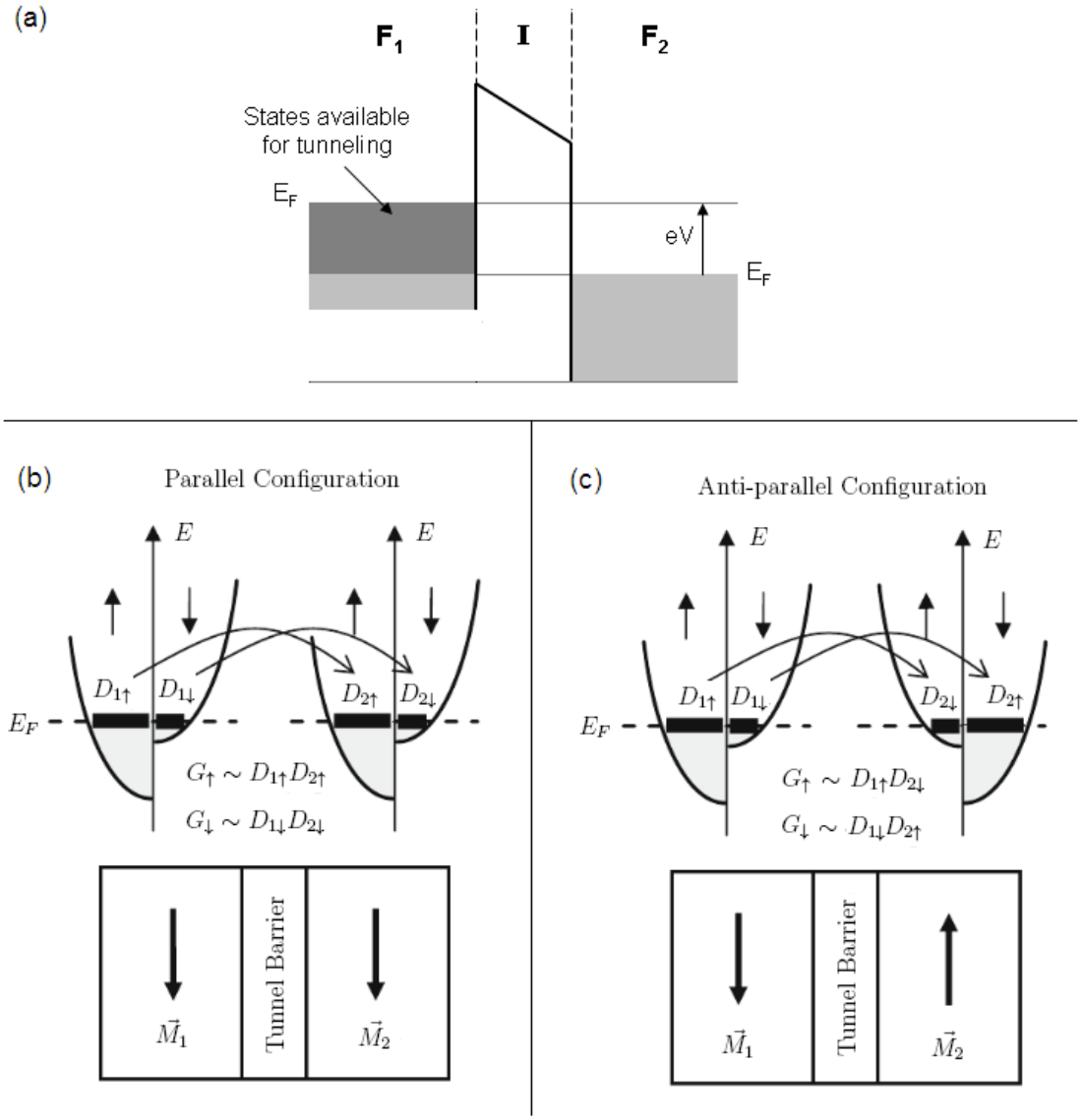

Figure 1: (a) Diagram of a tunnel junction with an applied voltage across two ferromagnetic electrodes separated by a thin insulating layer. (b) Conductances of majority and minority spin channels in the parallel and (c) anti-parallel configurations.

$$I(V) \propto \int_{E_{F_1}}^{E_{F_2}} D_1(E) f_1 \left|M_{12}\right|^2 D_2(E)(1-f_2)\, dE \tag{1}$$

where $D_{1(2)} = D_{1(2)\uparrow} + D_{1(2)\downarrow}$ is the total density of states (majority ($\uparrow$) plus minority ($\downarrow$)) at electrode $F_{1(2)}$, and $f_{1(2)}$ is the Fermi fuction of electrode $F_{1(2)}$: $f = 1/[\exp(E/k_BT)+1]$. Defining the spin polarization of the leads as: $P_{1(2)} = (D_{1(2)\uparrow} - D_{1(2)\downarrow})/(D_{1(2)\uparrow} + D_{1(2)\downarrow})$, it follows that:

$$2D_{1(2)\uparrow} = D_{1(2)}(1 + P_{1(2)}) \tag{2}$$

Now, since the tunneling current depends on the product between densities of states on both electrodes (see Figs. 1b-c), the ratio of conductance change can be expressed in terms of the spin polarization of the electrodes, :

$$\frac{\Delta G}{G_{\uparrow\uparrow}} = \frac{G_{\uparrow\uparrow} - G_{\uparrow\downarrow}}{G_{\uparrow\uparrow}} \propto \frac{D_{1\uparrow}D_{2\uparrow} + D_{1\downarrow}D_{2\downarrow}}{D_{1\uparrow}D_{2\uparrow}} \tag{3}$$

where ΔG is the change in the total conductance from the parallel, $G_{\uparrow\uparrow}$, to the anti-parallel, $G_{\uparrow\downarrow}$ configuration of the ferromagnetic electrodes. Figures 1b-c illustrate the tunneling process in both parallel and anti-parallel configurations. After some algebra, the expression for the TMR takes the form:

$$TMR \equiv \frac{\Delta R}{R_{\downarrow\uparrow}} = \frac{R_{\downarrow\uparrow} - R_{\uparrow\uparrow}}{R_{\downarrow\uparrow}} = \frac{2P_1P_2}{1 + P_1P_2} \tag{4}$$

which is the well known Julliere's formula. Although this model is very good in predicting TMR ratios, it does not include the properties of the tunnel barrier, e.g. barrier height and thickness, solely relying on the properties of the ferromagnetic electrodes [50]. Another limitation of the model is that there is no distinction between electrons within the electrodes,

belonging to different conduction bands, since they can have different effective masses as well as spin polarizations.

1.2.2 Coulomb Blockade

In tunneling systems containing small metallic grains, the energy required to add a single electronic charge may become comparable to other relevant energy scales in the system, such as k_BT and eV. In this regime, tunneling can be suppressed if this charging energy, $E_C = Q^2/2C_\Sigma$, is greater than the thermal or the electropotential energy. Here, C_Σ is the total capacitance of the grain and Q is the charge in it. Usually, the charge Q is written as $Q = Q_0 + ne$, to take into account charge increments in multiples of the electronic charge, e. The background charge, Q_0, reflects the electrostatic environment of the grain and can be conveniently adjusted using a gate electrode. Since our devices do not have a gate, Q_0 will be determined by sample fabrication and experimental conditions. In this case, Q_0 shifts are not uncommon during changes in temperature and bias voltages across the device. At low bias voltages, the total capacitance of such small grains, can be so small that E_C will be large enough to block an additional electron to tunnel into the particle. This regime, where tunneling is suppressed by the charging energy of the grain, is called *Coulomb Blockade* [9, 82] and is illustrated in Figure 2.

The tunnel resistance of granular tunnel junctions depends on the characteristics of the grain. For example, in a normal-metal grain, the current-voltage (IV) curve, will have the form of a staircase, where each plateau corresponds to a different charged state. In a magnetic grain, the tunnel resistance will also depend on the relative orientation of the grain's magnetization with respect to the magnetization of the leads [5]. The tunneling resistances of the samples presented in this work (R) are much larger than the quantum resistance ($R_Q = h/e^2$), making sequential tunneling the dominant mechanism, which is well described by the *orthodox theory* [3]. This condition, $R >> R_Q$, which is one of the assumptions of this theory, implies that electrons in the grain are localized, reflecting the importance of the coupling strength of tunnel barriers in single-electron devices [57, 9].

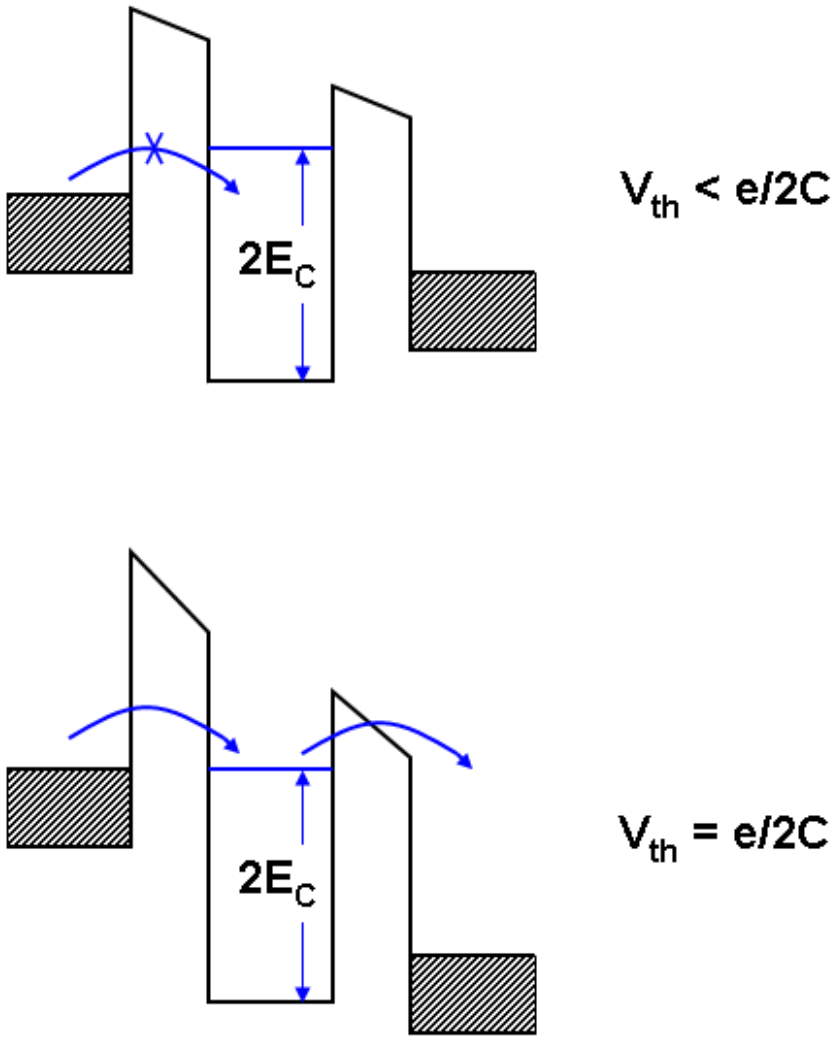

Figure 2: Energy diagram illustrating the phenomenon of Coulomb blockade. V_{th} is the voltage threshold for electron tunneling.

Moreover, this condition ensures that higher order tunneling processes, such as *cotunneling* [87] can be neglected. In the orthodox approach, the probability of a random tunneling event (an electron tunneling in or out of the grain) depends only on the change in the electrostatic energy resulting from this tunneling event [4]. Therefore, by changing the bias voltage across the barrier, the number of charged states in the leads also changes, affecting the tunneling probability of electrons in and out of the grain. Another assumption of the theory is that the amount of time it takes to tunnel through a barrier, is negligibly small compared to the time interval between tunneling events, which is adequate for small tunnel junctions [22, 60].

1.2.3 Energy Relaxation in Metallic Nanoparticles

One of the main reasons to study spin transport through nanoparticles, is that spin-orbit scattering processes are considerably weaker than in the bulk form [40]. This regime is interesting because spins injected from ferromagnetic leads into the particle, can have significantly longer lifetimes. This is a consequence of stationary electron wave functions being treated as slightly perturbed spinors [66, 19]. In samples consisting of Al nanoparticles tunnel coupled to two ferromagnetic leads (Chapter 3), the spin-polarized electron current takes place via discrete energy levels of metallic nanoparticles, in a regime where the tunneling rate is much smaller than the spin-conserving energy relaxation rate via phonon emission [1], ν_{e-ph}:

$$\nu_{e-ph} = \left(\frac{2}{3}E_F\right)^2 \frac{\omega^3 \tau_e \delta}{2\rho\hbar^5 \upsilon_S^5} \tag{5}$$

where E_F is the Fermi energy, ω is the energy difference between the initial and final states, τ_e is the elastic-scattering relaxation time, ρ is the ion mass density, and υ_S is the sound velocity. In aluminum nanoparticles with level spacings of $\sim 1meV$, $\nu_{e-ph}(\delta) \sim 0.1GHz$ [90]. In our samples, the tunneling rates, I/e, are smaller than this relaxation rate, so the nanoparticle can be assumed to be in the lowest energy state, accessible via spin-conserving transitions.

Spin-flip transitions can also take place due to electron coupling with phonons and nuclear

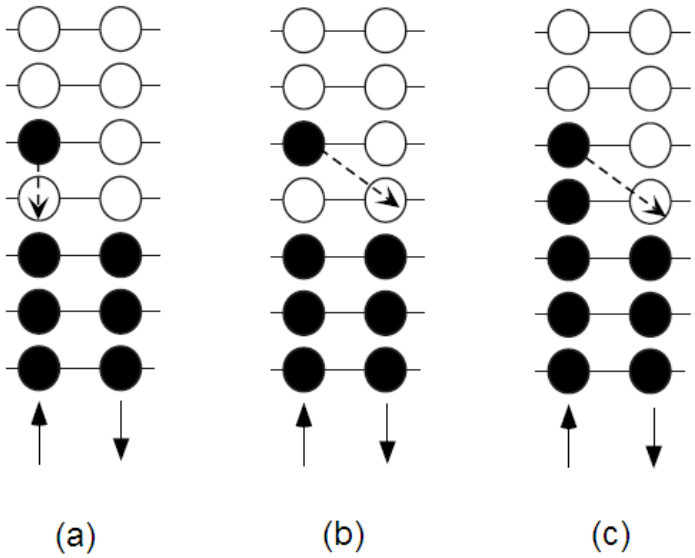

Figure 3: (a) Spin-conserving energy relaxation (b) Spin-flip energy relaxation (c) Spin relaxation time equals energy relaxation time.

spins, as illustrated in Figure 3b. In the absence of an applied magnetic field, the electron transitions shown in Figures 3a-b have the same energy difference between initial and the final states. Due to transfer of angular momentum from the particle to the environment, the spin-flip relaxation rate is expected to be much smaller than the corresponding spin-conserving relaxation rate. The spin-relaxation rates can be determined from tunneling measurements by trapping the nanoparticle into a state shown in Figure 3c (anti-parallel configuration of the leads) [90]. Then, spin-conserving energy relaxation will be forbidden by the Pauli exclusion principle and the relaxation rate will equal the spin-relaxation rate.

Spin-polarized current originates from spin accumulation in the particle, in a process that takes a large number of sequential tunneling events (in and out of the particle). Due to the sample fabrication process, the resistances of both tunnel junctions in our samples are different. If we assume that an electron tunnels into the particle via the lower resistance junction, followed by an electron tunneling out via the higher resistance junction, it is clear that in order to observe magnetoresistance, the spin relaxation time in the particle must be longer than the tunnel-out time. This reasoning does not change by reversing the bias

voltage, as long as the number of occupied electron states available for discharge, is large. If an electron first tunnels in via the higher resistance junction and an electron tunnels out via the lower resistance junction, it is unlikely that the same energy level will be involved in both tunnel events. Therefore, spin accumulation in the nanoparticle is still necessary for the occurrence of TMR, which at large bias voltages should show similar behaviors for both positive and negative polarities.

1.2.4 Magneto-Coulomb Effects

When single-electron tunneling takes place in nanostructures containing ferromagnetic components, their magnetization direction can couple to the electronic charge, giving rise to usually called, *Magneto-Coulomb* effects [75, 76]. In the presence of an external magnetic field, the two spin sub-bands in a ferromagnet are shifted by an amount equal to the Zeeman splitting, ΔE_Z, with the majority band being shifted down (lower energy), and the minority band shifted up (higher energy), as shown in Figure 4. For illustration purposes, the energy diagram uses the parabolic "free-electron" model of spin sub-bands. The difference in the densities of states of the spin sub-bands at the Fermi energy, induces a repopulation of conduction electrons between these two bands, followed by a corresponding shift in the chemical potential in order to conserve the total number of electrons. This shift in the chemical potential has been calculated [43, 75], and is given by:

$$\Delta\mu = -P\Delta E_Z = -Pg\mu_B H/2 \tag{6}$$

This expression is a good approximation in the regime where $\Delta E_Z \ll \mu$, and $k_B T \ll \mu - J$, which corresponds to temperatures below room temperature. Here, J is half the exchange splitting of the ferromagnet (at zero field). It is important to mention that P in this case, is the thermodynamic spin polarization at the Fermi energy, defined as:

$$P = \frac{N_\uparrow - N_\downarrow}{N_\uparrow + N_\downarrow} \tag{7}$$

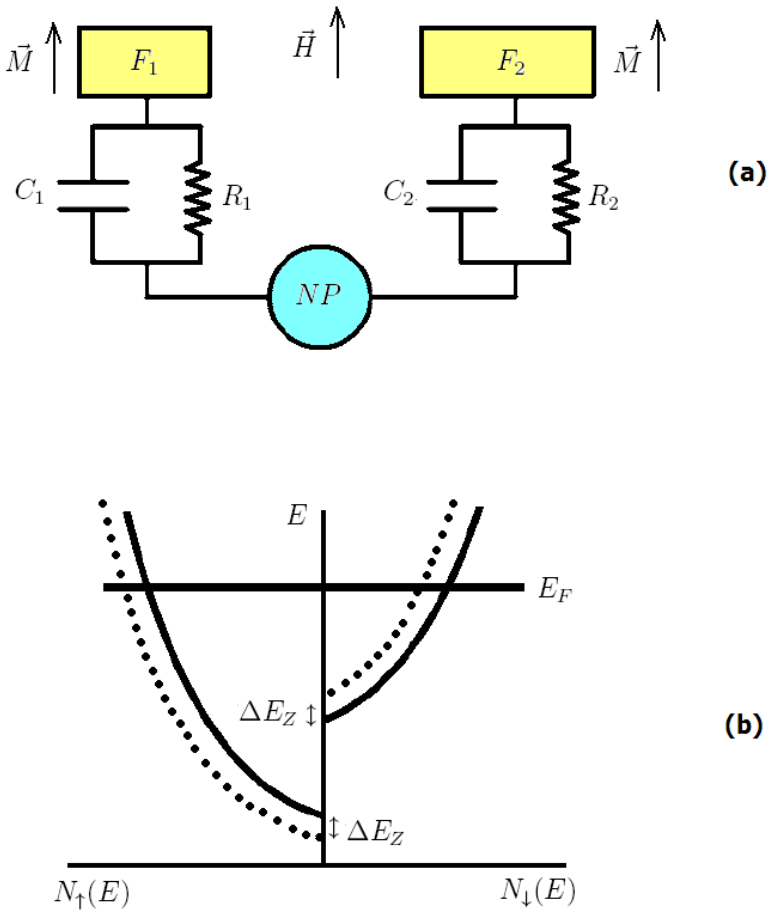

Figure 4: (a) Equivalent circuit of a double tunnel junction with no gate. (b) Splitting of the spin sub-bands induced by the external magnetic field, H.

Values of P given by the expression above, differ from the values obtained from spin-polarized tunneling experiments [44], since the latter is weighted by the tunneling probability of each conduction band at the Fermi level [75, 76]. Experiments involving ferromagnetic nanostructures, should always account for magneto-Coulomb effects.

1.3 Ferromagnetic Nanoparticles

1.3.1 Overview

Ferromagnetic materials have the interesting ability, even in the absence of an external magnetic field, to exhibit spontaneous magnetization. In macroscopic samples, this magnetization is confined to small subdivisions, first postulated by Weiss in 1906, as *magnetic domains*, in an attempt to explain the phenomenon of magnetic hysteresis. At thermodynamic equilibrium, these domains have their magnetizations randomly oriented. The vector sum of the magnetic moments of each domain, gives the total magnetic moment of the sample. In the absence of an external magnetic field, the net magnetization is close to zero, whereas in the presence of a field, the domains tend to align along the field, up to a saturation value (when the field is strong enough to align all domains along its direction). Since the magnetostatic energy is proportional to the volume of the sample, while the domain wall energy (interaction energy between adjacent domains) is proportional to its surface area, there will be a critical size, below which the formation of domains becomes energetically unfavorable [8]. Ferromagnetic particles with diameters below $\approx 15nm$, are usually single-domain, with magnetization (for a given applied magnetic field) uniformly distributed throughout their volume [7].

Research efforts pursuing control over the stability of such small particles, have been rapidly increasing, due to their promising potential for practical applications, including magnetic storage devices, ferrofluids for biomedical purposes, improvement of magnetic resonance imaging, site-oriented drug delivery, and cell membrane manipulation [8, 55, 28]. However, in order to achieve such ambitious goals, a much deeper understanding concerning inter-particle interactions and control mechanisms of magnetization reversal in

single-domain particles, is needed.

1.3.2 Size Effects in Magnetic Particles

Consider a system of magnetic particles in thermal equilibrium in the absence of anisotropy. It will behave similarly to atomic paramagnets, with mean magnetic dipole moment along the direction of the applied field, given by:

$$\left\langle \vec{m} \cdot \vec{h} \right\rangle = m \left(\coth \xi - \frac{1}{\xi} \right) = mL(\xi) \tag{8}$$

where $\vec{m}$ is the particle's magnetic moment, $\vec{H}$ is the applied magnetic field, $\vec{h} = \vec{H}/\mathrm{H}$, $\xi = \mathrm{m}H/(\mathrm{k}_B T)$, and L is the Langevin function, which describes the behavior of paramagnetic atoms. The crucial difference between the Langevin's picture of paramagnetism and the expression above is that the former deals with magnetic moments of single atoms while the latter accounts to tens to hundreds of thousands of spins, giving rise to a quite large magnetic moment per particle. Such large magnetic moments as well as magnetic susceptibilities combined with the strong temperature dependence of the coercive field in these particles, are the main characteristic of *superparamagnetism* [7]. Single-domain ferromagnetic particles show superparamagnetic behaviour whenever the thermal coupling to the surroundings is able to equilibrate the collective magnetization of the system in a time interval which is shorter than the one of a given experiment. Under such conditions, the particles exhibit paramagnetic-like behavior, but with a much larger magnetic moment than individual atoms, hence the name *super*paramagnetism.

The simplest case lacking axial symmetry concerns uniaxial anisotropy systems, where an external magnetic field is collinear with the anisotropy field [85]. For simplicity, consider the special case, where the free energy is represented by an energy barrier, $K_1 V$, separating the two stable magnetization states aligned parallel or anti-parallel to the particle's easy axis. K_1 is first order magneto-crystalline anisotropy constant [52] and V is the particle's volume. In this case, the magnetic energy of the particle is given by:

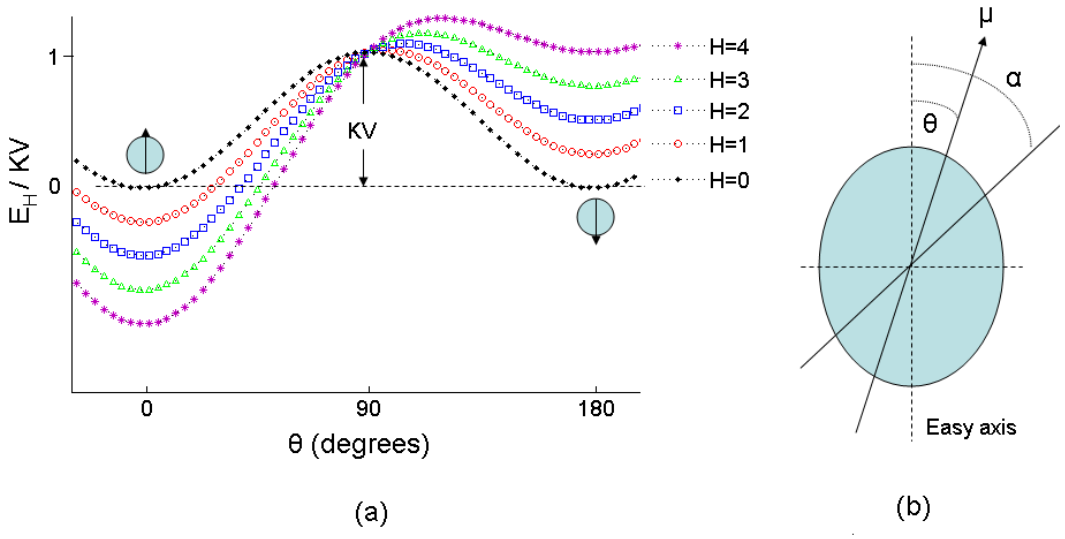

Figure 5: (a) Plots of the particle's free energy as a function of the angle between the magnetization and the easy axis for different values of the external magnetic field (a.u.). (b) Sketch of vectors and angles involved in Eq. 9.

$$E_H = K_1 V \sin^2\theta - \mu H \cos(\alpha - \theta), \tag{9}$$

Figure 5a shows the effect of different values (arbitrary units) of the external magnetic field, H, on the barrier's height. The angles involved in Eq. 9 are shown in Figure 5b. It is assumed that the external field is applied along the easy axis.

The process of thermally-induced magnetization switching can be characterized by a relaxation time, τ, or the decaying time from a state of saturated magnetization, M_S, after the removal of the external field [55, 93]. For an ensemble of identical particles, this relaxation of the magnetization is described by an Arrhenius-like dependence:

$$M(t) = M_S \exp(-t/\tau) \tag{10}$$

For large values of τ, the system is found in a stable configuration with $M = M_S$, while for small values of τ, M decays to zero. In the intermediate regime, the system's magnetization neither stays stable for a long time nor quickly decays to zero. It exhibits a magnetization

which lags behind the magnetic field. Such effect is known as *magnetic after-effect* [28] or *Néel relaxation*. Néel's proposal for the relaxation time has the form [74]:

$$\tau^{-1} = \tau_0^{-1} \exp(-KV/k_B T) \tag{11}$$

where τ_0 is usually taken as a constant (roughly equal to the ferromagnetic resonance (FMR) frequency $\approx 1GHz$, which can be obtained either experimentally or theoretically) [74, 20]. Therefore, the probability that a sufficient number of magnetic moments will overcome the energy barrier, KV, in order to achieve thermal equilibrium, is proportional to $\exp(-KV/k_B T)$.

The magnetic response of nanoparticle systems, is known to directly depend on the time period of a given measurement, τ_m [55, 27]. It can widely vary: $10^{-8}s$ in Mössbauer spectroscopy experiments, to $10^{2}s$ in typical magnetization measurements. Two main regimes can now be considered. For $\tau \ll \tau_m$, the relaxation takes place faster than the measurement of the magnetization, allowing the system to attain thermodynamic equilibrium. In this case, the nanoparticles are found in the superparamagnetic regime. When $\tau \gg \tau_m$, the relaxation process is much slower than the measuring time, and the system behaves as magnetically ordered, in the so-called *blocked* regime. The *blocking temperature*, T_B, which is the temperature separating these two regimes, can be defined by setting $\tau = \tau_m$ for a given volume V and using Eq. 11:

$$\ln \tau = \ln \tau_0 + KV/k_B T_B \tag{12}$$

For an experiment where $\tau_m \sim 100s$, the blocking temperature is $T_B \approx KV/25k_B$. It is important to notice that the determination of T_B is somewhat arbitrary due to the arbitrariness of τ_m, as well as the finite distributions of size and anisotropy. For instance, the same system probed by Mössbauer spectroscopy and by a static magnetization measurement, would show blocked and superparamagnetic behavior, respectively. In the regime where $T \ll T_B$, thermal fluctuations can be neglected and the well known Stoner-Wohlfarth

model [85] can be used to calculate static magnetizations by minimizing the system's free energy. A close relation between the blocking state (below T_B) of the system and the effect of magnetic hysteresis can then be established. In magnetization measurements, a transition from a hysteretic to a non-hysteretic behavior of the hysteresis loop, is a common sign that superparamagnetism has taken place [84].

1.3.3 Damping and LLG Equation

Magnetization dynamics of small magnetic particles involves highly non-linear processes [67], that require sophisticated models usually based on the stochastic Landau-Lifschitz-Gilbert (LLG) equation, where the stochastic term (usually Gaussian white noise) represents the thermal bath [47, 61, 20, 28]. Similar methods within the Langevin's equation formalism, offer powerful alternatives to approach this complex and unexplored aspect of magnetism [25, 73], but a theory of nanomagnetism is far from complete. Magnetic relaxation in magnetic materials is usually approached by the phenomenological LLG equation:

$$\frac{d\vec{m}}{dt} = -\gamma\vec{m} \times \left(\vec{H_{eff}} + \vec{h_{th}}(t)\right) + \alpha\vec{m} \times \frac{d\vec{m}}{dt} \tag{13}$$

where γ is the gyromagnetic ratio, α is the Gilbert damping parameter, and $\vec{h_{th}}$ is the stochastic Langevin field (assumed to be Gaussian white noise) representing the thermal environment. The effective magnetic field is given by $\vec{H_{eff}} = -\frac{\partial G}{\partial \vec{m}}$, where G is the Gibbs free energy of the system, which includes magnetic anisotropy and Zeeman energies. The first term on the right-hand side is usually referred to as the conservative part and the second one as the dissipative part. The Gilbert damping parameter, α, provides information on how fast the magnetization relaxes to equilibrium after the removal of an external field, and therefore is related to the magnetic viscosity of the system [73]. The origin of magnetic damping and energy dissipation in the nanoscale is not fully understood, due to the contribution from many different mechanisms, including spin-orbit interactions, eddy currents, and magnon-phonon scattering (see appendix A for a more detailed description of these processes).

Many experimental results can be reasonably well described by theoretical models using appropriate limiting cases and a variety of approximations. Brown [20] used the LLG formalism to derive the corresponding Fokker-Planck equation for the distribution of magnetic moment orientations. He obtained the same result for the relaxation time obtained by Néel, except for the prefactor τ_0^{-1}. It is remarkable the wide range of related problems that can be handled within the relatively simple Néel-Brown model [74, 20, 92]. This model is particularly used to study magnetization dynamics in granular, thin films, or bulk magnetic materials. It assumes a single-domain magnetic particle with two equivalent ground states corresponding to opposite magnetization, separated by an anisotropy energy barrier, as previously shown in Figure 5. Recent studies on thermally-induced magnetization reversal in magnetic nanoislands [58], using spin-polarized scanning tunneling microscopy (SP-STM), show that the prefactor τ_0^{-1} strongly depends on the morphology of the islands, with changes of orders of magnitude in the switching rate, due to small variations in size or shape. Different models applied to more specific cases, such as electron tunneling transport through magnetic nanoparticles, also exist [70, 23, 54]. However, a satisfactory agreement between theory and experiment is still lacking.

CHAPTER II

EXPERIMENTAL TECHNIQUES

2.1 Sample Fabrication

In this section, a description of each step of the sample fabrication process will be given. Every step along the overall process, needs to be carefully and thoughtfully executed, since a single mistake near the end, can compromise the whole process, which can take from a couple of days to a week of hard work.

2.1.1 Silicon Wafer Preparation

The very first step is to make sure that a clean piece of silicon is used as the substrate. The silicon wafers used here have a $30\mathring{A}$ surface layer of thermally grown oxide, to avoid electric charging effects which could possibly damage the samples. The cleaning procedure consists of sonicating the wafers in the following solutions: first in trichloroethylene (TCE), followed by acetone, and finally, isopropyl alcohol (IPA), for about 10 minutes in each solution. The wafers are then blow dried with dry air and immediately transfered to a vented hood in order to be coated with the appropriate lithography resists. Before coating the first resist layer, a quick extra cleaning of the wafer is performed by spinning the wafer at 5500 RPM and flushing it with acetone for about 10 seconds, followed by IPA for another 10 seconds, and finally letting it spin dry for another minute. This simple procedure assures that eventual dust collected during the transportation is washed off. Methyl methacrylate (MMA) is used as the first resist layer, being spun as soon as possible after the cleaning, at 1000 RPM for about 90 seconds, followed by a 10 minutes bake in a hot plate at 150 C. Next, the top polymethyl methacrylate (PMMA) layer is spun at 5500 RPM for one minute and baked at 180 C for another 10 minutes. The wafer can now be safely protected in an appropriate case and, when not in use, should be kept preferably in a "dry-box". The wafer can now be conveniently cleaved down to smaller rectangular-shaped chips ($\approx 2cm \times 3cm$), to facilitate

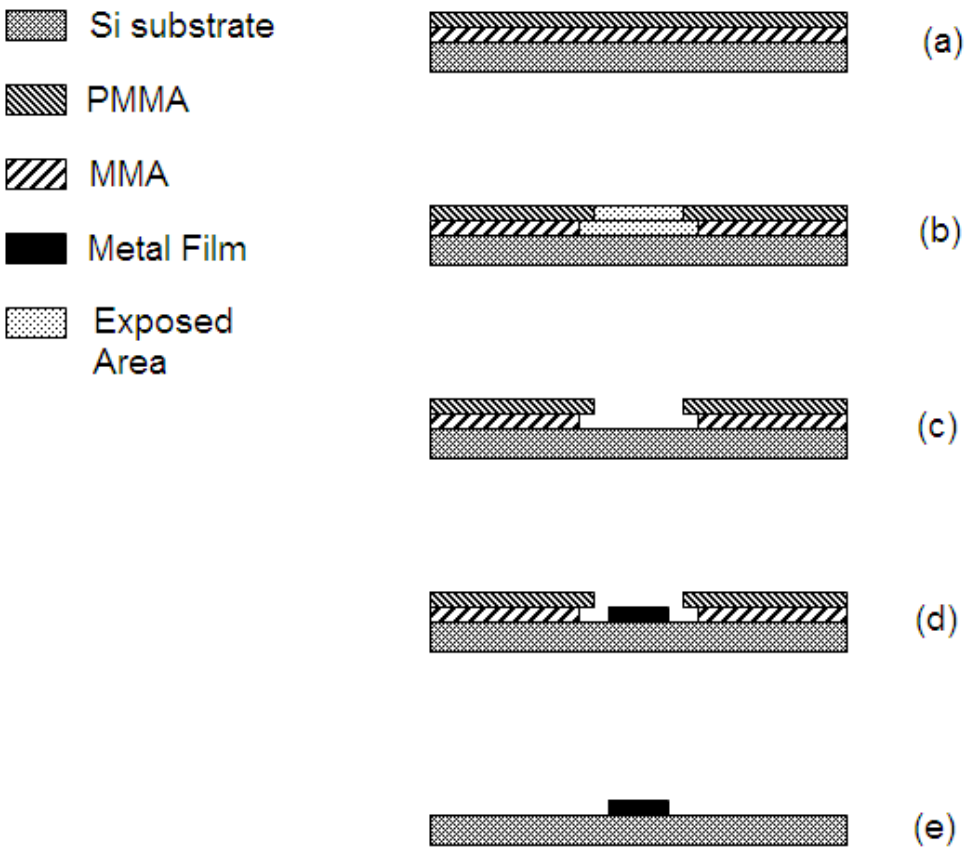

Figure 6: (a)Si wafer coated with MMA/PMMA bilayer; (b)Dotted region represents an area exposed by the electron beam; (c)The exposed area is removed during the development step; (d)A metal film is deposited; (e)Final pattern after lift-off in acetone.

the lithography process. This is easily done with the help of a diamond-tip scribe and the edge of a glass slide as a guide for the cleavage line. By doing this, small scratches at the corners of the chip can be used to find the desired starting position to write an array of patterns.

2.1.2 Electron Beam Lithography

The wavelength of electrons with energies $\sim 10kV$, are 3 to 4 orders of magnitude smaller than photons, providing outstanding resolution in the writing of nanometer scale patterns. The Electron Beam Lithography (EBM) technique makes use of a beam of electrons to write the desired pattern over a resist coated substrate. By sourcing an electric current through a tungsten filament, electrons are "boiled-off" via thermionic emission. An applied voltage up to 30kV between the cathode (the filament itself) and the anode (basically a metallic plate with a hole in it), accelerates the electron cloud away from the filament, creating the electron beam (Figure 7). In order to efficiently avoid the beam to spread out, another important part of the electron-gun, called *wehnelt*, is fundamental. It consists of a metal cap surrounding the filament and it has an orifice in its center to allow the passage of the electron beam. By applying a negative bias voltage to the *wehnelt*, equipotential surfaces(dotted lines in Figure 7) can be adjusted to be very close to the filament. Therefore, electrons below these surfaces will be accelerated towards the anode and by tuning the value of the bias voltage, in order to keep the equipotentials as close to filament as possible, one can optimize the electron emission process. The electron beam leaving the *wehnelt* then passes through a series of electromagnetic lenses, which are used to further collimate the beam before it finally reaches the sample.

The resolution of EBL strongly depends on the interaction between the incoming electrons and atoms/molecules in the resist material [64]. Electron backscattering processes will be present to some extent, affecting unwanted areas in the vicinity of the actual pattern. These so called, proximity effects can be minimized by properly choosing the values of controllable parameters such as accelerating voltage, working distance (WD), and beam spot size, ensuring the best possible writing conditions.

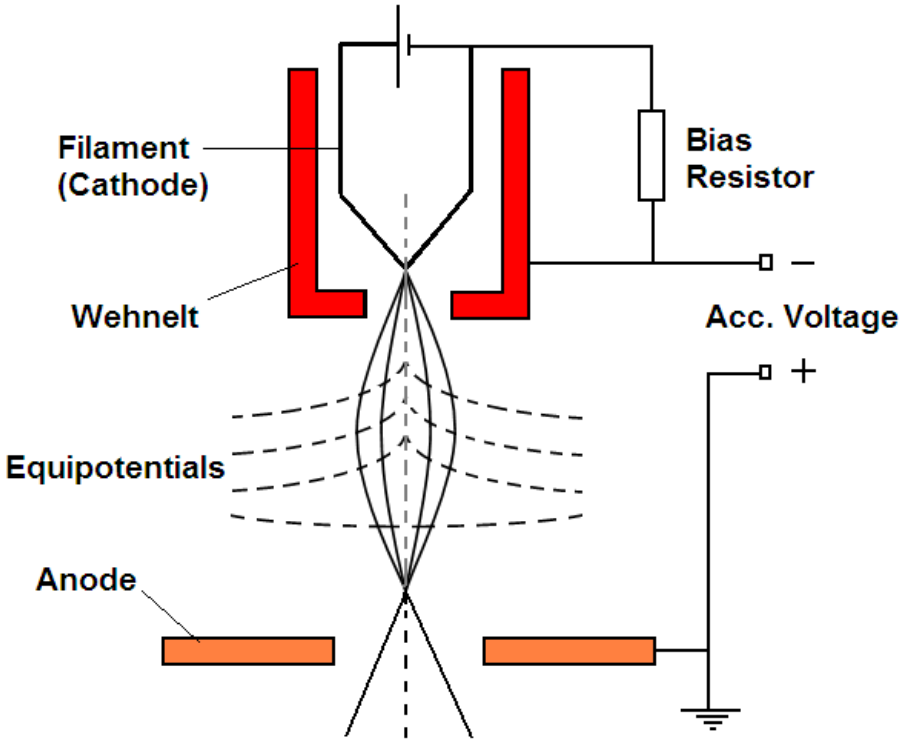

Figure 7: Schematic diagram of a scanning electron microscope's electron gun. Electrons generated at the filament by thermionic emission, are accelerated by voltages applied to the *wehnelt* and anode plate, giving rise to the electron beam.

The machine used to perform the lithography is a JEOL Scanning Electron Microscope (SEM) model JSM 5910. The interface between SEM and computer is established by the widely used software *Nanometer Pattern Generation System* (NPGS). This software provides automation tools for the SEM, allowing full control of the writing parameters, including the electron doses to be used, magnification, and CAD files containing all the geometric features of the device to be written.

Figure 8 shows the pattern design used for the different classes of samples: FNF, FNN, and NFN, where F designates a ferromagnetic metal (Co or Py), and N a non-magnetic metal (Al). Figure 8a shows the design pattern used for NFN devices and Figure 8b for FNN or FNF devices. The main reason for having different geometries is to avoid significant fringing fields generated by the ferromagnetic electrodes (if that is the case), in the vicinity of the particles. The pattern shown in Figure 8b illustrates the attempt to form single-domain magnetic leads to minimize the fringing field, and also provide well defined switchings of their magnetization [73, 51]. In all of them, the metal in the middle is in the form of nanoparticles embedded in an insulating matrix of Al_2O_3, forming two tunnel junctions with the outer metal electrodes. Figure 8c illustrates how the gap size determines the width of the PMMA bridge and consequently, the overlap area between the two electrodes. The following section describes this procedure in detail.

2.1.3 Thermal Evaporation

After the lithography is finished, the batch of samples is developed by dipping the chip in a solution of 1:3 (Methyl Iso-Butyl Ketone (MIBK):IPA) for 1 minute, rinsed with IPA, and blow dried with dry air. A quick inspection using an optical microscope is performed to make sure that no significant misalignments have taken place during the lithography process. The sample can now be loaded in the vacuum chamber of the evaporator, where the metal films will be deposited by resistive evaporation. The sample batch is attached to a rotary stage using carbon tape. A metal spring is connected to the stage, allowing external control of the angle of incidence of the vapor beam at the sample. Figure 9 displays a simple diagram with the basic components of the evaporator.

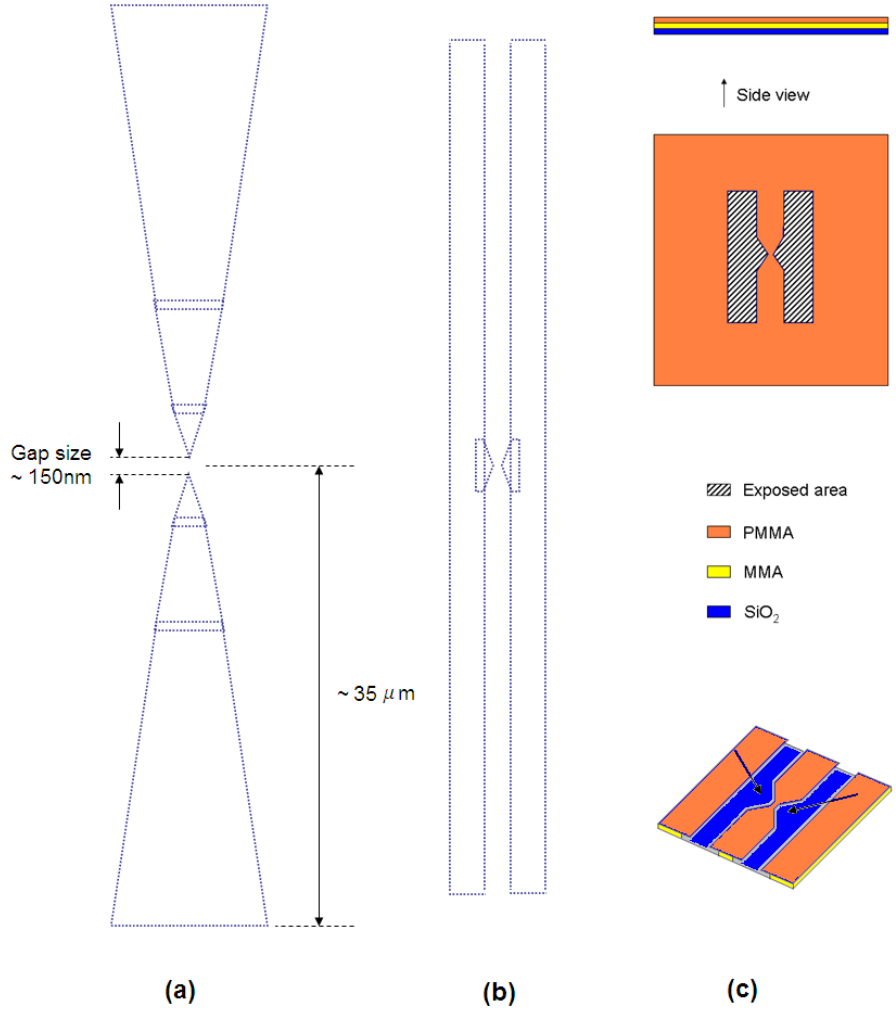

Figure 8: Design pattern for (a) NFN devices and (b) FNN devices. (c) Example of how the gap size in (b) influences the overlap area between the two electrodes during the thermal evaporation process. The arrows indicate the direction of evaporation.

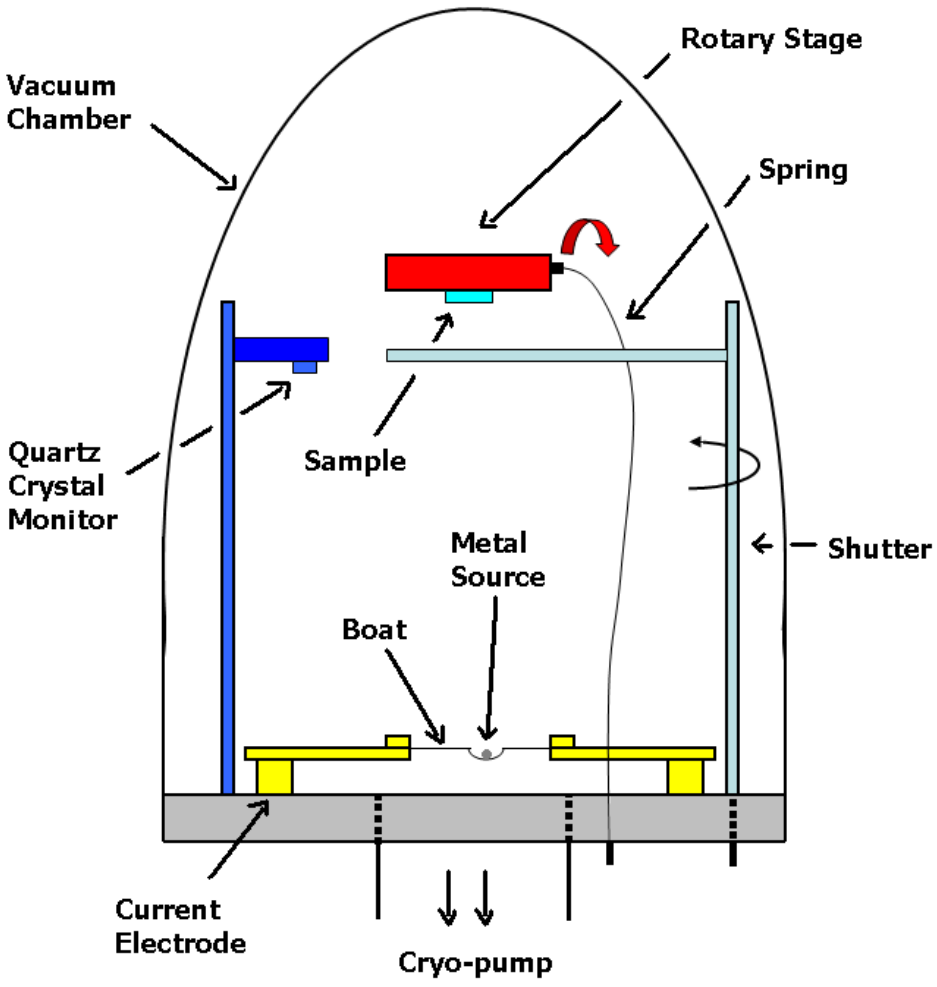

Figure 9: Diagram showing the basic setup of the evaporator chamber, particularly the external rotation control of the stage.

During the evaporation process, the selected metals are placed in tungsten boats and heated up by sourcing an electric current through the boat. When the temperature gets above the source material's melting point, a beam of vapor starts spreading through the whole chamber, and the thickness of the resulting thin film can be controlled. A quartz crystal monitor (Inficon XTM/2) is used to monitor the film thickness. Before starting the deposition process, the chamber is typically pumped out overnight, or until a base pressure of about 3×10^{-7} mbar is reached. Aluminum (99.999%, from Alfa Aesar) was used as the non-magnetic metal in all of the samples measured in this project. The ferromagnetic metals used were Cobalt (99.95%, from Alfa Aesar) and Permalloy ($Ni_{80}Fe_{20}$, from GoodFellow).

The technique used to fabricate these devices, is called *shadow evaporation* [31]. Its basic idea consists in using a PMMA "bridge", which is supported by the MMA underlayer, to act as a mask during the metal evaporation. By changing the angle of evaporation relative to the sample, it is possible to obtain very small overlaps between different deposition steps. An illustration of how this technique is applied to our samples is shown in Figure 10.

For the FNN samples, 200Å of Py is first deposited along direction 1, followed by 15Å of Al_2O_3, 5Å of Al, 15Å of Al_2O_3, and 200Å of Al, all of them deposited along direction 2. The angles defining directions 1 and 2 are chosen so that the resulting metal electrodes barely overlap each other, with only a few nanoparticles (possibly a single one) available for tunneling. The final fabrication step is a standard *lift-off* [42] in acetone, as shown in Figure 6.

2.2 Transport Measurements

2.2.1 Initial Tests

Once the metals have been deposited and the lift-off process has finished, the resistance of each device in the batch can be measured at room temperature using micro-manipulators (Signatone, Model S725-PRM). The bias voltage is supplied by an SRS Synthesized Function Generator (DS345 - 30MHz) and the current is measured via a low noise Ithaco current amplifier (model 1211) connected in series with the sample. The circuit setup is shown in Figure 11. The "Ithaco box" is used to minimize spurious interference and to safely apply a

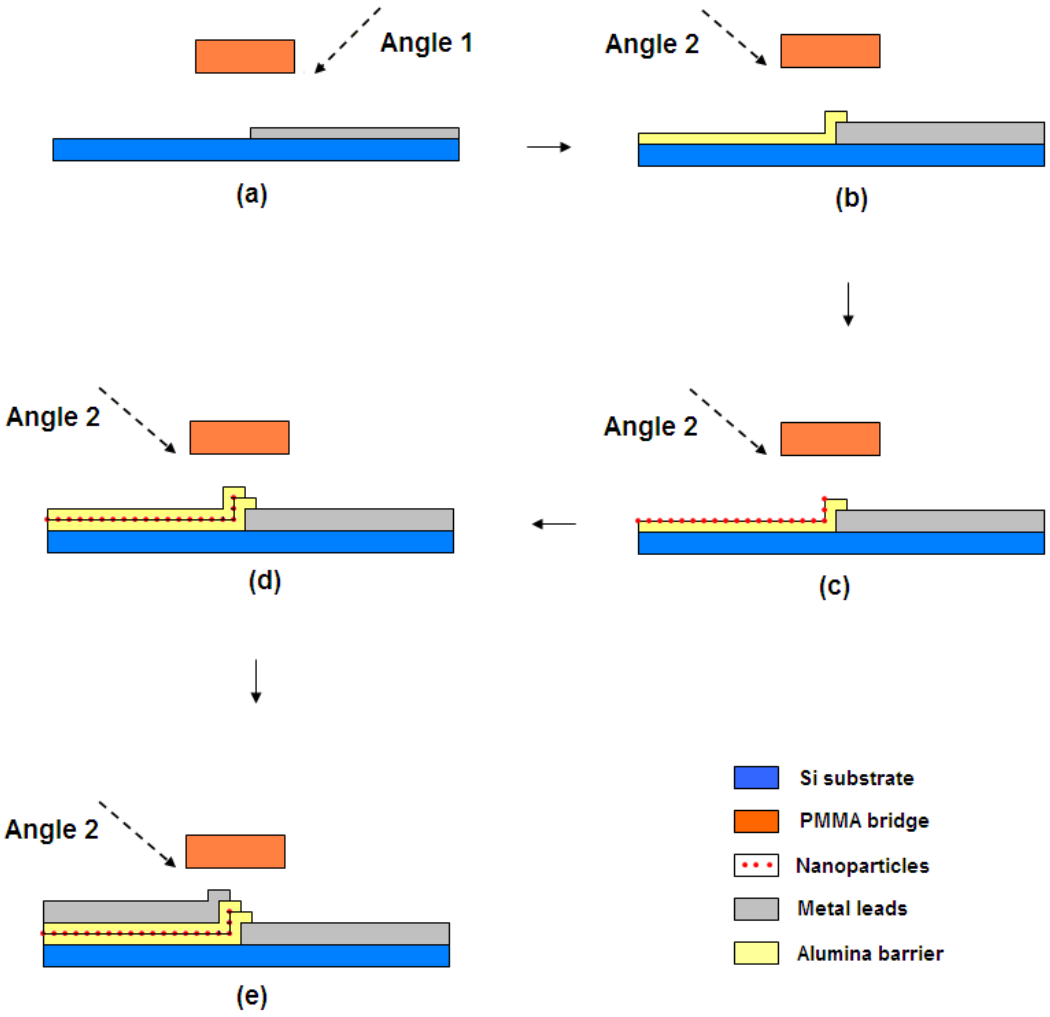

Figure 10: (a) First metal lead is deposited at angle 1; (b) After switching to angle 2, an Al_2O_3 layer is deposited followed by: (c) a layer of nanoparticles, (d) Another Al_2O_3 layer, and finally (e) the other metal lead.

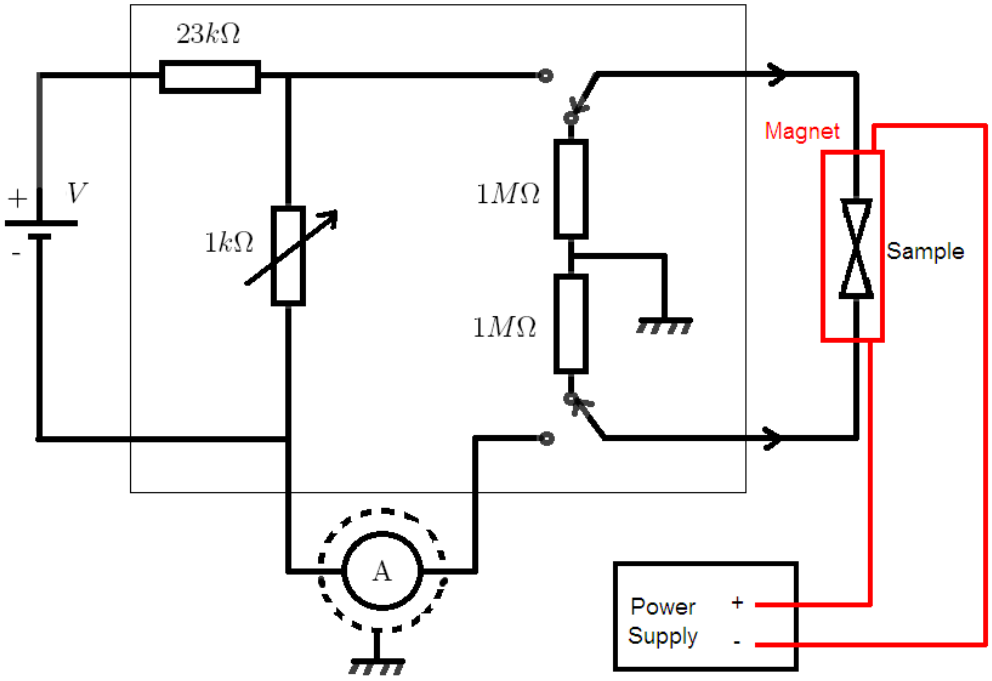

Figure 11: Circuit diagram showing the basic elements used to measure the I-V characteristics of pre-selected samples.

bias voltage to the sample. The box basically consists of a series limiter resistance, a voltage divider, and a triaxial connector coupling to the current amplifier. A schematic diagram of the basic circuit is shown in Figure 11.

Each column of the array of devices has a slightly smaller tunneling overlap area than the preceding one, due to the different "gap sizes" (Figure 8) used during the lithography step. Consequently, their electrical resistances are expected to follow the same trend. In other words, devices with a small lithographed gap between the tunnel contacts, will have a larger overlap between metal electrodes after the metal deposition, and vice-versa. In this way, it is always possible to identify an optimal resistance range of potentially good devices.

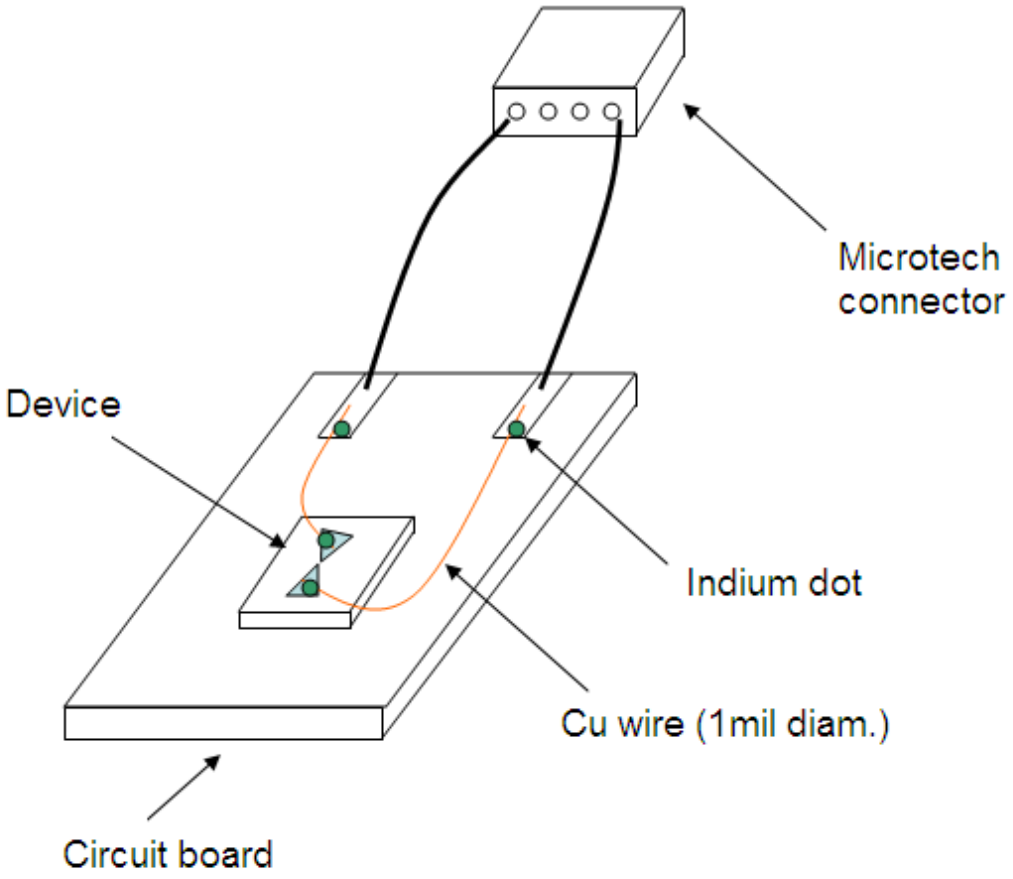

Figure 12: Schematics of a typical 2-terminal sample holder and the main elements required for wiring up the device.

2.2.2 Measurements at 4.2K

Samples in the $M\Omega \geq G\Omega$ resistance range are chosen to be tested at lower temperatures. Before measuring the I-V curve characteristics of each sample at liquid Helium (LHe) temperature (4.2K), the samples need to be wired up. This is a very delicate and important step, since we are literally connecting wires to the sample,s electrodes. Wire-bonding is not an option for these devices, since heat, mechanical shock, or electrostatic discharge, would certainly "kill" the sample. Copper wire 99.99% with diameter of 1 mil from CFW, is used for the connections between the sample holder and the chip. Typical sample holders

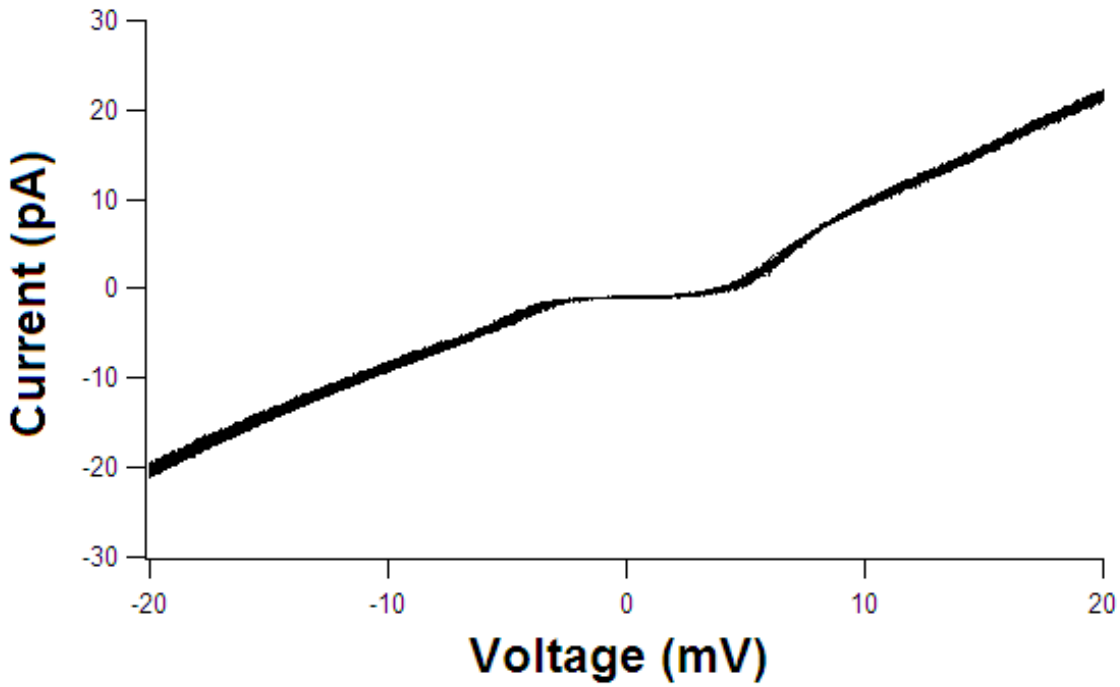

Figure 13: Current-Voltage characteristics of a representative sample at 4.2K.

(see Figure 12) are made from a small piece of circuit board, and the chip is placed at the center by using a little dab of vacuum grease (Apiezon Products). Make sure that everything is grounded. The contacts are made using indium dots, which are just small pieces of indium wire chopped with a razor blade. With the help of a half-tweezer or equivalent tool, we gently pick an indium dot, followed by a piece of the copper wire which sticks to the dot, and finally attach the "dot/wire" to one of the metal pads on the chip. The same procedure is repeated for the other electrode. After all these steps are successfully executed, the sample is ready to be plugged into the "dipstick" and further tested. The dipstick has a superconducting magnet attached to its end, so it can be conveniently inserted into the LHe dewar for eventual TMR measurements. The sample is electrically mounted via Microtech connectors. It will be shown in Chapter 5 that microwave pulses can be applied to the samples via specifically designed sample holders. Figure 14a shows the electromagnet used for the experiments at 4.2K, as well as the electrical and optional microwave connectors. Figure 14b shows the double-axis electromagnet that can also be used in the dilution refrigerator. After slowly inserting the dipstick into the LHe dewar,

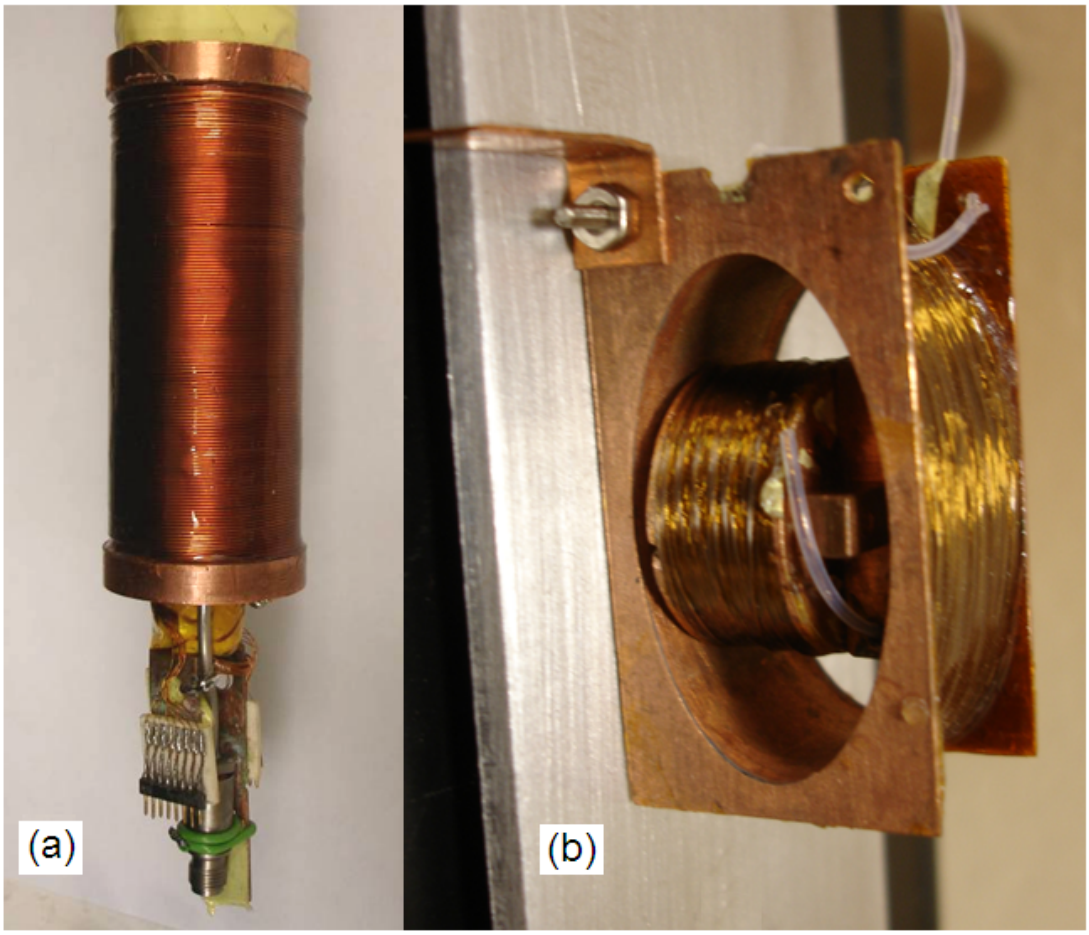

Figure 14: (a) Superconducting magnet for measurements at 4.2K. (b) The double-axis magnet can be used either at 4.2K or attached to the dilution refrigerator.

the I-V curves are taken using a LabView interface with the computer. The bias voltage is swept at $\sim 0.2mV/s$ up to an amplitude of $\sim 50mV$, which is sufficient to identify Coulomb Blockade (CB) phenomena in our samples. A linear I-V curve indicates that the tunneling junction is likely to be too large, with multiple particles or even a "short" contributing to the current. Another possible outcome is empty junction devices, which will basically behave as capacitors. Therefore, by changing the sweeping frequency of the bias voltage and observing the corresponding changes in current, it is possible to identify such devices. Both, empty and shorted devices, are not tested further. However, $\sim 40\%$ of tested devices show non-linearities or CB at 4.2K, as the one shown in Figure 13. About $\sim 20\%$ of the devices showing CB, will also show signs of TMR as well. A NFN sample showing TMR at

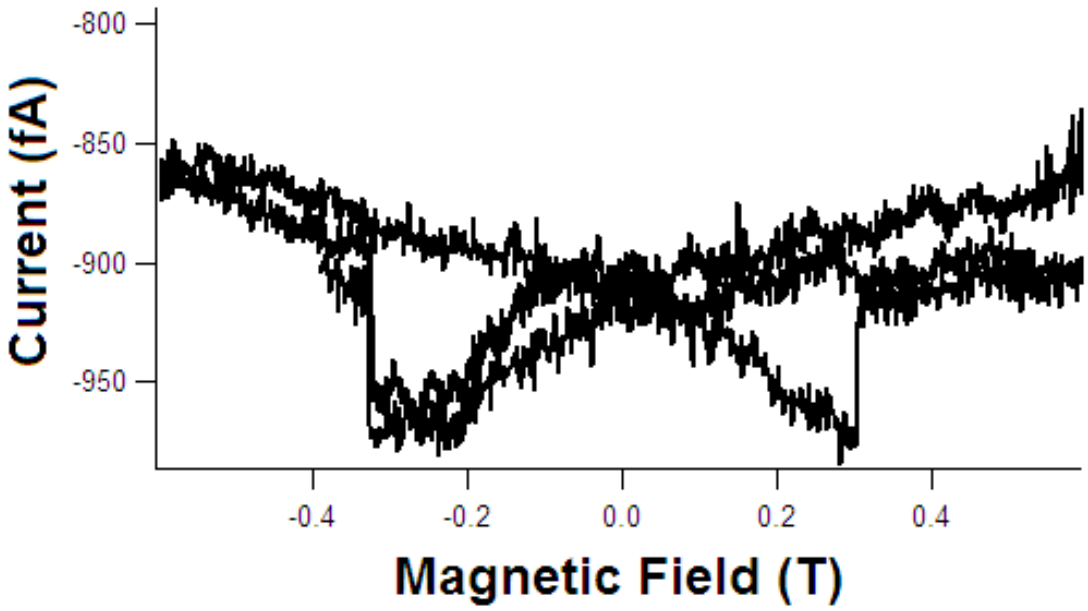

Figure 15: One of the few samples showing a reproducible TMR signal at 4.2K.

4.2K, is shown in Figure 15.

Although several samples show some kind of dependence on magnetic field, only a few of them will show reproducible switchings. However, some samples will show a much cleaner signal when cooled down to mK temperatures.

2.2.3 Measurements at the Dilution Refrigerator

Only a few samples (less than 20% of all tested samples) will qualify to be further tested using the dilution refrigerator. The principle of operation of the dilution refrigerator is based on the different thermodynamic properties of the two He isotopes, ^3He and ^4He. Although the cooling mechanism is purely quantum mechanical, the basic idea is shown in Figure 16. A mixture of the two stable helium isotopes undergoes a phase separation when it is cooled below a critical temperature, around 0.86K. These two phases are usually referred to as "concentrated phase", which is lighter and rich in ^3He), and a heavier "dilute phase", rich in ^4He, but containing 6%-7% of ^3He in it. By pumping on the dilute phase, mostly the inert ^3He minority will be removed. In order to restore equilibrium in the system, ^3He from the concentrated phase will have cross the phase boundary in a process

which requires energy to take place. This extra energy is taken in the form of heat, from the walls of the mixing chamber, where the sample is thermally anchored to. Therefore, cooling power is obtained by supplying a constant flow of ^3He through this closed cycle. Since the equilibrium concentration of ^3He in the dilute phase is finite even at zero temperature, this process keeps going at the lowest attainable temperatures. More details on the operation of the dilution refrigerator can be found elsewhere [63]. The sample wiring is filtered at the mixing chamber using a copper powder filter and a high-loss coaxial wiring with $10MHz$ bandwidth. The sample is in a Faraday cage and the filter output is connected coaxially with the cage. There are no unfiltered wires entering the cage. This step is very important in order to achieve the lowest possible electron temperature $\sim 0.1K$ (measured from the line-width of discrete levels in normal metal particles). It is possible to accommodate up to 4 samples at once. Since each electrical lead has a resistance of a few $k\Omega$, which is much smaller than the samples resistance (typically hundreds of $M\Omega$s), a simpler two-probe measurement is sufficient.

While handling the samples, extreme care must be taken to avoid permanent damage, such as disconnected indium dots and electrostatic discharge, which could easily ruin a whole week of work. Therefore, the use of grounded wristbands and static shielding bags to store the samples, are strongly recommended. After the samples have been loaded and all electric connections checked, the inner vacuum chamber (IVC) should be prepared to be pumped out. A turbo-molecular pump is used, to pump on the 1K pot, still, and condenser lines for a couple of hours, and a leak test should then be performed to guarantee a good heat exchange process during the initial cool down process. It is always good practice to use liquid nitrogen to pre-cool the system (dilution unit/cryostat) to 77K overnight, to minimize waste during the LHe transfer. After properly removing all the liquid nitrogen from the cryostat, LHe should be immediately transferred and the temperature can then be monitored. Once the system reaches thermal equilibrium at 4.2K, the procedure to condense and circulate the mixture ($^3He/^4He$) can be started. Details about this procedure will not be provided here, but can be found in the dilution refrigerator's guide. The measurement procedures are similar to the ones used at 4.2K. When using the dilution refrigerator, one big

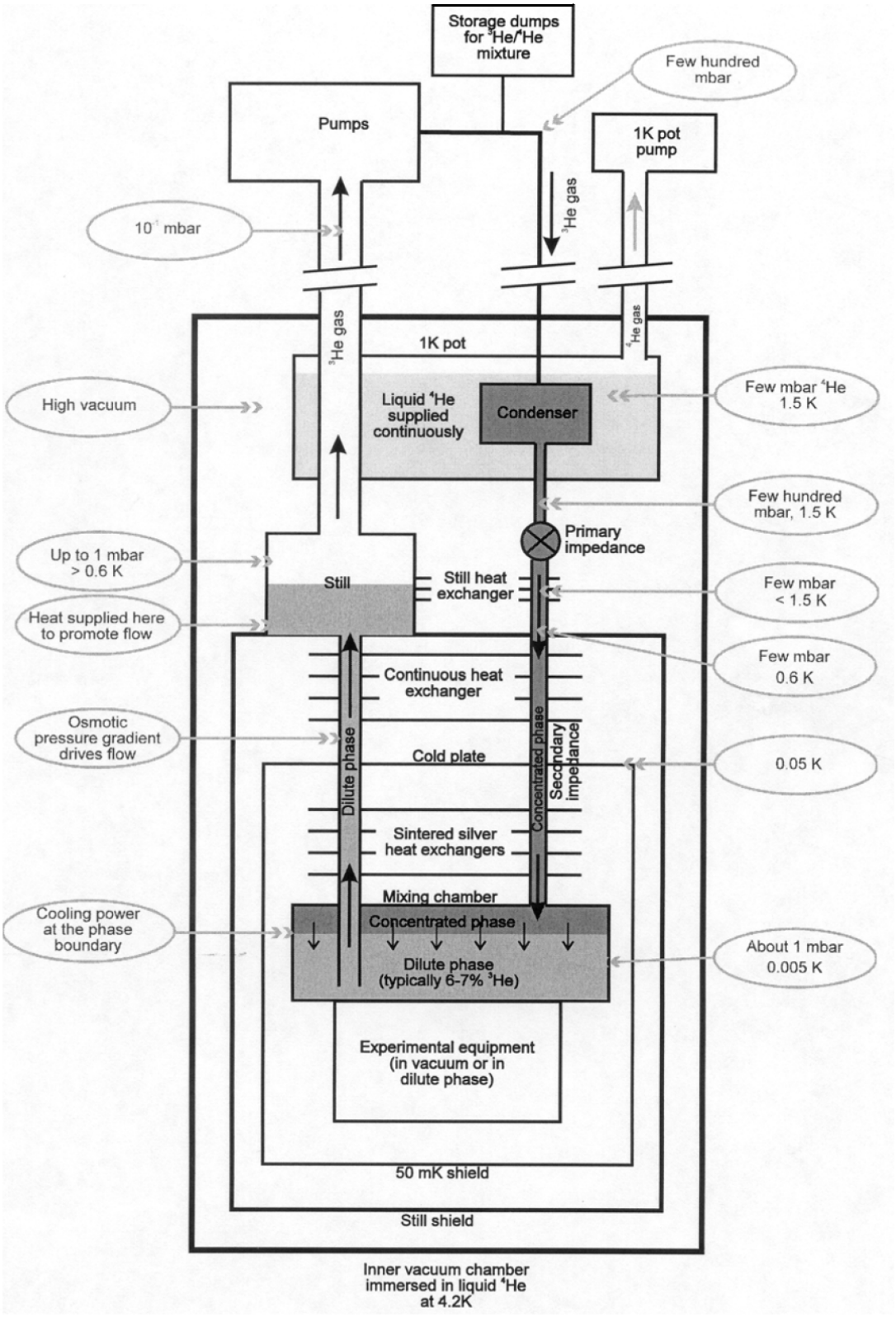

Figure 16: Diagram illustrating the basic principle of operation of a dilution refrigerator. Courtesy of Oxford Instruments.

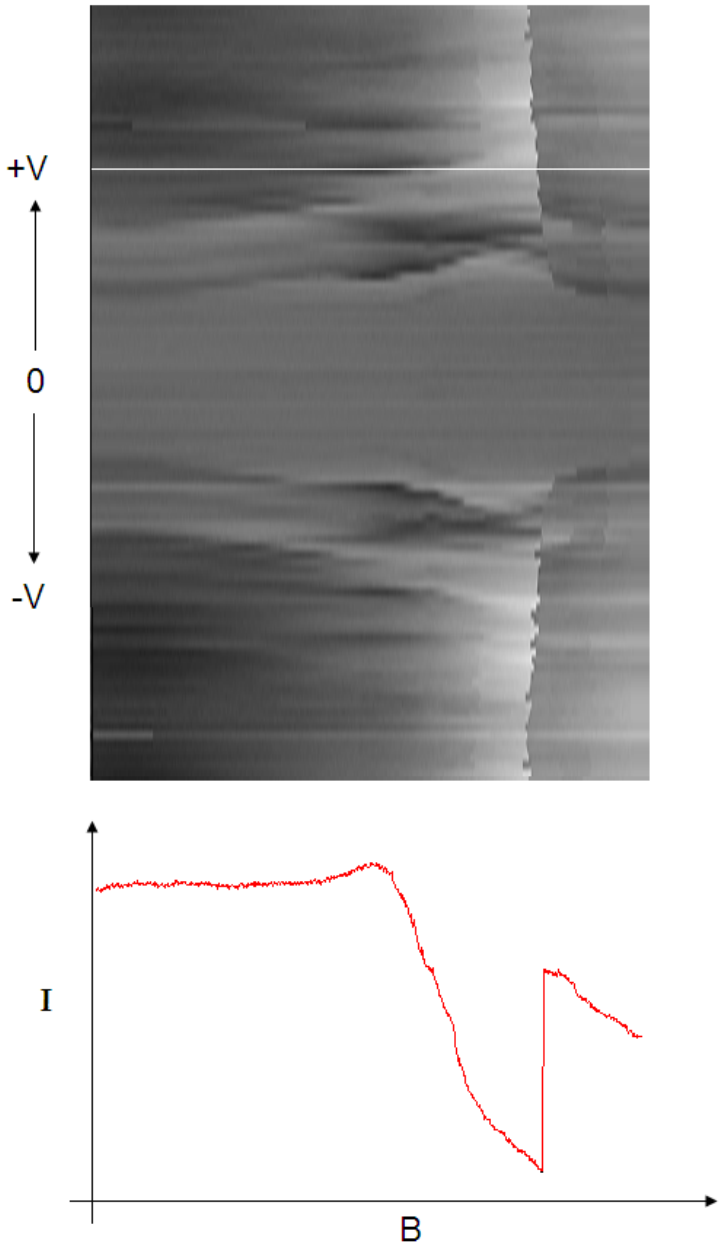

Figure 17: Typical current plot as a function of magnetic field and bias voltage in arbitrary units. The light (dark) areas represent low (high) currents. The white horizontal line is a cut profile, corresponding to the curve at the bottom.

difference is the much more powerful superconducting magnet, which uses a different power supply and it is able to reach up to 14T. A typical TMR image plot is shown in Figure 17, with a line profile (white) at the bottom. The magnetic field is swept fast ($\sim 60mT/s$) and the bias voltage is swept slowly ($\sim 15\mu V/s$). This image shows data from only one direction of the sweeping field (-1T to +1T)

CHAPTER III

SPIN TRANSPORT UNDER NON-COLLINEAR MAGNETIC FIELDS

3.1 Introduction

Studies of spin-polarized electron conduction in a non-collinear magnetic field are important for injection, detection and coherent manipulation of spins in electronic devices. In normal metals, electron spins can be injected from external ferromagnetic leads by tunneling. It has been demonstrated that a magnetic field applied perpendicular to the magnetization direction causes precession of the spin injected into the normal metal [46, 43]. In that effect, the spin of an electron injected from the ferromagnet exhibits precessional motion about the magnetic field while the electron diffuses through the normal metal.

In nanometer scale metallic particles, spin polarized electron transport is different from that in macroscopic samples [83, 6]. One important difference is the effect of the spin-orbit interaction [90]. In macroscopic metallic samples, where the electron-in-a-box level spacing, δ, is negligibly small, the spin-orbit interaction causes the electron wavefunctions to have an uncertain spin. As a result, an electron spin injected into such a sample will exhibit decay with the characteristic time equal to the spin-orbit scattering time τ_{SO}.

In Al particles with diameter smaller than about 10nm, the Heisenberg time corresponding to a quantum level spacing, $\hbar/\delta$, becomes shorter than the spin-orbit scattering time τ_{SO}. This case, where $\delta \cdot \tau_{SO}/\hbar > 1$, is known as weak spin-orbit scattering regime. For time scales longer than the Heisenberg time, spin-orbit scattering is quenched, and the electron wavefunctions will have certain spin. The electron spin direction in such a particle can decay only by some coupling to the environment [90, 91]. Evidence of long spin-relaxation time in metallic particles have been seen in spin-injection experiments where a single or an array of particles is attached by tunnel contacts to two ferromagnets [11, 90, 71].

The main question addressed in this chapter is whether the spin injected into the particle, by tunneling from a ferromagnet, exhibit precessional motion about a perpendicular magnetic field. Just as the finite level spacing quenches spin-orbit scattering, the spin-precession may also be quenched. This topic will be examined in section 3.2, where electron tunneling via the particle states in a non-collinear magnetic field will be discussed.

Experiments on spin-polarized current through a single aluminum particle as a function of the magnetic field direction, will also be discussed. This study was motivated by measurements of spin-precession in large scale metallic samples discussed above, and the initial goal was to observe similar spin precession in a metallic particle. The presented data indicate that spin-precession does not occur. The experimental signature of spin precession would be equal magnitudes of the dependencies of the current versus perpendicular field in the parallel and the anti-parallel magnetized states of the leads. A significant field dependence of the current through the particle is observed in the anti-parallel magnetized state. However, only a very weak dependence is observed in the parallel configuration. These observations are interpreted in terms of Zeeman splitting of the energy levels, which causes the tunnel coupling between the levels in the particle and the ferromagnetic leads, to depend on the field direction.

3.2 Quenching of Electron Spin-Precession in a Metallic Particle

3.2.1 Spin Precession and Sample Size Effects

In this section we discuss electron tunneling from a ferromagnet into a normal metal particle in a non-collinear magnetic field. In order to understand the sample size effects on spin-precession, we will discuss in detail its microscopic mechanisms in a macroscopic sample. First we analyze the case where the magnetic field is perpendicular to the magnetization. In a ferromagnet in tunnel contact with a normal metal, the electron spins are oriented along the direction established by the exchange field. Consider an incoming electron at energy E and spin-up, reaching the tunnel barrier from the ferromagnet. Because the energy spectrum in a large sample is continuous, an electron can enter at any energy, with the only

restriction on E being imposed by the Fermi-Dirac distribution. Figure 18a displays the single-electron energy spectrum of a macroscopic normal metal sample in a magnetic field perpendicular to the magnetization of the leads.

It will be shown that the energy levels in the particle must be spin-degenerate for the spin precession effect to take place. In particular, for any state $|A>$ of the sample with spin pointing in the direction of the perpendicular field (say 'spin-up' or $|\uparrow>'$), there should be a state $|B>$ with opposite spin direction ('spin-down' or $|\downarrow>'$) and the same energy. The orbital wavefunctions of states $|A>$ and $|B>$ have slightly different wave-vectors k, so that the difference in their kinetic energy is equal to E_Z, the Zeeman splitting in the perpendicular field. Because of the continuity of the spectrum, it will be possible to find such a pair of orbital wavefunctions at any E_Z and E.

As a result, a spin-up electron can tunnel from the ferromagnet into the normal metal without changing its spin. There will exist a receiving state in the normal metal with spin-up, which the electron can occupy after tunneling. In that state, the degenerate states $|A>$ and $|B>$ in Fig. 18 are coherently mixed to produce the spin-up state at the injection point. If the Zeeman splitting is close to zero, the receiving state would be $(|A>+|B>)/\sqrt{2}$. More generally, in a perpendicular field one has to take into account differences in the orbital states, $|A>= u_{k_A}(\vec{r})|\uparrow>'$ and $|B>= u_{k_B}(\vec{r})|\downarrow>'$. Then the receiving state is $C_1|A>+C_2|B>$, where C_1 and C_2 are obtained from the condition that the receiving state be proportional to $|\uparrow>'+|\downarrow>'$ at $\vec{r}=\vec{r}_I$, where $\vec{r}_I$ is the injection point. In that case, spin is conserved in tunneling from the ferromagnet into the normal metal sample, and at finite bias voltage, the spin in the normal metal will accumulate along the magnetization direction, consistent with experiments [83, 6].

To understand spin precession in a normal metal, we follow the trajectory of an electron after it is injected from the ferromagnet. The electron will follow a diffusive path through the metal with a diffusion constant $D = v_F l/3$. The correlated electron with opposite spin will follow a similar diffusive path. However, due to the phase difference developed from their different wave vectors, the two electrons will only remain correlated over the correlation length, $L_C = \sqrt{D\tau_C}$, where $\tau_C = \hbar/E_Z$. On lengths less than this distance, the

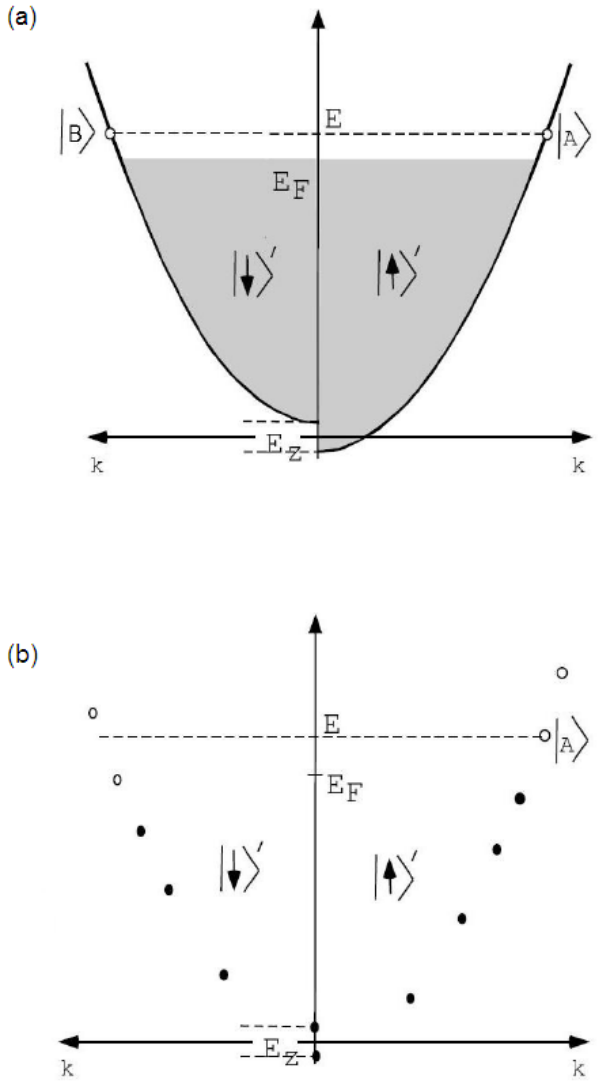

Figure 18: (a) Spin degeneracy of the energy spectrum of a macroscopic metallic sample in a perpendicular field. (b) Absence of spin-degeneracy in the energy spectrum of a metallic particle in a perpendicular field. The primes in the spin sub-bands indicate that spins are oriented along the direction of the applied magnetic field, rather than the magnetization direction in the ferromagnetic leads.

spins remain correlated, and longer than this distance, the phase shift turns spin up into spin down, resulting in spin precession. In this discussion we neglect spin-orbit scattering in the correlation region.

Going to nanometer scale particles, this picture changes dramatically. If $\delta > E_Z$, all energy levels are non-degenerate, as illustrated in Fig. 18b. Non-degeneracy prevents coherent mixing between 'spin-up' and 'spin-down' states to produce a receiving state with spin-up, leading to the quenching of spin precession.

In some cases electron spin precession can occur in the particle. Braun *et al* [18]. calculated the current through a normal metal particle in contact with ferromagnetic leads as a function of the magnetic field applied perpendicular to the magnetizations in the leads, which were collinear. Their model allows for the spin-up and spin-down states of the particle to mix coherently and considers the interplay between the Bloch equations and spin accumulation in the particle, as a result of spin-dependent tunneling. The model predicts spin precession of the accumulated spin in the particle.

The condition of Braun's model is that the Zeeman splitting in the particle be weak, $E_Z/\hbar < \Gamma$, where Γ is the electron tunnel rate between the particle and the ferromagnetic leads. In that regime the Zeeman split states are broadened by the tunnel coupling, making it possible to make coherent mixtures. This model is valid only at zero bias voltage, where sequential electron conduction can take place only if the background charge is $Q_0 = (n + 1/2)e$.

The samples measured here, are usually subjected to large bias voltages compared to δ/e and $E_Z/\hbar \gg \Gamma$, so the levels are not only non-degenerate, but also non-overlapping so there can be no coherent mixing between Zeeman-split levels. In that case, the contribution to electron current from different levels can be obtained using standard Coulomb Blockade theory, by summing the individual contributions of the levels incoherently, consistent with sequential electron tunneling [4, 14].

3.2.2 Non-Collinear Magnetic Fields

From now on we will assume that the magnetic field $\vec{B}$ can point in an arbitrary direction. We will consider a metallic particle in contact with two ferromagnets with collinear magnetizations. In the regime of well defined Zeeman levels of the particle, the tunnel rate between a level and the leads will depend on the direction of the magnetic field relative to the magnetizations.

In the ferromagnets, electrons move in an exchange field oriented along the z-axis, so the spinors in the ferromagnets are $|\uparrow>$ and $|\downarrow>$. The tunnel density of states at the Fermi level of the ferromagnet will be characterized by the spin polarization P. In the particle, the Zeeman splitting in magnetic field $\vec{B}$ defines spinors $|\uparrow>'$ and $|\downarrow>'$ as shown in Fig. 19a. The exchange field is negligible in the particle, because our tunnel barriers are thick.

It will be assumed that the spin is conserved in the tunneling process across any of the two junctions. In a non-collinear magnetic field, we use a spinor transformation $|\uparrow>'= cos(\alpha/2)|\uparrow> + sin(\alpha/2)|\downarrow>$ in the particle, where α is the angle between the magnetization of the leads and the applied magnetic field at the particle. If we consider the continuity of the wavefunction across the tunnel barrier, it will follow that the injection probability from the spin-up band into the state $|\uparrow>'$ is proportional to $cos^2(\alpha/2)$. Thus, the tunnel rate between level $|\uparrow>'$ and the spin-up band in the ferromagnet can be written as $\Gamma^i(1+P)cos^2(\alpha/2)$, where $i = L, R$ for the left or right lead, respectively. The factor $(1 + P)$ takes into account the spin-dependent tunnel density of states in the ferromagnetic leads. The injection from the spin up-band into $|\uparrow>'$ will be accompanied by a spin-down reflection, to satisfy spin-conservation. Similarly, the tunnel rate between $|\uparrow>'$ and the spin-down band is proportional to $sin^2(\alpha/2)$ and can be written as $\Gamma^i(1-P)sin^2(\alpha/2)$. The total tunnel rate between level $|\uparrow>'$ and lead i is obtained by summing over the spin-bands in the ferromagnet: $\Gamma^i_{|\uparrow>'}(\alpha) = \Gamma^i(1+P)cos^2(\alpha/2) + \Gamma^i(1-P)sin^2(\alpha/2) = \Gamma^i[1 + Pcos(\alpha)]$.

We obtain in a similar way that the total tunnel rate between level $|\downarrow>'$ and lead i is $\Gamma^i_{|\downarrow>'}(\alpha) = \Gamma^i[1 - Pcos(\alpha)]$. Thus, the overall effect of the field direction is to change the spin-polarization in the leads from P to an effective polarization $Pcos(\alpha)$.

It is important to mention that under a non-collinear magnetic field, electron tunneling between the ferromagnetic leads and the particle, could induce precession of the spin accumulated in the particle via spin torque [56], which is proportional to the tunnel coupling (Γ) between the leads and the particle. Due to the large tunnel resistance of our samples ($\sim G\Omega$), such tunnel coupling is very weak [33], and the effect of spin torque can be neglected in further analysis.

3.2.3 Spin Accumulation Mechanism

At finite bias voltage, the spin-dependent tunnel rates lead to spin-accumulation in the anti-parallel magnetized configuration [16, 96, 17]. In general, spin-accumulation arises when one spin direction is preferentially injected into the particle from one of the leads, while the other spin direction is preferentially drained to the other lead (see Figure 19). In this case, if the spin-relaxation time is longer than the electron dwell time on the particle, the excited particle states with one spin direction have a higher occupation probability compared to the states with opposite spin. As a result, the average spin-polarization of the particle will be nonzero.

In contrast, in the parallel magnetized configuration, one spin direction is both preferentially injected and removed, so the average spin polarization in the particle is zero. In this case, there is no spin accumulation at any α, because the effective polarization, $Pcos(\alpha)$, is the same on both leads. In other words, if the preference to inject one spin direction is reduced by $cos(\alpha)$, then the preference to remove that same spin direction, is also reduced by $cos(\alpha)$, so the spin accumulation will remain zero and the tunnel current, $I_{\uparrow\uparrow}$, should be constant, $I_{\uparrow\uparrow} = I_{\uparrow\uparrow,0}$.

As previously discussed, sequential electron tunneling through the particle in the anti-parallel magnetic state, will cause spin accumulation in the particle. The number of occupied 'spin-up' states, will be larger than the number of occupied 'spin-down' states, with the average spin of the particle pointing along the direction of the magnetic field. By exchanging P with $Pcos(\alpha)$ and using the spin accumulation model appropriate for our samples [91],

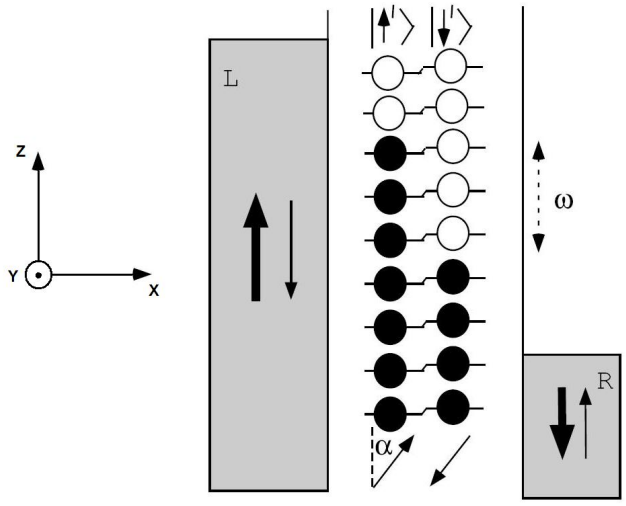

Figure 19: An excited state of the particle generated at finite bias voltage, fully relaxed with respect to spin-conserving transitions. Filled circles indicate occupied electron-in-a-box states. The spin expectation value is pointing along the magnetic field, which makes angle α with respect to the magnetizations.

we find

$$\Delta I = \Delta I_0 cos^2(\alpha) = \Delta I_0 \frac{B_z^2}{B_\perp^2 + B_z^2} \tag{14}$$

where $\Delta I = I_{\uparrow\uparrow} - I_{\uparrow\downarrow}$ is the difference in the current between the parallel and the anti-parallel magnetic configuration in the presence of the magnetic field, $\vec{B}$, and $\Delta I_0 = I_{\uparrow\uparrow,0} - I_{\uparrow\downarrow,0}$ is the difference in the current between the parallel and the anti-parallel magnetic configuration at zero magnetic field. Alternatively, $I_{\uparrow\downarrow} = I_{\uparrow\uparrow,0} sin^2\alpha + I_{\uparrow\downarrow,0} cos^2\alpha$.

Eq. 14 shows that in the anti-parallel magnetized state, the current versus angle α exhibits a minimum between $I_{\uparrow\downarrow,0}$ at $\alpha = 0$, and $I_{\uparrow\uparrow,0}$ at $\alpha = \pi/2$. This dependence reflects that the spin accumulation is reduced to zero when α varies from 0 to $\pi/2$. Moreover, the current depends only on the direction of the magnetic field, and not on its magnitude.

In macroscopic samples, spin precession would cause $I_{\uparrow\uparrow}$ versus perpendicular field to exhibit a maximum at $\alpha = 0$ [46]. Additionally, in the presence of spin precession, there is a characteristic field scale at which the precession period is equal to the electron transit time. The absence of field dependence in $I_{\uparrow\uparrow}$ combined with the field dependence in $I_{\uparrow\downarrow}$ given by Eq. 14, suggests the quenching of spin precession in nanometer scale particles.

3.3 Discussion of Experimental Results

The selected samples have resistances near the conduction threshold, which virtually guarantees that the current between the leads is flowing via a single particle [90]. The Coulomb Blockade and, sometimes, spectroscopy of energy levels can be used to verify this tunneling condition. It turns out that even in samples with multiple particles at the tunneling junction, electron transport via a single particle is still possible, as long as the bias voltage is kept low.

Typical particle parameters are $D \approx 5nm$ for the diameter and $\delta \sim 1meV$ for the level spacing. The Al_2O_3 thickness was chosen so that the tunnel resistance is high ($\sim G\Omega$). In this case, the tunnel rate between the discrete levels and the leads is $\sim (R_Q/R) \cdot (\delta/h) \sim 1MHz$. This rate is comparable to the spin-relaxation rate involving an energy difference δ, allowing the use of transport measurements to explore the energy dependence of the spin-relaxation rate [90, 91].

At bias voltages above the CB threshold, the particle is fully relaxed with respect to spin-conserving transitions, as already discussed in *Section 1.2.3*. The particle can still remain in an excited state at time scales of $1/\Gamma$ provided that the excited states relax only by a spin-flip transition. Spin-polarized excited states, such as the one in Fig. 19, are responsible for spin accumulation and spin-polarized current [91]. Figure 20a displays the I-V curve of one device at $4.2K$, which exhibits CB. In addition to the conduction thresholds indicated by the letters a and b, there are thresholds at higher bias voltages where the slope of the I-V curve increases sharply, as indicated by the letter 'c' at positive voltage. At the threshold voltages, additional charged states of the particle become energetically available for tunneling, consistent with CB formalism [4].

3.3.1 Bias Voltage and Saturation of the Spin-Polarized Current

In this section we discuss the spin-valve effect in sequential electron tunneling through the particle. We also present additional data confirming previous observations of saturation of spin-polarized current with bias voltage [90, 91]. The discussion is placed within the context of magnetoresistance oscillations (MRO) in the single-electron charging regime [5,

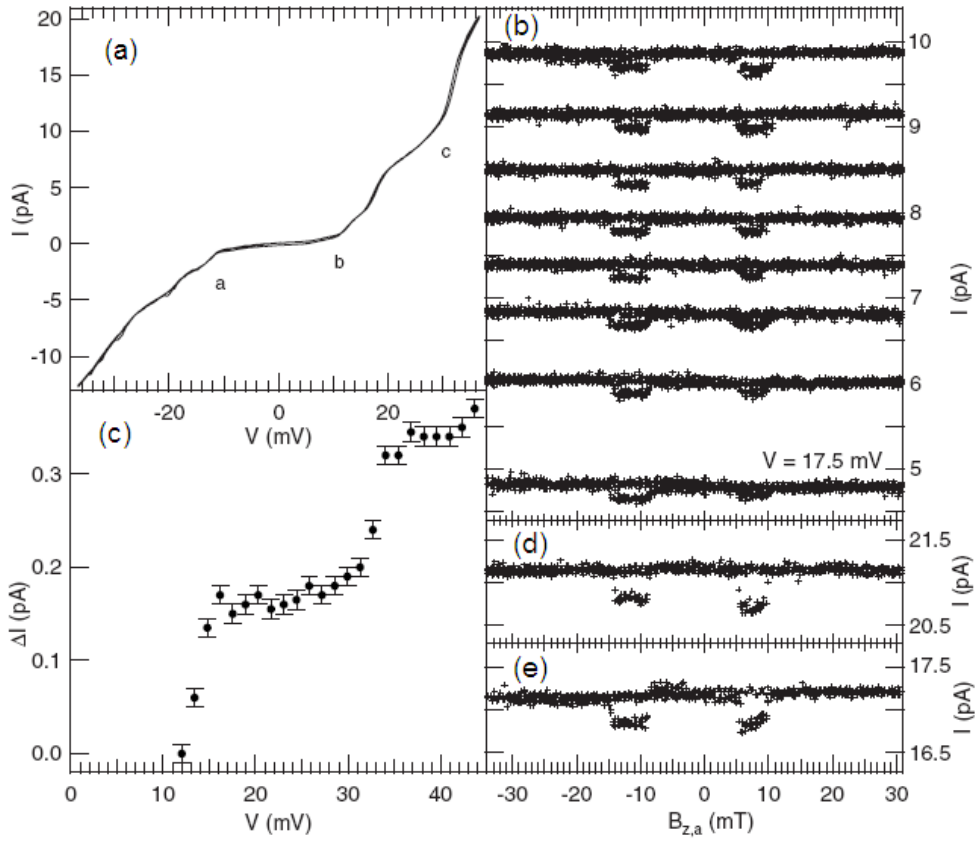

Figure 20: (a) I-V curve. (b) I versus $B_{z,a}$, with increasing bias voltage. (c) $\Delta I = I_{\uparrow\uparrow} - I_{\uparrow\downarrow}$ versus V. (d) and (e) I versus $B_{z,a}$ at $V = 35mV$ and $V = 40mV$, respectively. All data taken at $T = 4.2K$.

65], emphasizing the difference between both effects.

Fig. 20b displays current versus parallel applied field $B_{z,a}$. The magnetic field is swept four times in the positive and negative directions, for each one of eight different values of bias voltages, spaced by $1.4mV$ from each other. The dependencies show the spin-valve effect, displaying two magnetic transitions for each direction of the sweeping field. In a magnetic transition, the magnetic configuration switches between parallel and anti-parallel, resulting in the current change $\Delta I = I_{\uparrow\uparrow} - I_{\uparrow\downarrow}$. For every different value of the bias voltage, the magnetic transitions show high reproducibility between repeated scans. In Fig. 20b, $\Delta I \approx 0.17pA$, is nearly independent of V in the voltage interval between $17.5mV$ and $27.3mV$.

ΔI versus V over a broader voltage range is shown explicitly in Fig. 20c. From $V = 0$ to $V = 32mV$, ΔI displays saturation. We also measure the spin-valve signals at negative bias voltage and find the same behavior in ΔI versus V with the same magnitude of ΔI. By comparison, in ideal single magnetic tunnel junctions, ΔI would be linear with bias voltage within the range shown in Fig. 20b. For that reason, single tunnel junctions are normally characterized by the tunnel magnetoresistance, $TMR = \Delta I/\mathrm{I}_{\uparrow\uparrow}$, which is independent of V in ideal junctions [49]. The saturation of ΔI versus V has been reported before, with saturation occurring within the first few discrete energy levels available for tunneling above the CB-threshold voltage [90, 91]. The saturation was explained by a rapid decrease in spin-relaxation time T_1 versus energy difference, ω, in a spin-flip transition. The rate of these transitions $1/T_1(\omega)$ increases rapidly with ω. At low bias voltage measured from the CB-threshold voltage, Fig. 19 shows that the range of excitation energies of the particle will be small because that range is proportional to the voltage. In this case, $1/T_1(\omega) < \Gamma$ for any ω, so ΔI will be linear with $I_{\uparrow\uparrow}$ and TMR will be constant. As the voltage increases, the range of ω also increases and ΔI saturates when there is an ω for which $1/T_1(\omega) \sim \Gamma$. A self-consistent calculation of the saturation parameters, can be performed using the model developed in Ref. [91], leading to an estimate of $T_1(\delta) \approx 1\mu s$. ΔI versus V in Fig. 20c exhibits another increase at $V \approx 32mV$. The dependencies I versus B_z at $V > 32mV$ are shown in Figs. 20d and 20e. ΔI in these figures is approximately two times larger than ΔI in Fig. 20b. The data in Figs. 20b-e are observations of a stepwise increase in the spin-polarized current with bias voltage through a metallic particle. The increase in ΔI occurs at the conduction threshold voltage 'c' in Fig. 20a. At that voltage, an additional charged state becomes energetically available for electron tunneling and starts to contribute significantly to electron transport. So, adding a new charged state also adds a new channel for spin-polarized transport. This second step observed in ΔI is explained as follows: At the threshold where the additional charged state becomes energetically available, there is insufficient energy to generate internally excited states in the particle, since the chemical potential in the source is equal to the charging energy for this additional charged state. Therefore, the particle in the additional charged state must be in the ground state. If the

voltage is slightly larger than the threshold voltage, then the internal excitation energy ω will also be small for this new available state and the condition $1/T_1 < \Gamma$ will be satisfied again leading to spin accumulation.

One alternative explanation of the saturation effect in ΔI would be that it is caused by the magneto-Coulomb effect [83, 88]. In this effect (see section 1.2.4), magnetization switching could induce a shift in the I-V curve along the V axis, due to a change in the background charge, ΔQ_0, of the particle. However, such effect can be ruled out by measuring the spin-valve effect in the regime of resolved discrete energy levels [91]. In particular, the spin-valve effect was measured at voltages where the current was not sensitive to small Q_0 shifts. As an additional assurance, we can estimate the magneto-Coulomb Q_0 shift in our sample: $|\Delta Q_0/e| \sim PE_Z/E_C \sim 10^{-5}$, where E_Z is the Zeeman energy at the coercive field ($\sim 10mT$) and E_C is the charging energy ($\sim 10meV$). This Q_0 shift is very small because of the large charging energy. It would cause a shift in the current of about $0.1fA$ while the measured value is $\Delta I = 0.17pA$. So the contribution to ΔI from the magneto-Coulomb effect can be neglected.

The saturation and stepwise increase of ΔI versus bias voltage, can also be analyzed in terms of the MRO in ferromagnetic single-electron transistors [5, 65]. If both the particle and the leads are ferromagnetic, then magnetoresistance oscillations arise from a combination of two effects: nonlinearity of the I-V curve in the CB and the spin-dependent tunnel resistance. The nonlinearity depends on the tunnel resistances since they vary between the parallel and anti-parallel magnetization configurations. The magnetoresistance will then exhibit oscillations with bias voltage in the range where the I-V curve is nonlinear. It has been predicted that MRO can also take place in a normal-metal particle in tunnel contact with two ferromagnetic leads, under the condition that the spin accumulation in the normal-metal particle is present [15, 5, 95, 59, 94]. In MRO with long spin-relaxation time, magnetoresistance remains within the same order of magnitude over a range of voltages involving several steps of the Coulomb staircase [95]. In our samples, the saturation of the spin-polarized current occurs within the first few discrete energy levels available for tunneling above the CB-threshold voltage [90]. At bias voltages above the saturation voltage,

the TMR decreases as $1/V$. Moreover, TMR in our samples becomes strongly suppressed within the first step of the Coulomb staircase, in contrast to the MRO effect with long spin-relaxation time where TMR remains within the same order of magnitude. So, the saturation of the spin-polarized current observed in our samples cannot be explained by the MRO effects without taking into account the energy dependence of the spin-relaxation time. Our samples have generally strong asymmetry of the tunnel junction resistance [90, 91]. In that case, for a typical sample the I-V curve above the CB-threshold voltage is linear at one sign of the bias voltage. We observe the saturation of ΔI with V at voltages where the I-V curve is linear and where the MRO effect should be weak. If the bias voltage is reversed and the I-V curve is nonlinear, the MRO effect could affect our spin-valve signal. However, we find that even in the nonlinear regime, ΔI saturates rapidly with bias voltage. Since the MRO vary with the energy scale set by the charging energy and our saturation effect is characterized by the energy scale comparable to δ [90], this is a further indication that the MRO cannot explain our observations.

Depending on the sign of the bias voltage, MRO may play a role in the spin-valve effect in our samples. However, the rapid saturation of the spin-polarized current with bias voltage cannot be explained by the MRO without taking into account the energy dependence of the spin relaxation time, which has the strongest effect on the bias voltage dependence of the spin-valve signal.

3.3.2 Effects of a Non-collinear Applied Magnetic Field

In this section we investigate how a non-collinear magnetic field influences spin-polarized current through the particle. The magnetizations are set into the anti-parallel configuration using the spin-valve signal. Figs. 21a and b display current versus magnetic field applied along the x-axis, $B_{x,a}$, with the field being swept back and forth. The x-axis is indicated in Fig. 19b.

The curve I versus $B_{x,a}$ exhibits a minimum in the anti-parallel configuration and weak dependence in the parallel configuration as can be seen in Figs. 21a, b, and c. The minimum center is offset, and its amplitude, $\approx 0.05pA$, is smaller than $\Delta I = 0.17pA$ measured in the

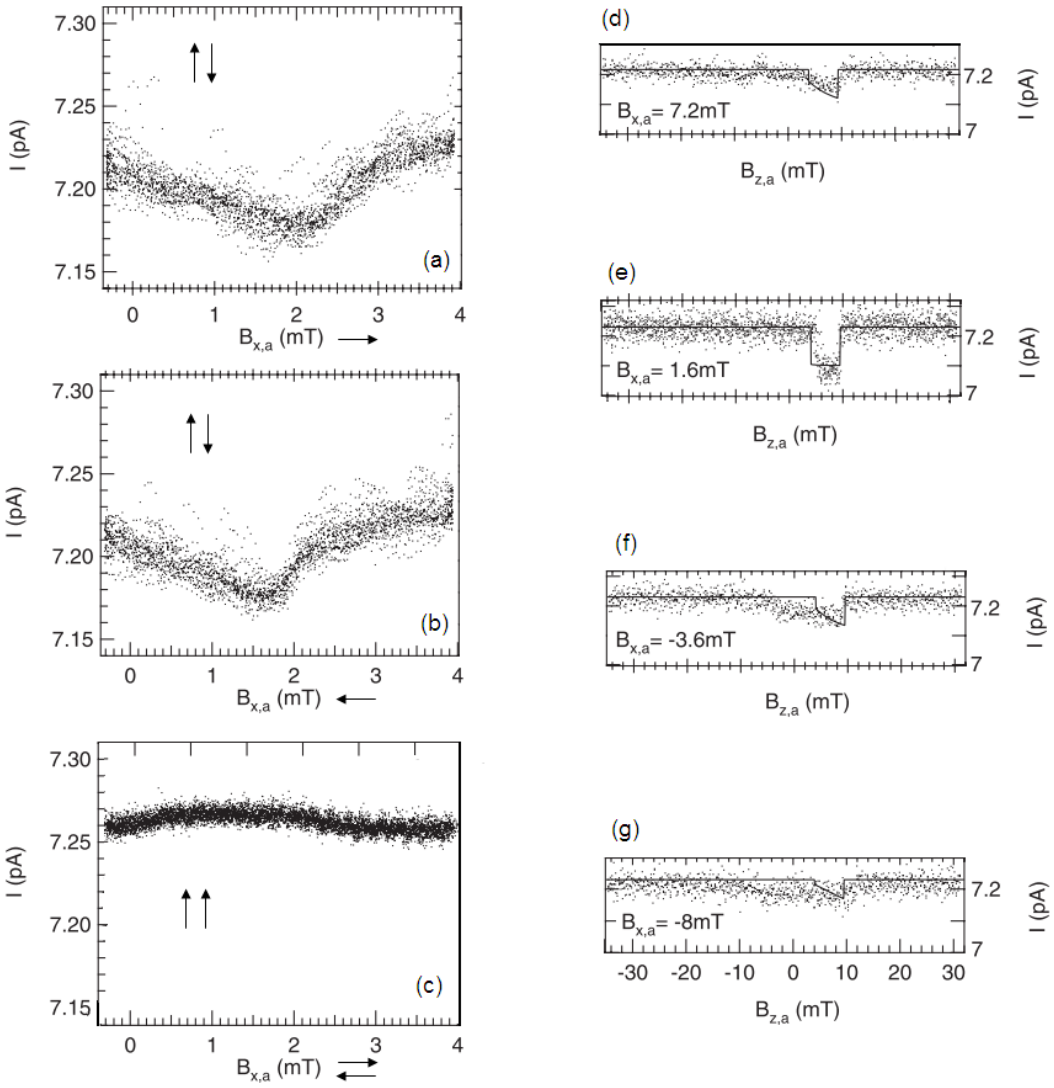

Figure 21: (a) and (b): $I_{\uparrow\downarrow}$ versus $B_{x,a}$, for increasing and decreasing $B_{x,a}$, respectively, at $B_{y,a} = B_{z,a} = 0$. (c): $I_{\uparrow\uparrow}$ versus $B_{x,a}$, at $B_{y,a} = B_{z,a} = 0$. (d)-(g): Suppression of the spin-valve signal with perpendicular applied field. T=4.2K in all figures.

spin-valve signal shown in Fig. 20. Comparing Figs. 21a and b, the minimum is reversible with magnetic field, although there is a weak hysteresis of $\approx 0.2mT$.

The spin-valve signal is suppressed in the presence of $B_{x,a}$, as shown in Figs. 21d, e, f, and g. The strongest spin-valve signal, Fig. 21e, is measured around the minimum field in Figs. 21a and b. For strong fields, Figs. 21d, f, and g, show the magnetic transitions from parallel to the anti-parallel magnetic state getting significantly weakened; as $B_{z,a}$ approaches the magnetic transition from anti-parallel to the parallel state, there is now a gradual decrease in current. These transitions remain resolved, but they get weakened proportionally to the magnitude of the perpendicular field, indicating that the characteristic perpendicular field that weakens the spin-valve signal is much larger than the width of the minimum in Fig. 21a and b.

Rotation of the magnetization of the leads, could be a possible cause for the dependencies shown in Fig. 21. For example, such rotations could induce a flip from the anti-parallel to the parallel configuration, leading to a minimum in I versus $B_{x,a}$. Starting from the parallel configuration, these rotations might not be able to vary the angle between the magnetizations, resulting in no dependence with perpendicular field.

However, consider the family of spin-valve signals measured at different fixed values of $B_{x,a}$ shown in Fig. 22. These curves were taken within the field range of the minimum in Figs. 21a-b and they were offset by $0.36pA$ from each other for clarity purposes. The fact that the spin-valve effect is weakly affected by $B_{x,a}$, demonstrates that the parallel and anti-parallel configurations are stable in this field range, ruling out rotation of the magnetizations as the explanation for the dependencies in Fig. 21.

Now we analyze the dependencies in Figs. 21 and 22 using Eq. 14, where $\vec{B} = \vec{B}_a + \vec{B}_l$. The fields $\vec{B}_a$ and $\vec{B}_l$ are the applied and the local field, respectively. $\vec{B}_l$ arises from the demagnetizing field generated by the leads, from the Earth's magnetic field, and from the stray fields in the laboratory. Initially, we assume that the local field is static. In the section on electron dephasing we will consider a case when the local field has a time-dependent fluctuating component. ΔI_0 in Eq. 14 is obtained as the maximum value of $I_{\uparrow\uparrow} - I_{\uparrow\downarrow}$ as a function of parallel and perpendicular applied fields in Fig. 22.

The amplitude, the full-width-half-minimum, and the center of the curves in Fig. 21a-b should correspond to $\Delta I \frac{B_{z,l}^2}{B_{z,l}^2+B_{y,l}^2}$, $2\sqrt{B_{z,l}^2+B_{y,l}^2}$, and $-B_{x,l}$ respectively from Eq. 14, which leads to $\vec{B}_l = (-1.8mT, \pm 0.63mT, \pm 0.41mT)$.

Next, using this local field, Eq. 14, and the value of ΔI_0 obtained as described above, we calculate the spin-valve signal, using fixed coercive fields in the leads of 4 and $9mT$. The results of the calculation are indicated by the solid lines in Figs. 21d-g, showing good agreement with Eq. 14, without any fitting parameters.

The reason that the spin-valve signal in Fig. 22 is weakly affected by the perpendicular field, compared to Figs. 21a-b (where $B_{z,a} = 0$), is that in the spin valve signal, $B_{z,a}$ is large compared to $B_{x,a}$ in the anti-parallel magnetic configuration. Fig. 22c displays the spin-valve signal versus increasing $B_{x,a}$ calculated from Eq. 14 as explained above, showing that the perpendicular field in Fig. 22 is weak to suppress the amplitude of the spin-valve signal. The calculation for decreasing $B_{x,a}$ leads to the same conclusion.

Since the dominant component of $\vec{B}_l$ is along x, this suggests that the local field is generated by a domain magnetized along the x-direction, in the vicinity of the particle. Such a domain would explain the hysteresis and asymmetry in Figs. 21a and b, if the domain wall moved in response to changing $B_{x,a}$. In that case the local field would not be completely independent of the applied field. Hysteresis of the domain wall motion would lead to a hysteresis in $B_{x,l}$. The asymmetry of the minimum could also be attributed to the dependence of $B_{x,l}$ on $B_{x,a}$. But the hysteresis in $B_{x,l}$ is only $0.2mT$, which is about 10%. So, in the lowest order of approximation, it can be assumed that the local field is constant in our applied field range.

3.3.3 Fluctuations in the Local Magnetic Field

The analysis of the results so far has neglected spin dephasing in the particle. In a single metallic particle, the dephasing could be caused by temporal fluctuations of the magnetic field, which can randomize the spin angle with respect to the z-axis.

One common source of spin dephasing in quantum dots is the hyperfine field of the nuclei. An electron spin in an Al particle interacts with N nuclear spins, where N is the

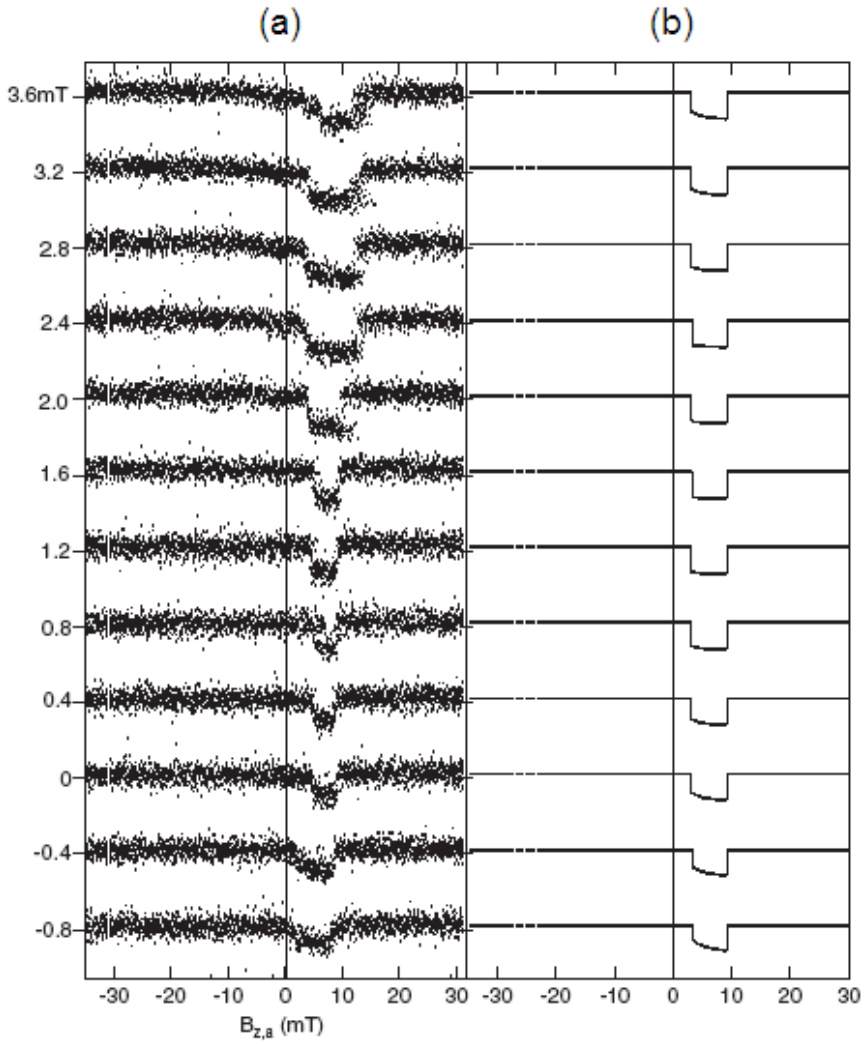

Figure 22: (a) Spin-valve signals versus weak perpendicular field $B_{x,a}$, for decreasing and increasing $B_{z,a}$, respectively, at $T = 4.2K$. (b) Calculated spin-valve signal corresponding to (a).

number of Al atoms in the particle. Those nuclear spins can be assumed random and uncorrelated, in which case the total hyperfine field summed over the nuclei has a Gaussian distribution with standard deviation $\sim \sqrt{N}$. The sum has to be weighted by the magnitude square of the electron wavefunction at the nuclei, which is $\sim 1/V$, where V is the particle volume. So, the hyperfine field scales proportionally with $1/\sqrt{N}$; the larger the particle, the weaker the fluctuating hyperfine field.

In this discussion we will assume that the fluctuating field varies slowly compared to the tunneling rate and fast compared to the time that the current is measured ($\sim s$). This assumption is usually satisfied in GaAs quantum dots. In that case, the tunnel-in and tunnel-out rates between the particle and the leads follow the direction of the fluctuating field adiabatically. The measured current can be obtained by averaging over the Gaussian distribution of the fluctuating field,

$$\Delta I(\vec{B}) = \Delta I_0 \int \frac{d^3\vec{B}'}{(\sigma\sqrt{2\pi})^3} \exp\left(-\frac{\vec{B}'^2}{2\sigma^2}\right) \frac{(B_z + B'_z)^2}{(\vec{B}+\vec{B}')^2}. \quad (15)$$

In this equation, σ is the standard deviation of a component of the fluctuating field, assumed to be the same for x,y, and z components. It sets the characteristic field scale for the angular dependence of the spin-polarized current.

We have calculated the integral in Eq. 15 numerically and obtained the magnetic field dependence. Figure 23a displays $\Delta I/\Delta I_0$ versus perpendicular field B_x/σ, at different values of parallel field: $B_z/\sigma = 0, 1, 2, 4, 6, 12$, and for $B_y = 0$.

In zero parallel field ($B_z = 0$), the spin-valve signal is reduced by 1/3 compared to the spin-valve signal in absence of the fluctuating field. Although the fluctuating field randomizes the spin-axis in the particle, the spin-valve effect is not reduced to zero. The reason is that the spin-valve signal is proportional to $cos^2(\alpha)$, where α is defined by the direction of the fluctuating field, and the average of $cos^2(\alpha)$ over the space angle is 1/3. The half-width-half-maximum (HWHM) of the dependence at $B_z = 0$ is 2.04σ, the same as that in the Gaussian distribution of the fluctuating field magnitude $\sqrt{B'^2_x + B'^2_y + B'^2_z}$ (HWHM=$\sigma\sqrt{6ln(2)}$). A parallel magnetic field reduces the effect of the fluctuating field on the spin valve signal, and $\Delta I/\Delta I_0$ approaches 1 when $B_z \gg \sigma$. In a parallel field, the

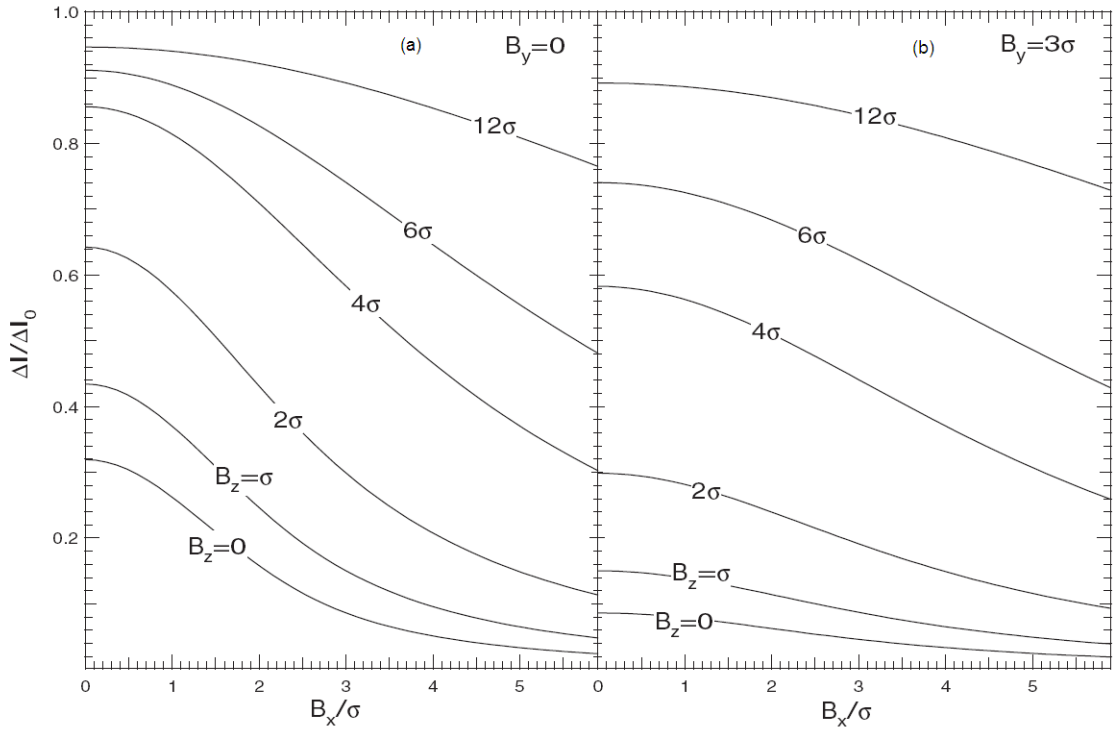

Figure 23: (a) and (b): Normalized spin-valve signal ($I_{\uparrow\uparrow} - I_{\uparrow\downarrow}$) versus perpendicular field B_x, for $B_y = 0$ and $B_y = 3\sigma$, respectively. Different curves correspond to different magnetic field parallel to the magnetization (B_z).

HWHM of $\Delta I/\Delta I_0$ versus B_x is $\sqrt{(2.04\sigma)^2 + B_z^2}$.

The dependencies of the spin-valve signal on B_x can also be changed by applying the field B_y, as shown in Fig. 23b, where $B_y = 3\sigma$. As a function of increasing B_y, the magnitude of $\Delta I/\Delta I_0$ is suppressed and the width of $\Delta I/\Delta I_0$ versus B_x is enhanced. Overall, HWHM $= \sqrt{(2.04\sigma)^2 + B_z^2 + B_y^2}$, for the dependence of the current on B_x.

Unfortunately, there is not enough information to determine both σ and the static local field, but it is possible to obtain a lower bound on σ, since HWHM$> 2.04\sigma$. Using the HWHM in Fig. 21a-b, we obtain $\sigma < 0.37mT$, or alternatively, the rms fluctuating field magnitude, $\sqrt{3}\sigma < 0.64mT$. Thus, the inhomogeneous dephasing time is $T_2^\star > \hbar/(g\mu_B 0.64mT) \approx 8ns$, which is enhanced compared to that in mesoscopic Al strips [43], and it is slightly larger than that measured in GaAs quantum dots [79].

CHAPTER IV

MAGNETORESISTANCE IN FNN DEVICES

4.1 Introduction

It is well known that electron transport through a normal metal between two ferromagnetic contacts can exhibit TMR, due to spin-accumulation in the normal metal [46]. An interesting point here is that although a single ferromagnetic contact is coupled to the particle, the TMR is still explained in terms of the spin-accumulation mechanism. In carbon nanotubes with a single ferromagnetic contact, TMR has been observed [45], but not explained. It is now recognized that magneto-Coulomb effects, can cause magnetoresistance when only one ferromagnetic contact is involved [30, 88]. However, it will be shown that the asymmetry in the TMR with respect to the bias voltage, can be used to rule out the contribution of magneto-Coulomb effects. This chapter describes an investigation of electron transport through a normal metal particle connected by tunnel junctions to a ferromagnetic lead, F, and to an Al lead. The observation of TMR in the regime of low magnetic fields and the main mechanisms behind it, will be discussed. The origin of the TMR in our samples is attributed to the collinearity between the electronic magnetic moments occupying the discrete energy levels of the particle, and the magnetic field in the particle. Therefore, the injection of spin-polarized current from F into the particle, will result in the accumulation of magnetic moments that are parallel to the local magnetic field at the particle and not to the magnetization of F. This local magnetic field includes the fringe field generated by F, which shows discontinuities whenever F undergoes magnetic transitions caused by an applied magnetic field. Consequently, the direction of the accumulated magnetic moment will also change discontinuously at these transition points, leading to discrete transitions in the TMR. However, as it will be shown later, the direction of the field can be continuously varied by applying a transverse static field, leading to continuous changes in the TMR.

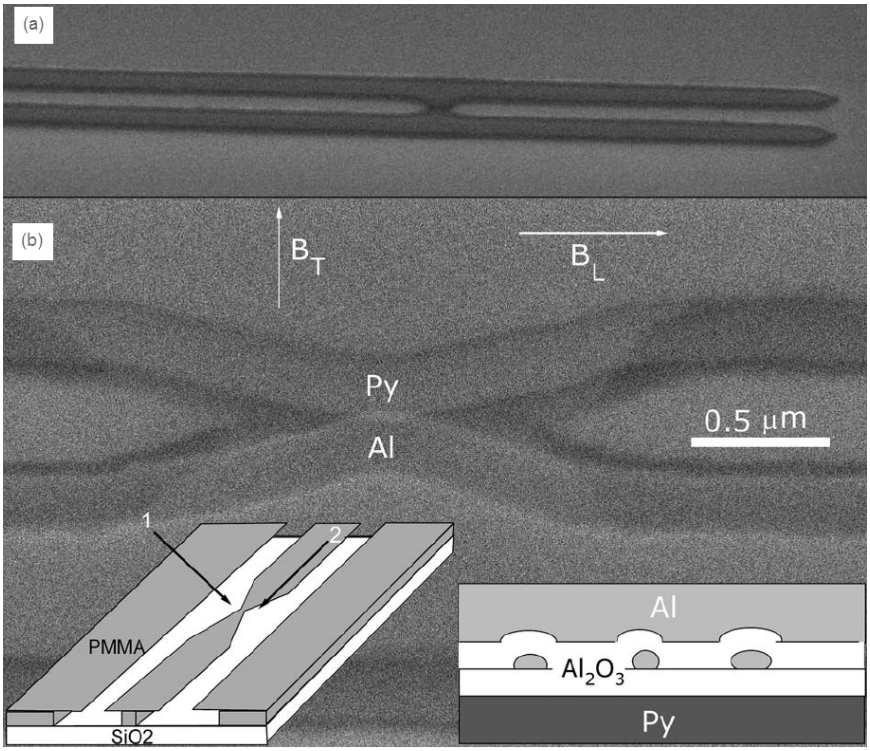

Figure 24: (a) Large scale SEM image of the device. The leads are $1\mu m$ wide. (b) Close-up image of the junction and magnetic field directions. Lower left inset: Sketch of the fabrication process. Lower right inset: Sketch of the overlap cross-section.

4.2 Experimental Results and Discussion

Fig. 24 displays a scanning electron microscope image of a representative FNN device. A larger scale structure is shown in Fig. 24a, with two needle-like $1\mu m$ wide leads, overlapping each other near half of the total length. Fig. 24b shows a higher magnification image of the overlap region, where the tunnel junctions and the particle are confined between the Permalloy (Py = $Ni_{0.8}Fe_{0.2}$) and the Al leads. The lower left inset shows the sketch of a shadow mask made of a bilayer resist (MMA/PMMA), using electron beam lithography, as described in Chapter 2. The I-V curves at $T = 4.2K$ and $T = 0.04K$, at zero applied magnetic field, are displayed in Fig. 25a. Both the Coulomb-Blockade (CB) region and the discrete energy levels are well resolved at $T = 0.04K$. The plot of conductance (dI/dV) versus bias voltage is shown in Fig. 25b, for positive (full line) and negative sweep directions (dotted line). The conductance traces are consistently reproducible along the voltage sweeps. It can clearly be seen that the spacings between discrete energy levels (indicated by

conductance peaks), are much larger than the CB-threshold voltage, which is $\approx \pm 0.002V$ for this sample, indicating that the background charge, Q_0, is close to $(n + 1/2)e$, where n is an integer. Under this condition, only one spin-degenerate level of a single particle is involved in electron transport at low bias voltage. Some of the energy levels display the BCS-gap in Al, which arises when the energy of a discrete level of the particle is aligned with the Fermi level in Al [80]. In that case, the level location in the superconducting state is larger than that in the normal state (at $B = 0.1T$), by an amount $(1+C_2/C_1)\Delta/|e|$. Here C_1 and C_2 are the capacitances between the particle and the Py and between the particle and the Al lead, respectively, and Δ is the BCS-gap. By comparing the locations of different levels at positive and negative bias voltage, as well as their shifts when Al is driven normal by the magnetic field, we confirm that the levels α and β have the same capacitance ratio $C_1/C_2 = 1.2$, while the BCS-gap is $\Delta = 0.157meV$. Additionally, we compare the locations of different levels before and after a small Q_0-shift, which confirms the values of C_1/C_2 and Δ. The average spacing between Al particles is $\sim$ 10nm [90], suggesting that there is more than one particle in the junction shown in Fig. 24. At low voltages, only the particle with a Q_0 closest to $(n+1/2)e$ would conduct; the other particles would remain in the CB-regime. Therefore, it should not be surprising that the levels at low bias voltage have equal C_1/C_2 ratios.

4.2.1 Electron Tunneling Asymmetry

In Fig. 25B, note that at negative bias voltage, the level α, which does not display the BCS-gap, is followed by a pair of levels β, which do display the BCS-gap; the level α occurs at a voltage where an electron tunnels from the Fermi level of F into the lowest unoccupied level of the particle. It is followed by a pair of levels β, which occur when the closest doubly occupied level, below α, starts to discharge an electron into the Al lead. The discharged electron can leave the particle via distinct excited states. Electron-electron interactions cause splitting of these states, and as a result, multiple conductance levels can be formed out of a single level [1].

The doubling of the second level β, is possible only if the number of electrons on the

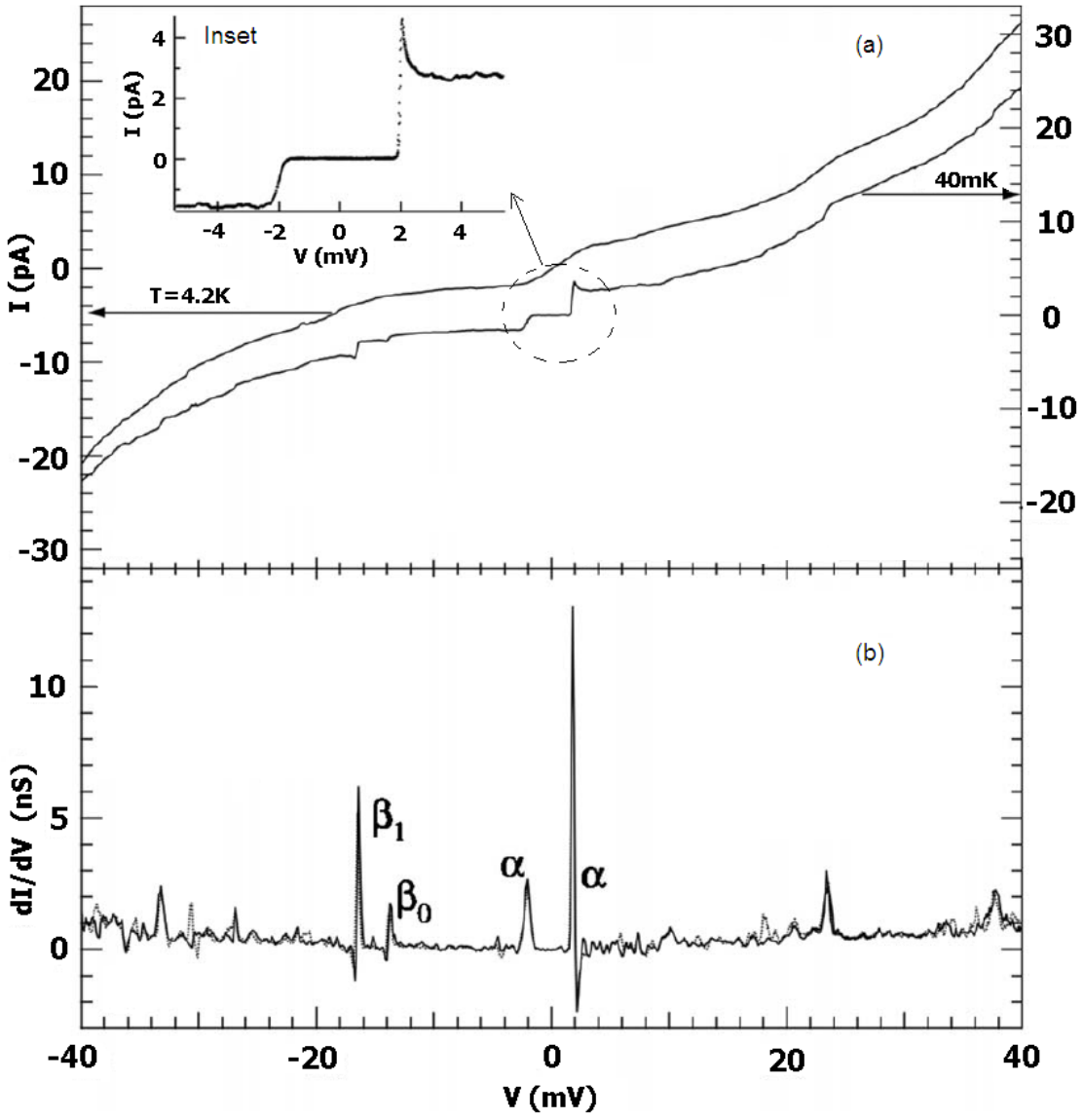

Figure 25: (a) I-V curves in the absence of an applied magnetic field. Inset: Close-up of the I-V curve at $T = 0.04K$ near the Coulomb Blockade voltage. (b) Conductance versus bias voltage. The levels are located at following bias voltages: $V(\alpha)$=1.97mV and -2.02mV,$V(\beta_0)$=-13.9mV, $V(\beta_1)$=-16.5mV. At these voltages, the current through the level reaches 50% of the current through the level at high bias.

particle in the CB-regime is even. In this case, the excited states generated by the electron discharge process, include both a spin-singlet and a spin-triplet states of the particle. These two states are exchange-split, causing the level β to duplicate. For the case of an odd number of electrons in the CB-regime, the excited states generated by the electron discharge process, as described above, would include states from a spin-doublet, and β would be a single level. The relation between parity and multiplicity can be confirmed by measuring the Zeeman splitting of the levels.

The sign of the bias voltage is crucial to understand the observed properties of the TMR. Figs. 26a-b show a sketch illustrating sequential electron tunneling via a discrete energy level of a particle for both signs of the bias voltage. In these figures, the number of electrons on the particle is even in the CB-regime, and an electron initially tunnels into the particle.

At positive voltage (Fig. 26a), the first tunneling step takes place when an electron tunnels from the Al lead. In the second tunneling step, an electron is discharged from the particle into F. In this discussion we neglected electron spin relaxation in the particle, since the spin relaxation time T_1 is in the μsec range [90, 91], which is longer than the electron discharge time into F, $1/\Gamma_F = 15$nsec, as obtained below. A spin-up electron discharges at a higher rate because of the larger density of spin-up states in F. As a result, the probability of the spin-up state of the particle being filled is smaller than that for the spin-down state, which is the basic principle behind spin accumulation on the particle.

If we consider the time average of the various tunnel events, electrons will discharge from a spin-polarized particle into the spin-polarized ferromagnetic lead. As a consequence, the current depends on P, the spin-polarization in F. Using the techniques outlined in Ref. [14], we find that the current through the particle can be expressed as

$$I = |e| \frac{2\Gamma_{Al}\Gamma_F(1-P^2)}{2\Gamma_{Al} + \Gamma_F(1-P^2)}, \tag{16}$$

where Γ_{Al} and Γ_F are the bare tunnel rates between a member of the doublet and the respective leads.

At negative voltage on F (Fig. 26b), an electron first tunnels into the particle from F.

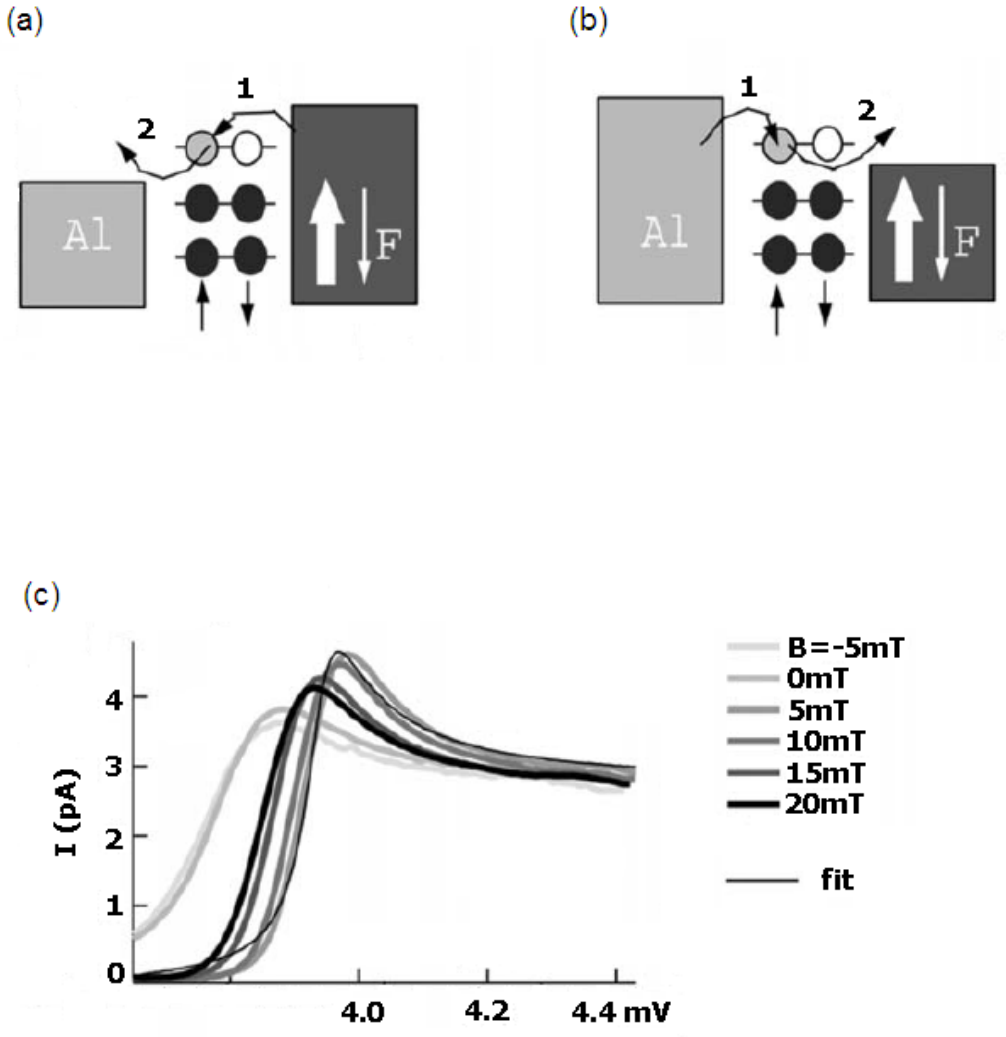

Figure 26: (a) and (b): Illustration of electron tunneling at positive and negative voltage on F, respectively. (c) Behavior of the BCS-gap for different applied magnetic fields.

Before tunneling, the particle is in an unpolarized singlet state and therefore, this tunneling process does not depend on P. This time we obtain

$$I = -|e|\frac{2\Gamma_{Al}\Gamma_F}{\Gamma_{Al} + 2\Gamma_F}. \tag{17}$$

The tunnel rates can be calculated using Eqs. 16, 17, and from the current at positive and negative bias voltages in Fig. 25b. In first approximation, we can neglect the P^2 term because the TMR is weak enough to do so. We find $\Gamma_F = 6.6 \cdot 10^7 s^{-1}$ and $\Gamma_{Al} = 1.1 \cdot 10^7 s^{-1}$.

4.2.2 TMR under a Transverse Applied Magnetic Field

Consider now the TMR measurements shown in Figs. 27a-d, where graphs of current versus applied longitudinal magnetic field (B_L), at zero applied transverse field ($B_T = 0$) are displayed. In order to compare the graphs in Fig. 27, all of the vertical axes were set to equal lengths. At positive bias voltage, Figs. 27a-b show discrete transitions in magnetoresistance at $B \approx -0.0075T$ and $B \approx 0.002T$. At these transitions, the current changes by ≈1.5%. At negative bias voltage, Figs. 27c-d indicate that the magnetoresistance is suppressed.

Figs. 27e-f show graphs of current versus B_L for $B_T = 0.01T$ and $B_T = 0.02T$, where B_T is applied perpendicular to the easy axis in the film plane. At negative bias voltage, the TMR remains suppressed, as shown in Figs. 27g-h. At positive bias voltage, TMR remains significant, with the width of the magnetoresistance signal getting enhanced proportionally to B_T.

The asymmetry in the P-dependence of the currents given by Eqs. 16 and 17 could explain the asymmetry in the TMR magnitude with bias voltage in Fig. 27. However, there is a caveat. If the magnetic reversal in F is modeled in a standard way, by changing from P to $-P$, the current in Eq. 16 would not change. In order to obtain the TMR, the magnitude of P in Eq. 16 needs to change with the magnetic reversal.

As discussed earlier, the electron magnetic moments in the particle are collinear with the magnetic field. The tunnel coupling between the spinors in F, collinear with the magnetization, and the spinors in N, collinear with the magnetic field, depends on α, the angle between these two vectors [12]. The overall effect on the current is that the effective spin

polarization to be used in Eq. 16 should be $Pcos(\alpha)$ instead of P,

$$I = |e| \frac{2\Gamma_{Al}\Gamma_F(1 - P^2cos^2(\alpha))}{2\Gamma_{Al} + \Gamma_F(1 - P^2cos^2(\alpha))}. \quad (18)$$

If α changes discontinuously at a magnetic transition, then the current given by Eq. 18 will also exhibit a discontinuity, consistent with the transitions in the TMR shown in Figs. 27a-b. In addition, as α varies continuously with B_L, a continuous change in current should occur, again in consistency with the TMR background. At negative bias voltage, the current does not depend on P and TMR is thus suppressed, in agreement with our measurements.

It is known that a magnetic transition in F can induce a chemical potential shift in F from the magneto-Coulomb effect related to a magnetoresistance transition [88]. A magneto-Coulomb based TMR would not exhibit significant asymmetry with bias voltage in our sample. In addition, we have measured TMR at voltages within plateaus of the I-V curves, as in Ref. [90], where the current is nearly constant and a chemical potential shift cannot change the current significantly. Chemical potential shift due to magneto-Coulomb effect, can be enhanced in ferromagnetic contacts with strong magneto-crystalline anisotropy [77, 10], which is not the case for Py.

In a finite B_T, the TMR remains suppressed at negative bias voltage. A full analysis of the transverse field effect on TMR at positive bias would require the disentanglement between changes in the fringe field and changes in the applied magnetic field, which was not possible to achieve within the capabilities of this experiment.

However, if the applied magnetic field is much larger than the fringe field, then the approximation $cos^2(\alpha) \approx B_L^2/(B_L^2 + B_T^2)$ is appropriate. In that case Eq. 18 predicts that the current through the particle has a *maximum* at $B_L = 0$, in agreement with Figs. 27e-f. The presence of this maximum as well as the suppression of the magnetoresistance at negative bias voltage, indicate that spin-accumulation described here is the mechanism underlying the magnetoresistance effect. The width of the magnetoresistance, $2B_T$, is also roughly in agreement with Fig. 27f.

The height of the peak is approximately twice the size of the magnetic transitions in

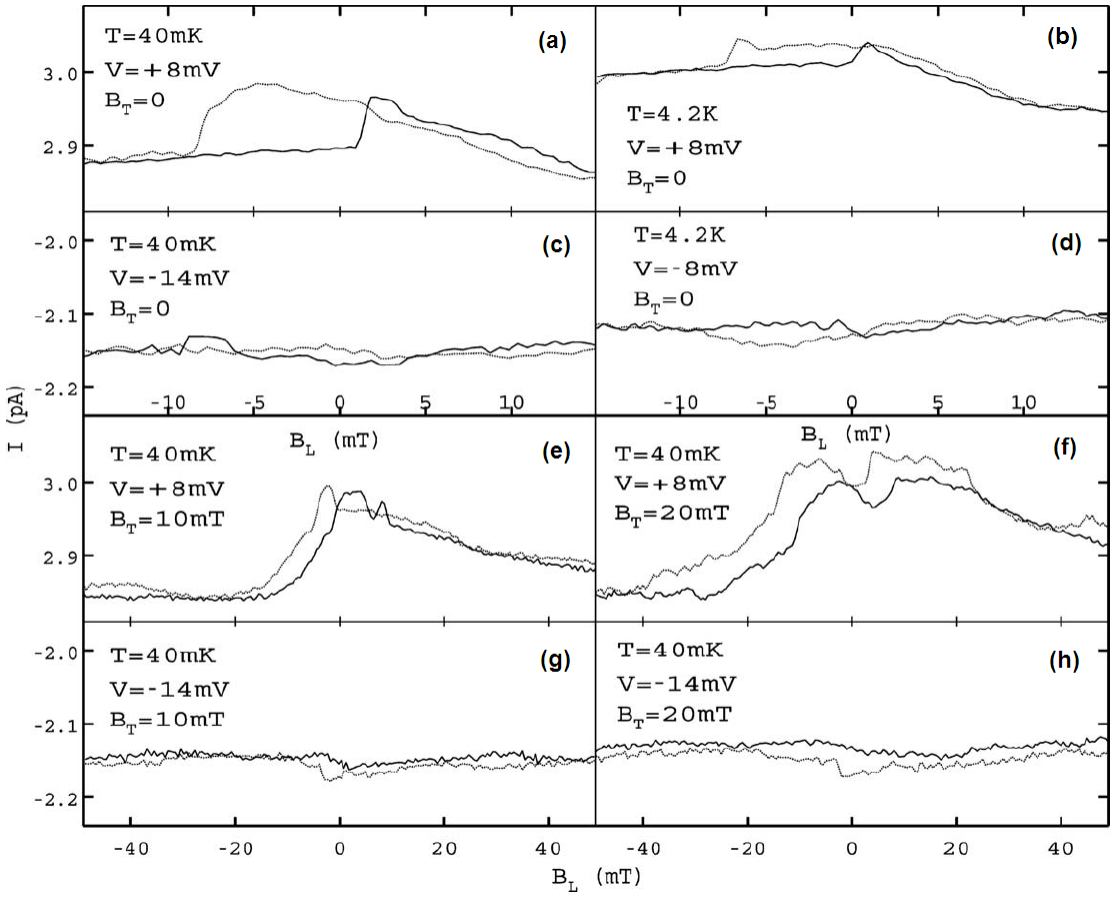

Figure 27: (a)-(d) Current versus longitudinal magnetic field at zero transverse magnetic field. (e)-(h): Similar measurement in the presence of a non-zero transverse magnetic field. Full (dotted) lines correspond to field sweeps in the positive (negative) direction.

Fig. 27a. By comparing the peak in Figs. 27e-f with the value predicted by Eq. 18, we can obtain the spin-polarization P of the tunnel density of states in $Ni_{0.8}Fe_{0.2}$. Now we can make use of $cos^2(\alpha) \approx B_L^2/(B_L^2 + B_T^2)$ at $B_L > 0.01T$, to obtain $P = 0.26$, which is consistent with the previously measured value $P \approx 0.28$ in tunnel junctions [69], but smaller than the $P \approx 0.37$ measured in $Ni_{0.8}Fe_{0.2}$ point contacts [48].

4.2.3 Estimate of the Fringe Field

In order to obtain a better understanding about the fringe field, we can study its pair-breaking effect on the BCS-gap. Measurements of the BCS-gap as a function of an increasing applied magnetic field B_L is shown in Fig. 26c. There was a small Q_0 shift between Figures. 26c and Figure 27, which caused level α to shift from $1.97mV$ to $3.89mV$. At the

applied fields of $-0.005T$ and $0T$, I versus V is measured before the magnetic transition at $0.002T$, while at $B_L \geq 0.005$, I versus V is measured after the transition. The BCS-gap has a clear discontinuity at the transition, indicating a discontinuity in the fringe field. Analogous behavior was observed around the magnetic transition in the reversed direction of the field sweep.

At $B_L \geq 0.005T$, the fringe field is weak because the BCS-gap is relatively large. We fit the data in Fig. 26c to the broadened BCS-density of states:

$$I = I_0 Re \frac{V - V_0}{\{(V - V_0)^2 - [(\Delta - i\gamma)(C_1 + C_2)/C_1]^2\}^{1/2}} \tag{19}$$

The gray line shows the best fit at $B_L = 0.005T$, with best-fit BCS-gap $\Delta = 0.155 \pm 0.007meV$ and broadening $\gamma = 21 \pm 0.7\mu eV$. We fit the entire family of curves in Fig. 26c well to this formula, using the same parameters I_0 and V_0, the level current and location, respectively, while Δ and γ are varied with B_L. For $B_L \geq 0.005T$, we find the BCS-gap is reduced at a rate $d\Delta/dB_L = -2.29meV/T$. Our BCS-gap is close to $\Delta_0 = 0.172meV$, the BCS-gap measured in Al particles with all Al leads, in zero magnetic field [80]. In our case, the magnetic field, at $B_L = 0.005T$, is estimated as $(\Delta_0 - \Delta)/|d\Delta/dB| = 0.009T$. Therefore, the fringe field is $\sim mT$, justifying the approximation for $cos^2(\alpha)$.

In conclusion, we demonstrated a spin-accumulation based magnetoresistance mechanism in a normal metal particle with a single ferromagnetic contact. If the magnetic field on the particle is not parallel to the magnetization, the injection of a spin-polarized current into the particle will result in the accumulation of the magnetic moment not being parallel to the magnetization of the ferromagnetic lead. Magnetoresistance arises from the magnetic field dependence of the angle between the accumulated magnetic moment and the magnetization. This simple mechanism needs to be considered when interpreting results in spintronics involving discrete energy levels.

CHAPTER V

MAGNETIC INTERACTIONS IN COBALT NANOPARTICLES

5.1 Introduction

Tunneling spectroscopy of discrete levels in metallic nanoparticles is a valuable tool to study electronic interactions in a metal. In normal metal nanoparticles, tunneling measurements have demonstrated that the low-lying electronic excitations are similar in character and spacings, to the particle-hole excitations in a noninteracting electron system. A few simple theoretical models [23, 54] have attempted to explain experimental observations [38] in the spectra of ferromagnetic nanoparticles, in terms of the coupling between particle-hole (p-h) and collective magnetization excitations in the particle [70]. As a result, their discrete energy spectrum is much more complex than usually predicted by an independent particle picture. The magnetic behavior of ferromagnetic nanoparticles can be significantly different than in the bulk material. In addition to finite size effects, the particle's electronic environment is also likely to play a fundamental role in the magnetic properties of such systems [93]. In this chapter, studies on the switching field dependence with respect to bias voltage and temperature will be presented, as well as possible interpretations of the observed results.

5.2 Experimental Results and Discussion

Our samples consist of Co particles tunnel-coupled with two Al leads via alumina barriers. The fabrication process has been described in Chapter 2. Summarizing, a PMMA bridge is defined by electron beam lithography over a SiO_2 substrate. First, we deposit 10nm of Al and 1.5-3nm of Al_2O_3, along direction 1 (see Figure 10). Then we oxidize the sample at room temperature in O_2 at 3mPa, for 30s. Next, we deposit 0.5nm of Co, 1nm-1.5nm of Al_2O_3, followed by 10nm of Al, all along direction 2. At such a small thickness (0.5nm), isolated Co particles are formed with 1-4nm in diameter and spaced by 2-5nm [38].

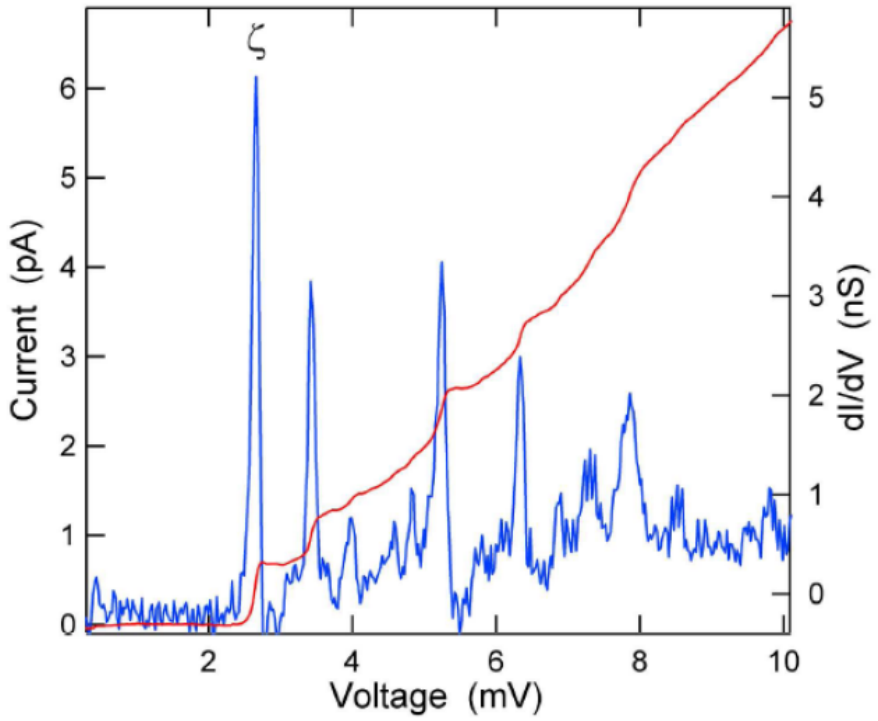

Figure 28: Current versus voltage (red) and differential conductance versus voltage (blue), at $T = 60$mK and zero magnetic field.

The current-voltage characteristics, $I(V)$, and the tunnel spectrum, $dI(V)/dV$, at $T =$ 15mK and zero applied magnetic field, are shown in Figure 28. Both the Coulomb blockade region and the discrete energy levels are well resolved. Discrete levels in Co particles have been studied extensively, both experimentally [38, 29], and theoretically [23, 54, 53, 24], with our measurements confirming the previous results. Figure 29 displays the magnetic field dependence of the energy levels, for decreasing and increasing magnetic fields, showing symmetric hysteresis about zero field. All of the levels are discontinuous at the switching field $|B_{sw}| \approx 0.3$T, indicating that they belong to the same particle. Note that the magnetic field dependence of the energy levels varies from level to level. This variation is known to be related to mesoscopic fluctuations (a few percent) of the magnetic anisotropy energy, giving therefore a fluctuating character to the switching field [29]. Analogous fluctuations, but in the *g-factors* for Zeeman splitting of energy levels in non-magnetic nanoparticles, have also been reported [66, 19], showing the importance of spin-orbit interactions, which also contribute to the anisotropy energy in ferromagnetic particles.

5.2.1 Tunnel Spectroscopy

The ground state spin (S_0) of the nanoparticle can be estimated either from the tunnel spectra or from the temperature dependence of the switching field. In tunneling spectroscopy of ferromagnetic nanoparticles, the spacing between the low-lying levels has been found to be smaller than the electron-in-a-box level spacing [38, 29]. This enhanced density of levels is well explained by a model that includes a phenomenological Hamiltonian and electron transport out of equilibrium [23, 54, 53]. This model assumes that non-equilibrium spin accumulation is responsible for the larger density of tunneling excitations, since it cannot be explained in terms of an independent-electron approach. First, we make use of this model to obtain S_0 from the average nearest-neighbor level spacing of the low lying levels, which is $\delta_{min} - U/2$ in Co [54, 53], where $\delta_{min} = 1.2eV/S_0$, is the electron-in-a-box spacing for the minority electrons and $U/2 = 1eV/S_0$ is the exchange energy divided by S_0. An alternative method uses the spacing between repeated levels in the tunnel spectrum. Level ζ in Figure 29 is repeated twice at negative voltage, because the magneto-fingerprint of that level

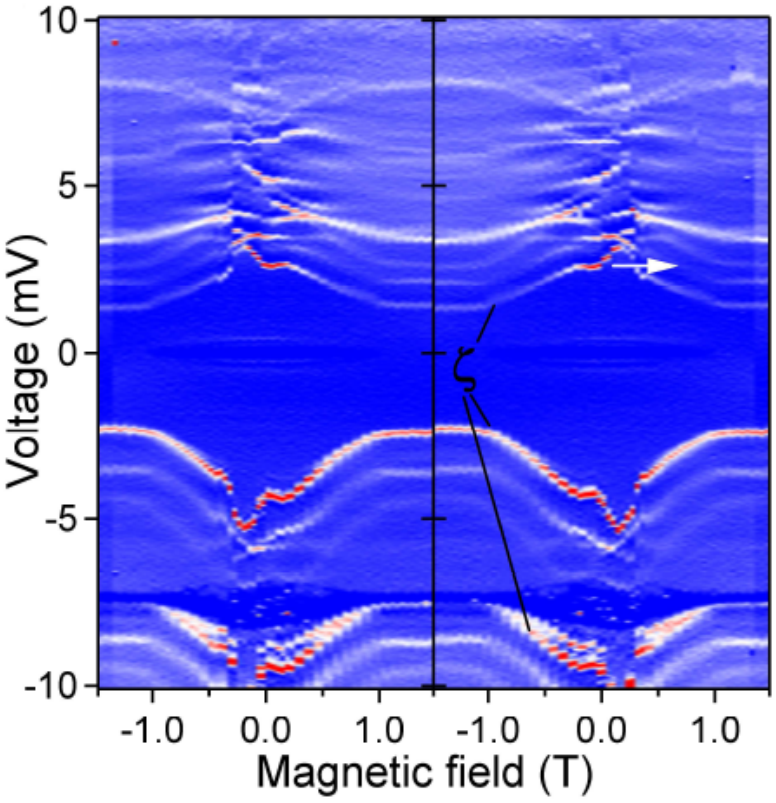

Figure 29: (a) Differential conductance of sample 1 versus magnetic field and voltage, at $T = 60$mK. The left and the right panel correspond to decreasing and increasing magnetic field, respectively. Blue (red) regions correspond to low (high) conductance. (b) Current versus magnetic field for sample 1 at voltage 2.4mV, showing the hysteresis loop at $T =$ 60mK, 2.4K, and 4.4K (bottom to top), with current offsets 0.2pA (for clarity).

is displayed twice. The repeated-level spacing should be $U/2$ [54, 53]. By using both the nearest-neighbor and the repeated-level spacing, we obtain $S_0 \approx 500$. The corresponding particle volume is $V = (1.9\text{nm})^3$.

The intrinsic switching field, defined as the switching field at zero tunnel current, is measured in the Coulomb blockade state. We set the voltage to 2.4mV and measure the magnetic hysteresis loop. In the vicinity of the switching field, we follow the path indicated by the white arrow in Figure 29. At low temperatures, if the magnetic field is just below the switching field, the particle will face Coulomb blockade. As the magnetic field is increased and reaches the switching field, a transition to a current-carrying state takes place. The magnetic hysteresis loop for three different temperatures is displayed in Figure 30, with the inset showing the temperature dependence of the switching field averaged over ≈30 field cycles. The error bars indicate the standard deviation of the switching field. The decrease of the switching field with temperature, accompanied by an increase in the standard deviation with temperature, indicates thermally activated switching [39, 35, 92]. By fitting the temperature dependence of the intrinsic switching field and the standard deviation, to the Néel-Brown model of magnetic reversal [74, 20, 92], we obtain $B_0 = 0.359 \pm 0.036$T for the switching field at zero temperature and $E_B = 20.6 \pm 2$meV for the anisotropy energy barrier. The fit of the switching field is shown by the solid line in Figure 31. We can estimate the "thermally activated" S_0 as $E_B/(g\mu_B B_0) \approx 500$.

5.2.2 Tunneling Effects on Magnetic Switching

Next, we investigate the effects of electron transport on magnetic switching at $T = 60$mK. Figure 32 shows that the magnitude of the switching field decreases with voltage. The phase diagram in Figure 33, corresponding to the increasing-field branch, displays the $I(B, V)$ dependence in detail.

During the measurement of $I(B, V)$, the magnetic field is cycled fast, while the voltage is varied slowly from 10mV to zero and back to 10mV. The phase diagram for the decreasing-field branch (after reflection about zero magnetic field) as well as for negative bias voltage, present similar behavior. The color scales in Figure 33, correspond to $I(B, V) - I_{bac}(V)$,

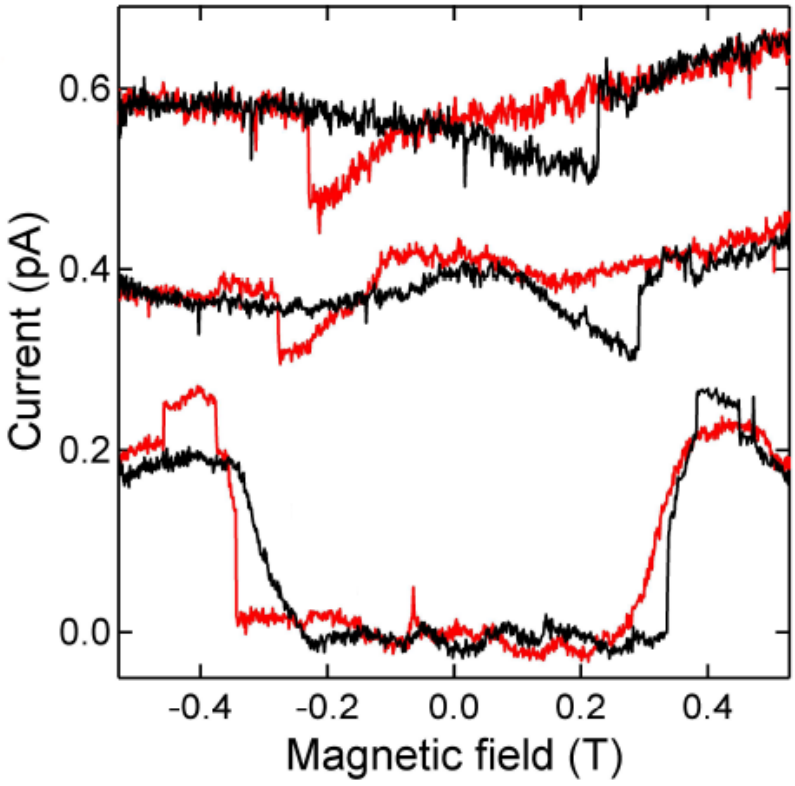

Figure 30: Current versus magnetic field at 2.4mV, showing the hysteresis loop at $T =$ 60mK, 2.4K, and 4.4K (bottom to top), with current offsets 0.2pA (for clarity).

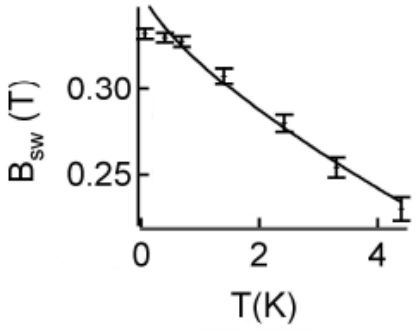

Figure 31: Swithing field versus temperature.

where $I_{bac}(V)$ is the average I-V curve ($I(B,V)$ averaged over B). This subtraction is performed because the changes in the current, caused by magnetoresistance, are much smaller than the ones caused by voltage. Therefore, this subtraction enhances the magnetoresistance contrast, making it easier to discern magnetic transitions at very small currents. Above the Coulomb blockade voltage threshold, the switching field (B_{sw}) decreases with voltage, as indicated by the yellow arrow. At 10mV, the switching field is reduced by 15%. The switching field decreases most rapidly near the Coulomb-blockade threshold.

5.2.3 Voltage-Induced Magnetic Swithing

This section describes how magnetization switchings can be induced by an applied voltage. The voltage and magnetic field parameters were adjusted according to the white line shown in Figure 33. The initial voltage was set to 2.4mV, below the Coulomb blockade threshold. This time, the phase boundary is crossed by applying a 10mV voltage pulse at a field $\sim 0.3T$, well before the positive switching field, and then comparing it with the unperturbed hysteresis loop. The inset in Figure 33 displays the two loops in the vicinity of the switching field. The red curve shows current versus increasing field, in the absence of the pulse. It is followed by the blue curve, showing current versus decreasing field. Next, while the field is increasing, the current versus magnetic field is measured in the presence of the pulse, as shown by the green line. Finally, the black line, which displays current versus decreasing field, completes the loop. The voltage pulse is able to switch the particle from

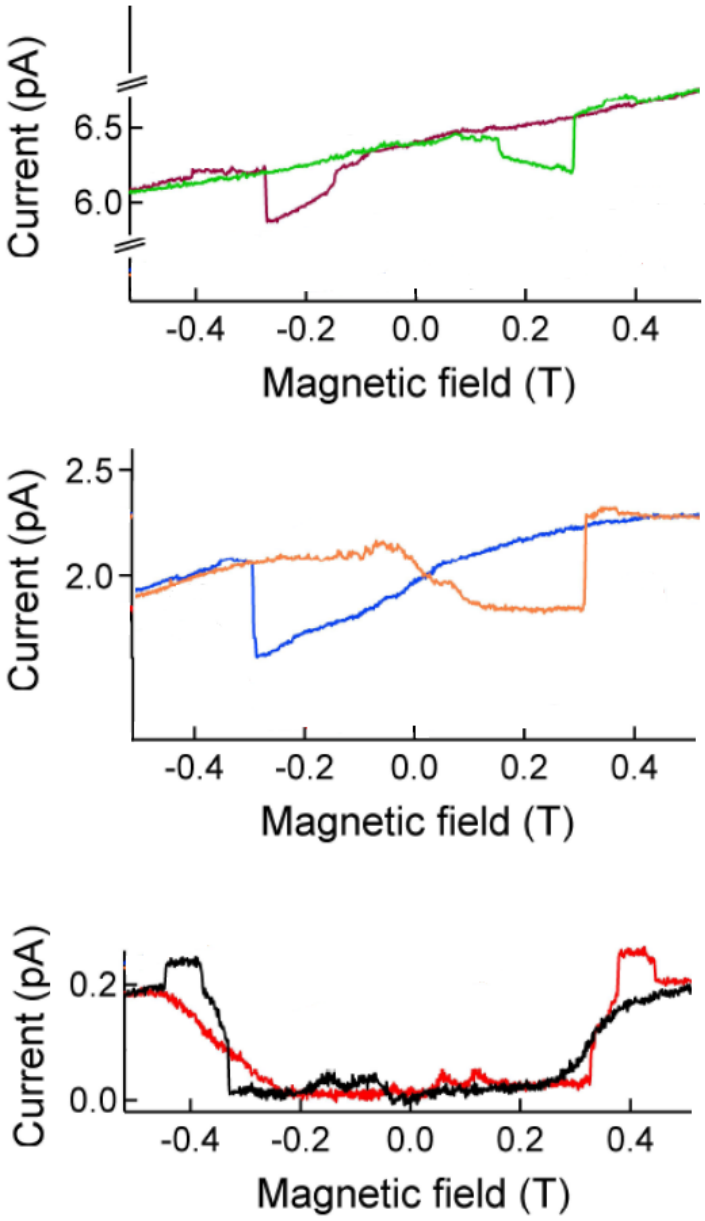

Figure 32: Current hysteresis loops at voltages 2.4mV, 5.2mV, and 10mV (bottom to top). Red, orange, and green: increasing-field. Black, blue, and brown: decreasing-field.

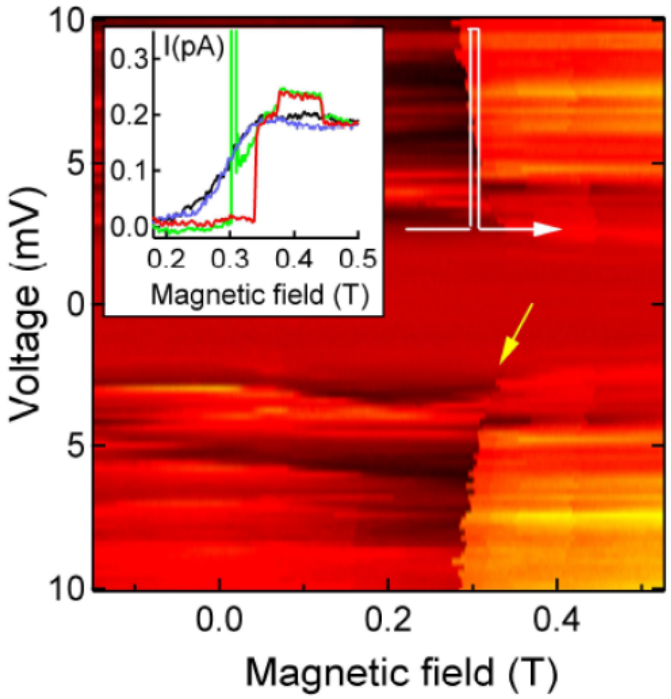

Figure 33: Color plot of the current versus magnetic field and voltage at $T = 60$mK. Darker areas correspond to lower currents. The yellow arrow indicates the slope in the switching field versus voltage. The white arrow represents a crossing of phase boundary induced by voltage. Inset: Hysteresis loops at $T = 60$mK zoomed-in near the switching field. Increasing and decreasing-field, without the voltage pulse (red and blue, respectively) and with the pulse (green and black, respectively).

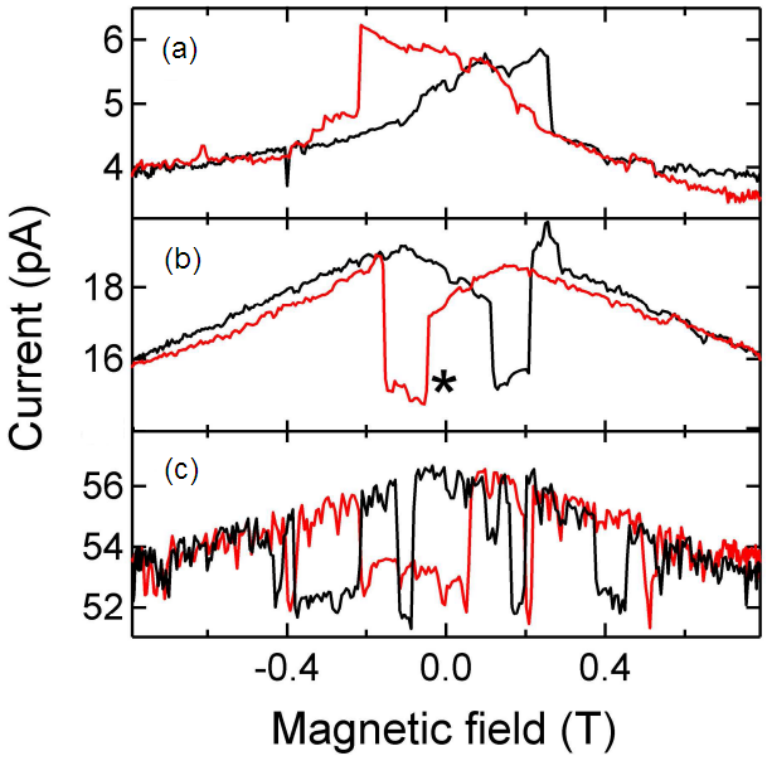

Figure 34: Hysteresis loop versus magnetic field for a different sample, measured at V = 26mV, 32mV, and 44mV, respectively. Black and red curves display the increasing and the decreasing-field branches, respectively.

the Coulomb blockade, into the current carrying state. When the voltage is set back to 2.4mV, the current settles around the magnetically reversed state, showing that the state of the particle has been switched. This procedure was repeated on three pairs of hysteresis loops and in the vicinity of the negative switching field as well, with the voltage-driven switching being confirmed every time.

Similar measurements were performed in several samples, with most of them showing significant reduction of the switching field as a function of voltage. A different sample showing a crossover from hysteretic to non-hysteretic behavior (superparamagnetism) at large bias voltages, is displayed in Figure 34.

In this sample, the particle diameter and the spin ground state are estimated to be 1.6nm and 160, respectively. The tunnel resistance at high voltage is about four times smaller than in the previous sample. At T = 60mK, the current-field hysteresis loop versus voltage is

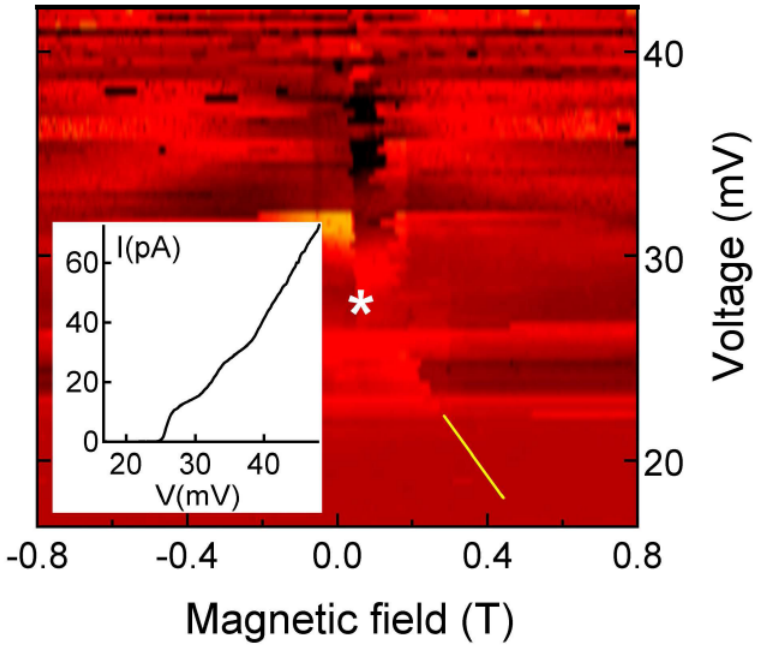

Figure 35: Color plot of the current versus magnetic field and voltage. Inset: I-V curve at zero field. The yellow line indicates the slope in the switching field versus voltage, at the Coulomb blockade threshold.

shown in Figures. 34a-c, and the phase diagram, along with the I-V curve, is displayed in Figure 35. Near the Coulomb blockade threshold, the switching field decreases rapidly with voltage, as in the other sample, slowing down at higher voltages. The magnetic hysteresis disappears completely above $\sim 38mV$, when the particle is in a superparamagnetic-like state. It exhibits telegraph noise, with the current randomly switching between the non-hysteretic, superparamagnetic background, and the current-induced magnetic state. In both samples, the hysteresis loop starts to display additional magnetic transitions, when the tunnel current is large, indicated by the stars in Figures. 34b and Figure 35. These transitions are current-induced, since they are absent at low voltages.

The reduction of the switching field versus bias voltage, suggests an interpretation that electron transport raises the magnon temperature above the sample temperature, through some form of Ohmic heating. This temperature difference can arise if electron spins in the particle are inefficiently coupled to the dissipative environment. According to this

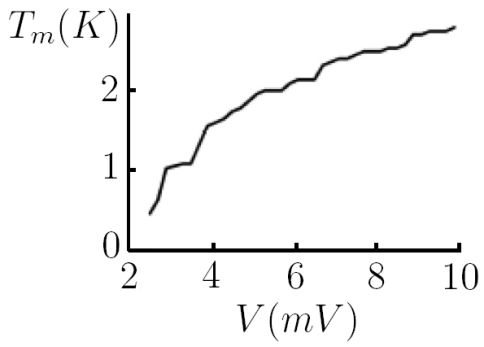

Figure 36: Effective magnon temperature versus bias voltage.

picture, the switching field serve as a "magnon thermometer", and the magnon temperature (Figure 36), $T_m(V)$, can be obtained by interpolating the temperature dependence of the switching field at the conduction threshold (Figure 31), to the switching fields measured as a function of V, at the lowest temperature, $T = 60$mK.

5.2.4 Concluding Remarks

The experiments presented in this chapter, aimed to study the behavior of magnetic hysteresis loops of Co nanoparticles as a function of temperature and bias voltage, showing that they can be very sensitive to sequential electron transport through the particle. As a consequence, the nanoparticle's magnetization can be switched by an applied voltage, via the coupling between spin collective modes in the particle and particle-hole excitations produced by electrons tunneling through the particle. Occasional crossings between spin and particle-hole excitation energies, can lead to entanglement between these two types of excitations [70]. In this regime, sequential electron-tunneling is able to excite spin collective modes in the particle, thereby reducing the switching field. According to this picture, the observed bias voltage dependence of the magnetic hysteresis loops, show significant magnon emission induced by electron tunneling. Further analysis is necessary to fully describe the mechanisms behind these intriguing effects.

CHAPTER VI

CONCLUSIONS AND FUTURE WORK

6.1 Microwave-Induced Switching

When it comes to spintronic practical applications, control over magnetization reversal in small magnetic grains, is a subject of great interest, from both fundamental and technical points of view. External magnetic fields can be used, with the inconvenience of requiring large current densities to be created. Application of microwave pulses, usually in the microwave range, could be a potential candidate for probing magnetization reversal dynamics in nanostructures. The use of microwave pulses have the advantage of being able to reverse magnetization of nanomagnets using much lower power at much shorter times. It is a valuable tool to probe magnetization dynamics in such small systems and it will definitely be useful as a complementary technique. In this chapter, preliminary experiments addressing radi-frequency (RF)-induced magnetization reversal in Cobalt nanoparticles, indicate a promising research route to be taken in future projects. As part of being preliminary results, it reflects the work involved in getting acquainted with new experimental procedures and equipment. However, the wide range of potential new experiments, opens a rich route for future research projects.

6.1.1 Experimental Procedures

As a first step, sample holders used in previous experiments had to be redesigned in order to accommodate the RF coupling to the device. The newer version includes a 2.4mm male connector, purchased from SRI connectors, which allows the transmission of microwave signals up to 50GHz. It also allows the sample to be mechanically stable and electrically connected to the semi-rigid coaxial line. In current experiments, the frequency range used is $< 10GHz$ and signal attenuation is not a concern. Figure 37 shows the new sample holder in detail.

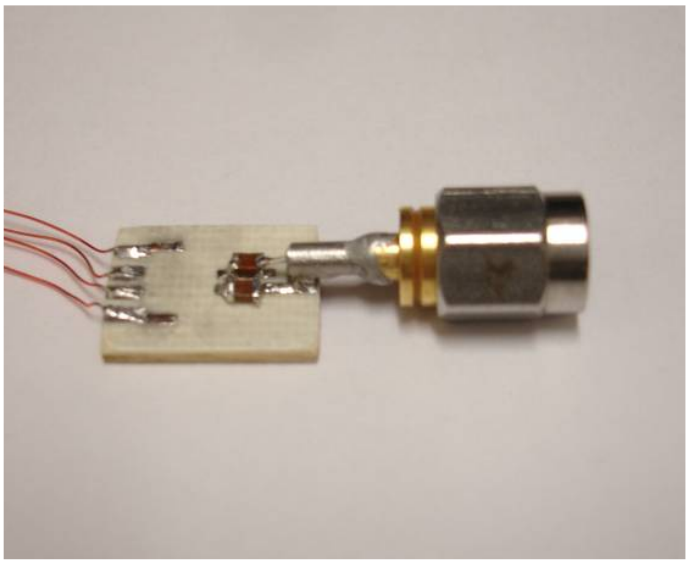

Figure 37: Sample holder adapted to allow the application RF pulses. A 2.4mm connector and a pair of 1pF mica capacitors have been added to support the new geometry of the devices.

In terms of the lithography pattern, changes also had to be made. Now, a straight thin wire ($\sim 100nm$ wide) is used as one of the electrodes and to carry the RF signal as well. This new geometry allows extra room for a second tunneling contact in the same device, as shown in Figure 38. The wiring between the chip and the sample holder still consists of fine Cu wire and indium dots as described in Chapter 2. Two $1pF$ CDE mica capacitors were added between the coax line and the sample as decoupling capacitors.

The RF signal is generated by a Synthesized Swept-Signal Generator (SSG), 0.01 - 40 GHz (Agilent, model 83640B), and the current/voltage measurements are performed as in previous experiments. An extra Function Generator (FG) is used as a "burst" modulator to trigger the microwave output. This is done by creating a single square pulse using the *arbitrary wave form* function of the FG. The FG burst output, which is triggered by a TTL signal, connects to the *pulse modulation input* of the SSG. The duration of a single pulse can be adjusted by changing its amplitude and the spacing between pulses can be controlled by changing the frequency of the TTL triggering signal.

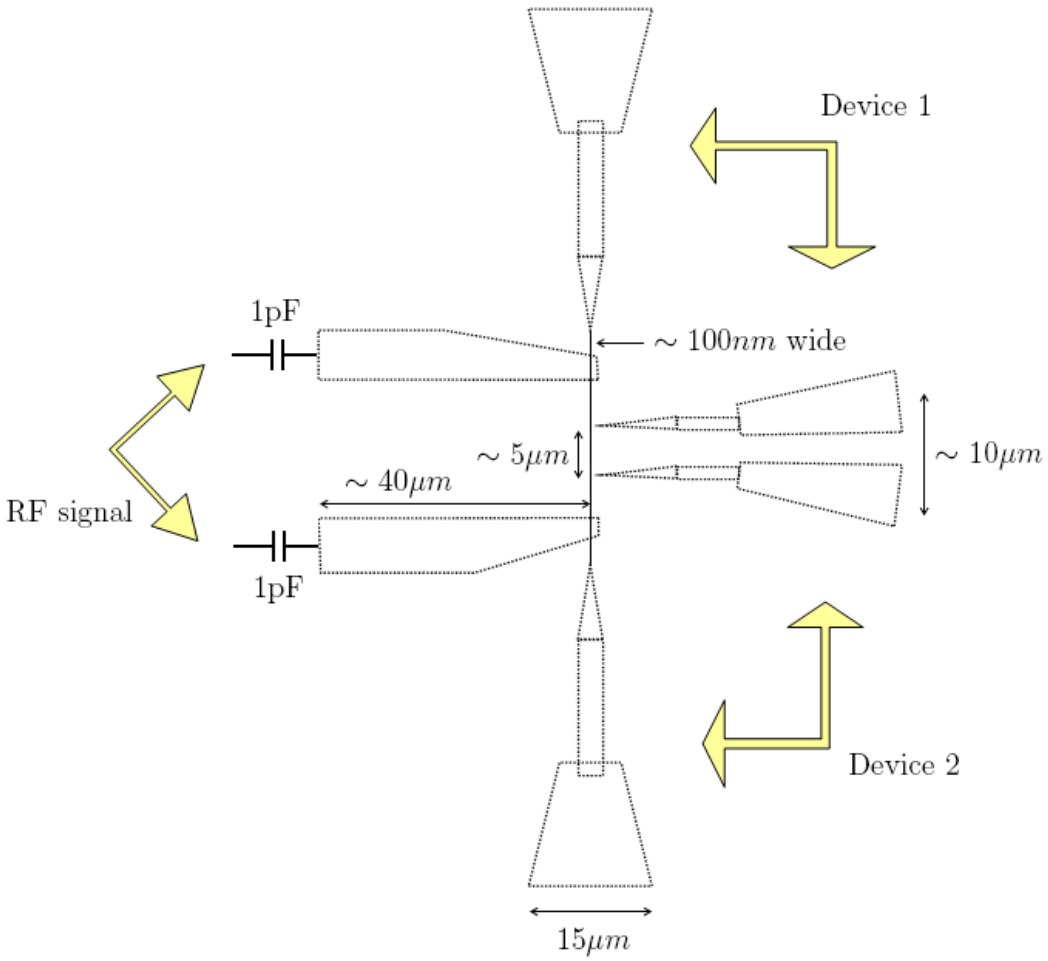

Figure 38: New device geometry to allow RF pulses to be applied. For illustration purposes, some approximate dimensions are shown (not scaled). The thin wire in the center is a $100nm$ line.

6.1.2 Preliminary Results

First, we performed an attempt experiment to observe the effects (if any) of microwave pulses in our samples. A double-pulse (two square pulses in series) was applied via "bursts" triggered by the FG. For each value of spacing between the two pulses, ranging from $10\mu s$ to $1ms$, a full histogram of the switching fields was obtained using LabView. The resulting histograms are shown in Figures 39 and 40.

From the histogram corresponding to the largest pulse spacing, $1,000\mu s$, there is clear switching field distribution around $\sim -0.21T$, suggesting that the magnetization in the particle fully relaxes between the first and the second pulse. For shorter pulse spacings, the magnetization becomes less stable, and an alternative switching field appears, widely distributed at first. As the pulse spacing gets shorter, the presence of this alternative switching field becomes more noticeable. At a spacing of $10\mu s$, the second switching field distribution becomes dominant around $-0.51T$. These histograms were taken at one sweeping direction of the magnetic field (decreasing field), with only one switching event happening at either one or the other field distributions.

From this result, it is clear that the RF pulses definitely have an effect on the hysteresis loop. It turns out that the pulse duration of $1\mu s$, used for this experiment, is long enough to induce heating at the sample, affecting the observed switching field distribution. This was realized after performing further tests using a train of much shorter single pulses ($\sim 3ns$) with different spacings. By measuring I-V curves under different applied pulse spacings, and comparing it with another set of I-V curves measured at different temperatures, it was possible to estimate the critical pulse spacing, below which, heating due the RF signal does not happen. Figure 41 shows the temperature dependence of I-V curves.

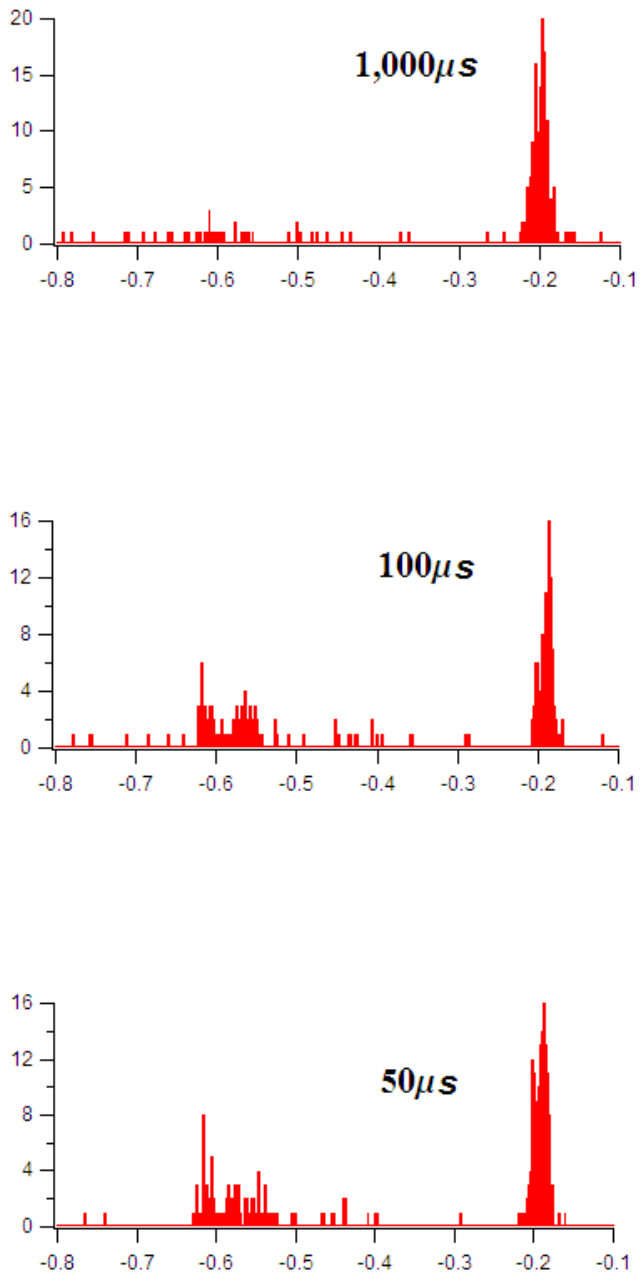

Figure 39: Switching field histograms for different time spacings between an applied double-pulse. Spacings vary from $1ms$ to $50\mu s$

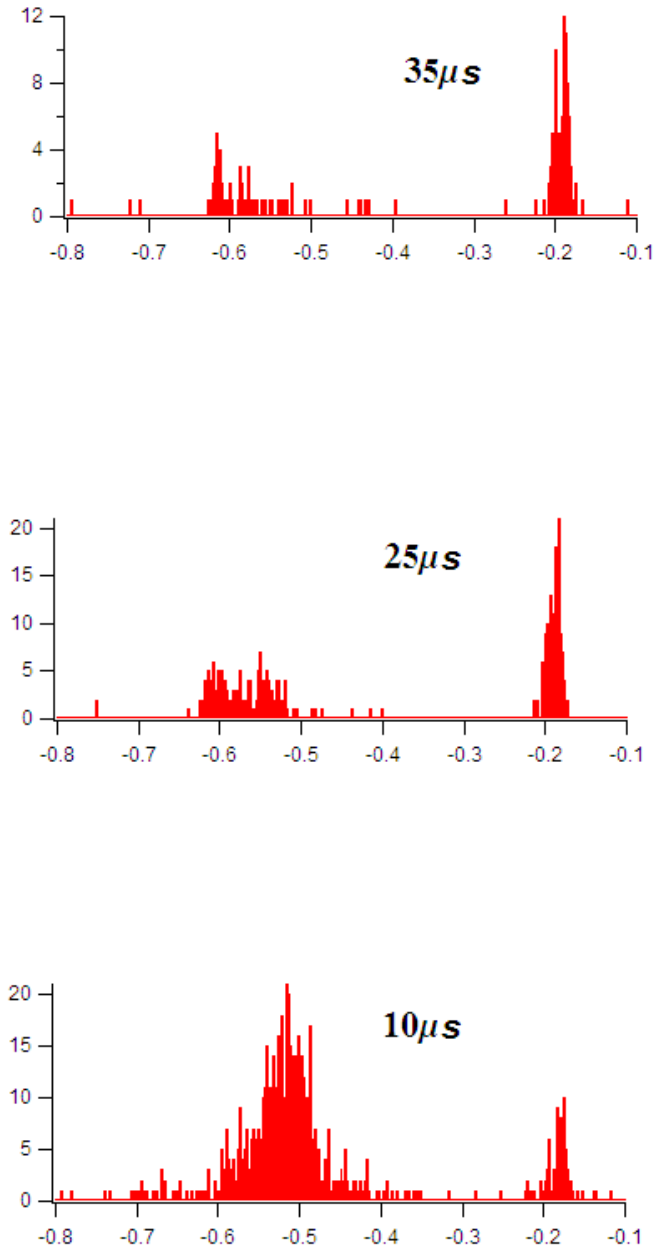

Figure 40: Switching field histograms for different time spacings between an applied double-pulse. Spacings vary from $35\mu s$ to $10\mu s$

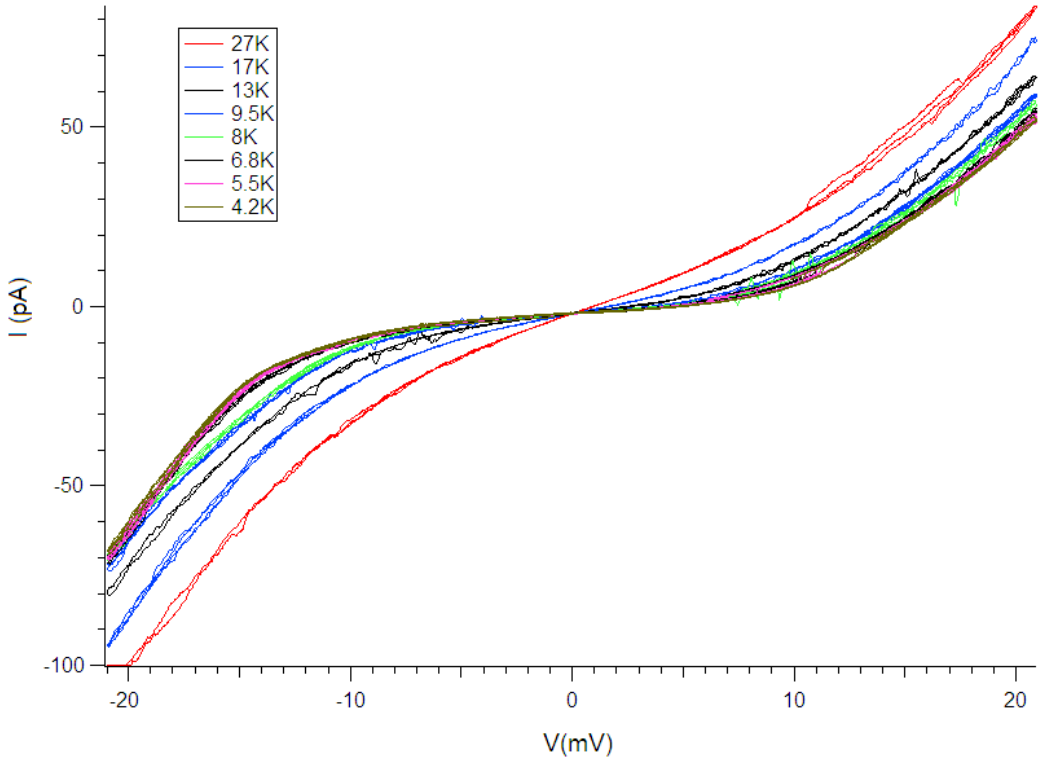

Figure 41: Temperature dependence of I-V curves. By comparing changes in slope due to different temperatures and pulse spacings, it is possible to determine if heating due to the RF signal is taking place.

6.2 Conclusions

The work presented in this thesis shows how tunneling spectroscopy techniques can be applied to metallic nanoparticles to obtain detailed information about fundamental physical processes in such small length scales. At low temperatures, the discrete character of the energy spectrum, allows the study of spin-polarized current via single"electron-in-a-box" levels, as well as its effects on transport properties, in the presence of external magnetic fields.

In FNF structures, the spin-valve effect was shown to be affected by a magnetic field applied perpendicular to the magnetization of the leads, in agreement with a simple model based on a basis transformation, from spin states in the particle to states in the ferromagnetic leads. As a consequence, the current through the particle in the parallel magnetization configuration, is weakly affected by the perpendicular field, but shows a much stronger dependence in the anti-parallel configuration. The variety of observations, indicate suppression of spin-precession in the particle, with spins in the particle accumulating along the direction of the local magnetic field. The spin-accumulation mechanism is responsible for magnetoresistance in FNN devices as well. It was shown that magnetoresistance arises from the magnetic field dependence of the angle between the accumulated magnetic moment and the magnetization. This simple mechanism needs to be considered when interpreting results in spintronics involving discrete energy levels.

In contrast to normal metal particles, ferromagnetic nanoparticles show a much more complex energy level structure, due to variations in the anisotropy energies as a function of magnetic field and interactions between electronic and magnetic excitations, which are just beginning to be unraveled. From measurements of the switching field as a function of temperature and bias voltage, it is possible to study magnetic relaxation and its relations with the coupling strength with the environment. By using microwave pulses as a complementary probing technique, more accurate quantitative results about the magnetization dynamics of the system, such as magnetic damping and relaxation times, will become soon available.

APPENDIX A

SOURCES OF MAGNETIC DAMPING

This appendix aims to present a few derivations and discussions about possible mechanisms of magnetic damping. It is not intended to give a detailed analysis, but to provide a brief description about the physical origins of each process, as well as to point out relevant references from the literature.

A.1 Interaction with Nuclear Spins

The magnetization of a Co particle is coupled to the its nuclear spins (7/2) via the hyperfine interaction. The discrete electron-in-a-box levels and energy conservation impose constraints on the magnetization relaxation processes. In the relaxation caused by hyperfine scattering, the magnon energy is much larger than the nuclear-spin energy. The energy difference is not compensated by the change in electron kinetic energy, making the hyperfine scattering inefficient, similar to the behavior in GaAs quantum dots [32]. The hyperfine field at the nuclei was measured by nuclear magnetic resonance (NMR) in Co [37]. The NMR frequency ($213.1MHz$) is much smaller than the typical magnon frequency $10^9 - 10^{10}$Hz, causing energy mismatch between the nuclear and magnon energies, which prohibits direct electron-nuclear flip-flops. In GaAs quantum dots in a magnetic field, it was shown that the electron-spin relaxation time is very long ($> 10ms$) in a magnetic field above $0.1T$ [41]. In GaAs quantum dots, the energy mismatch is caused by the difference between the electron and the nuclear Zeeman splitting, while in Co nanoparticles it is caused by the difference between the magnon energy and the nuclear Zeeman splitting in the hyperfine field at the nuclei.

A.2 Near-Field Magnetic Noise and Eddy-Currents

The magnetization of the particle is coupled to the near-field magnetic noise, generated by the Johnson-noise currents in the leads. In addition, magnons can emit eddy currents in the leads, via the magnetic dipole field generated by the magnetic moment of the particle. These two damping mechanisms are similar and we find that they have the same damping contribution. First we consider near-field magnetic noise at the particle. The lead is modeled assuming an infinite slab of thickness t, while the center of the particle is at distance d from the slab surface. The conductivity of the leads at low temperature was measured from the residual resistance ratio, $\sigma = 1 \cdot 10^7/\Omega m$. The corresponding mean free path is $3.5nm$ The magnetic field spectral density in the vicinity of the slab was calculated by Varpula and Poutanen [89]. The skin depth at the magnon frequency, $\sim 1\mu m$, is much larger than any other length scale in the problem. The spectral density differs by a factor of 2 between the magnetic field direction parallel and perpendicular to the slab. The average spectral density, defined as $< B^2 >= (< B_x^2 > + < B_y^2 > + < B_z^2 >)/3$, is:

$$< B^2 >= \frac{\mu_0^2 \sigma k_B T}{12\pi} \left(\frac{1}{d} - \frac{1}{d+t} \right). \tag{20}$$

This expression is compared with the fluctuating field spectral density in the LLG-equation, calculated in Ref. [46]. It follows that the near-field magnetic noise has a magnetic damping:

$$\alpha = \frac{\sigma(\mu_0 g \mu_B)^2 S_0}{24\pi\hbar} \left(\frac{1}{d} - \frac{1}{d+t} \right). \tag{21}$$

A precessing magnetic moment in the particle creates a time dependent magnetic field, which induces an electric field, resulting in dissipative eddy-currents. In our Co particles, the electronic level spacing is much larger than the magnon energy, thus electrons in the particle cannot be excited by magnons. But the electrons in the leads can still be excited, via the dipole magnetic field. In a quantum mechanical description, the magnon relaxation rate can be obtained by using the Fermi golden rule. It involves finding the matrix elements between diffusive electron wave-functions in the leads. Alternatively, one can calculate the eddy current power dissipation P, classically. The relaxation rate will be obtained by making a correspondence $P = n\hbar\omega/T_1$, where n is the number of magnons (the magnetic

energy of the particle is $n\hbar\omega$). The magnitude of the precessing component of the magnetic moment is given by $M' = g\mu_B\sqrt{2S_0 n}$. The center of the particle is at a distance d from the slab, as described above. The eddy-current dissipation is calculated for the precession axis both perpendicular and parallel to the slab, and the result is averaged over three orthogonal directions.

The magnetic dipole field generated by the particle decays at a length scale comparable to the particle diameter, much smaller than the skin depth. We use $\vec{B} = curl(\vec{A})$ for the precessing magnetic field, $\vec{E} = -\partial\vec{A}/\partial t$ for the induced electric field , and

$$\vec{A} = \frac{\mu_0}{4\pi}\frac{\vec{M}' \times \vec{r}}{r^3},$$

for the the vector potential at point $\vec{r}$, where $\vec{r}$ is measured from the center of the particle. We calculate the dissipation power $P = \int dV\sigma E^2$ by integrating over the entire slab volume. The resulting power is

$$P = \frac{\sigma(\mu_0\omega M')^2}{24\pi}\left(\frac{1}{d} - \frac{1}{d+t}\right). \tag{22}$$

Using the correspondence $P = n\hbar\omega/T_1$, we obtain the damping parameter $\alpha = 1/2\omega T_1$. The result for α is identical to that given by Eq. 21. A possible scenario is that the equivalence of the two damping parameters is not a coincidence, but a consequence of the fluctuation dissipation theorem, which relates eddy current noise in thermal equilibrium, with eddy current dissipation out of thermal equilibrium.

The divergence in damping at $d \to 0$ arises from the assumption that the dissipation is local, which is implicit in the integral $\int dV\sigma E^2$. The dissipation becomes non-local at distances r from the particle smaller than the mean free path, l. The induced electric field varies at a length scale comparable to the particle size, smaller than l, while the electrons dissipate their kinetic energy at a length scale, l. A similar situation is found in the treatment of the anomalous skin effect. Nonlocal dissipation can be taken into account by excluding the region in the slab with distances from the particle $< l$. Thus, for thick slabs, the physically sensible estimate is:

$$\alpha = \frac{\sigma(\mu_0 g\mu_B)^2 S_0}{24\pi\hbar l}. \tag{23}$$

The magnetic damping is independent of frequency and proportional to S_0, meaning that α scales with the particle's volume, which is a possible reason why the extrinsic eddy-current/magnetic-noise damping becomes very weak in very small particles.

A.3 Magneto-Elastic Damping

The magnons in the particle are coupled to the phonon bath via the magneto-elastic interaction. This interaction can annihilate a magnon while creating a degenerate acoustic phonon. The magneto-elastic damping in various sample geometries has been calculated previously [86, 68, 81]. In our samples, we consider magneto-elastic coupling between the magnons and the substrate phonons. The phonon wavelength at the magnon frequency is $\sim$ 100nm, much larger than the particle size. The magneto-elastic coupling Hamiltonian is

$$H' = \frac{VB_2}{S_0^2} \sum_{i,j=1}^{3} e_{ij} S_i S_j,$$

where $e_{ij} = (\partial u_i/\partial x_j + \partial u_j/\partial x_i)/2$ is the strain, u_i is the displacement component, and B_2 is the magneto-elastic coefficient, B_2 =2.6$\cdot$ 10^7 J/m^3 in Co [13], and V is the particle volume. The terms S_iS_j change the magnon number. We consider only shear waves as in Ref. [86], and expand the displacement in terms of the phonon operators [2]:

$$\vec{u}(\vec{r}) = \sum_{\vec{k}s} \sqrt{\frac{\hbar}{2\rho V_s \omega_s(\vec{k})}} \left(a_{\vec{k}s} + a^{\dagger}_{-\vec{k}s}\right) \vec{\epsilon}_s(\vec{k}) e^{i\vec{k}\vec{r}},$$

where ρ is the substrate density, $\omega_s(\vec{k}) = ck$ is the phonon frequency, c is the speed of sound in the substrate, $\epsilon_s(\vec{k})$ is the phonon polarization vector, and V_s is the substrate volume. The relaxation time is obtained using the Fermi golden rule,

$$\frac{1}{T} = \frac{2\pi}{\hbar} | < S_0, S_0 - n | H' | S_0, S_0 - n + 1 > |^2 D(\omega),$$

where $D(\omega)$ is the phonon density of states at the magnon frequency. The calculation leads to:

$$\frac{1}{T} \sim n \frac{\omega^3 (VB_2)^2}{\hbar \rho c^5 S_0} = \frac{n}{T_1}.$$

The magnon relaxation rate $1/T_1$ is proportional to the cube of the frequency; a factor of ω^2 comes from the phonon density of states, and another factor of ω comes from the square of

the deformation potential matrix element, $e_{ij} \sim uk \sim \sqrt{\omega}$. The majority of the substrate in our sample is SiO_2. Substituting for $\rho = 2.6 \cdot 10^3 \mathrm{kg/m}^3$ and c =5700m/s, we obtain a weak damping parameter which also scales with the particle's volume, $\alpha = 1/2\omega T_1 \sim 10^{-9} - 10^{-8}$.

A.4 Paramagnetic Impurities

Paramagnetic impurities may be present in the particle's surrounding oxide, loosely coupled to the particle spin. In this case, magnon energy can dissipate through those impurities, via the exchange interaction or dipole-dipole interaction. Such an active paramagnetic impurity would have to be very well separated from the particle. The exchange coupling between the impurity and the particle spin must be less than the magnon energy $\sim 10\mu eV$, otherwise there would be a prohibiting energy mismatch. The exchange interaction between the impurity and the particle spin decreases exponentially with distance, and we estimate that the distance between the impurity and the magnetic particle must be $> 1nm$ to decouple.

Let us examine possible origins of the decoupled paramagnetic impurities. In particular, the Co surface might be oxidized, creating the impurities in the Co oxide. However, in order to decouple the impurity from the metallic core, the oxide would have to be $\sim 1nm$ thick. Our hysteresis loops are very symmetric about zero magnetic field, indicating that the oxide layer is not present. If the Co surface was oxidized with a thick oxide, a strong exchange bias effect would be noticeable, resulting in strong asymmetry, contrary to our measurements. Thus, oxidation of the surface must be weak, if any. It cannot account for paramagnetic impurities at 1nm distance from the core.

A.5 Dipole-Dipole Coupling

The particle magnetization may interact with the magnetization of neighboring particles, via the magnetic dipole-dipole interaction. The effects of dipole-dipole interactions between the particles have been observed in hysteresis loops of a Co particle, by Daniel Ralph's group. They observed that the magnetic field from one particle can shift the hysteresis loop of another particle [38]. There is a small number of particles in significant magnetic coupling with the measured particle. Those particles would have to match the measured particle's

magnon energy in order to cause magnon dissipation. Due to the difference in particle size, shape, and local environment, this energy match is very improbable to take place.

REFERENCES

[1] Agam, O., Wingreen, N. S., Altshuler, B. L., Ralph, D. C., and Tinkham, M., "Chaos, interactions, and nonequilibrium effects in the tunneling resonance spectra of ultrasmall metallic particles," *Phys. Rev. Lett.*, vol. 78, p. 1956, 1997.

[2] Ashcroft, N. W. and Mermin, N. D., *Solid State Physics*. McGraw-Hill advanced physics monograph series, Philadelphia : Saunders College, 1976.

[3] Averin, D. V., Korotkov, A. N., and Likharev, K. K., "Theory of single-electron charging of quantum wells and dots," *Phys. Rev. B*, vol. 44, p. 6199, 1999.

[4] Averin, D. V. and Likharev, K. K. in *Mesoscopic Phenomena in Solids* (Altshuler, B. L., Lee, P. L., and Webb, R. A., eds.), p. 169, Elsevier and Amsterdam, 1991.

[5] Barnas, J. and Fert, A., "Magnetoresistance oscillations due to changing effects in double ferromagnetic tunnel junctions," *Phys. Rev. Lett.*, vol. 80, p. 1058, 1998.

[6] Barnas, J. and Weymann, I., "Spin effects in single-electron tunnelling," *Jour. Phys. Cond. Matt.*, vol. 20, p. 423202, 2008.

[7] Bean, C. P. *J. Appl. Phys.*, vol. 26, p. 1381, 1955.

[8] Bedanta, S. and Kleemann, W. *J. Phys. D*, vol. 42, p. 013001, 2009.

[9] Beenakker, C. W. J., "Theory of coulomb-blockade oscillations in the conductance of a quantum dot," *Phys. Rev. B*, vol. 44, p. 1646, 1991.

[10] Bernand-Mantel, A., Seneor, P., Bouzehouane, K., Fusil, S., Deranlot, C., Petroff, F., and Fert, A., "Anisotropic magneto-coulomb effects and magnetic single-electron-transistor action in a single nanoparticle," *Nat. Phys.*, vol. 5, p. 920, 2009.

[11] Bernand-Mantel, A., Seneor, P., Lidgi, N., Munoz, M., Cros, V., Fusil, S., Bouzehouane, K., Deranlot, C., Vaures, A., Petroff, F., and Fert, A., "Evidence for spin injection in a single metallic nanoparticle: A step towards nanospintronics," *Appl. Phys. Lett.*, vol. 89, p. 062502, 2006.

[12] Birk, F. T., Malec, C. E., and Davidovic, D., "Spin-polarized electron tunneling through an aluminum nanoparticle in a noncollinear magnetic field," *Phys. Rev. B*, vol. 79, p. 245425, 2009.

[13] Bochi, G., Song, O., and O'Handley, R. C., "Surface magnetoelastic coupling coefficients in single-crystal fcc co thin films," *Phys. Rev. B*, vol. 50, pp. 2043–2046, 1994.

[14] Bonet, E., Deshmukh, M. M., and Ralph, D. C., "Solving rate equations for electron tunneling via discrete quantum states," *Phys. Rev. B*, vol. 65, p. 045317, 2002.

[15] Brataas, A., Nazarov, Y. V., Inoue, J., and Bauer, G. E. W., "Non-equilibrium spin accumulation in ferromagnetic single-electron transistors," *European physical journal B*, vol. 9, p. 421, 1999.

[16] Brataas, A., Nazarov, Y. V., Inoue, J., and Bauer, G. E. W., "Spin accumulation in small ferromagnetic double-barrier junctions," *Phys. Rev. B*, vol. 59, p. 93, 1999.

[17] Braun, M., Konig, J., and Martinek, J., "Theory of transport through quantum-dot spin valves in the weak-coupling regime," *Phys. Rev. B*, vol. 70, p. 195345, 2004.

[18] Braun, M., Konig, J., and Martinek, J., "Hanle effect in transport through quantum dots coupled to ferromagnetic leads," *Europhys. Lett.*, vol. 72, pp. 294–300, 2005.

[19] Brouwer, P. W., Waintal, X., and Halperin, B. I., "Fluctuating spin g-tensor in small metal grains," *Phys. Rev. Lett.*, vol. 85, p. 369, 2000.

[20] Brown, W. F. *Phys. Rev.*, vol. 130, p. 1677, 1963.

[21] Burkard, G., Engel, H. A., and Loss, D., "Spintronics and quantum dots for quantum computing and quantum communication," *Fortschr. Phys.*, vol. 48, p. 965, 2000.

[22] Buttiker, M. and Landauer, R., "Traversal time for tunneling," *IBM J. Res. Develop.*, vol. 30, p. 451, 1986.

[23] Canali, C. M. and MacDonald, A. H., "Theory of tunneling spectroscopy in ferromagnetic nanoparticles," *Phys. Rev. Lett.*, vol. 85, pp. 5623–5626, 2000.

[24] Cehovin, A., Canali, C. M., and MacDonald, A. H., "Elementary excitations of ferromagnetic metal nanoparticles," *Phys. Rev. B*, vol. 68, p. 014423, 2003.

[25] Chakraverty, S. and Bandyopadhyay, M., "Coercivity of magnetic nanoparticles: a stochastic model," *Journal of Physics: Condensed Matter*, vol. 19.

[26] Chappert, C. and Barthelemy, A. in *Nanoscience - nanotechnologies and nanophysics* (Dupas, C., Houdy, P., and Lahmani, M., eds.), 2004.

[27] Coffey, W. T. and Fannin, P. C. *J. Phys.:Condens. Matter*, vol. 14, p. 3677, 2002.

[28] Coffey, W. T., Kalmykov, Y. P., and Waldron, J. T. *World Scientific Series in Contemporary Chemical Physics*, vol. 14, 2004.

[29] Deshmukh, M. M., Kleff, S., Gueron, S., Bonet, E., Pasupathy, A. N., von Delft, J., and Ralph, D. C., "Magnetic anisotropy variations and nonequilibrium tunneling in a cobalt nanoparticle," *Phys. Rev. Lett*, vol. 87, p. 226801, 2001.

[30] Deshmukh, M. M. and Ralph, D. C., "Using single quantum states as spin filters to study spin polarization in ferromagnets," *Phys. Rev. Lett*, vol. 89, p. 266803, 2002.

[31] Dolan, G. J., "Offset masks for lift-off photoprocessing," *Appl. Phys. Lett.*, vol. 31, p. 337, 1977.

[32] Erlingsson, S. I., Nazarov, Y. V., and Fal'ko, V. I., "Nucleus-mediated spin-flip transitions in gaas quantum dots," *Phys. Rev. B*, vol. 64, p. 195306, 2001.

[33] Ernult, F., Yakushiji, K., Mitani, S., and Takanashi, K., "Spin accumulation in metallic nanoparticles," *J. Phys. Cond. Mat.*, vol. 19, p. 1652140, 2007.

[34] Feynman, R. P., "Quantum mechanical computers," *Found. Physics*, vol. 16, p. 507, 1986.

[35] Garg, A., "Escape-field distribution for esacape from a metastable potential well subject to a steadily increasing bias field," *Phys. Rev. B*, vol. 51, pp. 15592–15595, 1995.

[36] Giaever, I. and Zeller, H. R., "Superconductivity of small tin particles measured by tunneling," *Phys. Rev. Lett.*, vol. 20, pp. 1504–1507, 1968.

[37] Gossard, A. C. and Portis, A. M., "Observation of nuclear resonance in a ferromagnet," *Phys. Rev. Lett.*, vol. 3, pp. 164–166, 1959.

[38] Gueron, S., Deshmukh, M. M., Myers, E. B., and Ralph, D. C., "Tunneling via individual electronic states in ferromagnetic nanoparticles," *Phys. Rev. Lett.*, vol. 83, p. 4148, 1999.

[39] Gunther, L. and Barbara, B., "Quantum tunneling across a domain-wall junction," *Phys. Rev. B*, vol. 49, pp. 3926–3933, 1994.

[40] Halperin, W. P., "Quantum size effects in metal particles," *Rev. Mod. Phys.*, vol. 58, p. 533, 1986.

[41] Hanson, R., Witkamp, B., Vandersypen, L., van Beveren, L. W., Elzerman, J., and Kouwenhoven, L., "Zeeman energy and spin relaxation in a one-electron quantum dot," *Phys. Rev. Lett.*, vol. 91, 2003.

[42] Hatzakis, M., "Electron resists for microcircuit and mask production," *J. Electrochem. Soc.*, vol. 116, p. 1033, 1969.

[43] Jedema, F. J., Filip, A. T., and van Wees, B. J., "Electrical spin injection and accumulation at room temperature in an all-metal mesoscopic spin valve.," *Nature*, vol. 410, p. 345, 2001.

[44] Jedema, F. J., Heersche, H. B., Filip, A. T., Baselmans, J. J. A., and van Wees, B. J., "Electrical detection of spin precession in a metallic mesoscopic spin valve.," *Nature*, vol. 416, p. 713, 2002.

[45] Jensen, A., Hauptmann, J. R., Nygard, J., and Lindelof, P., "Magnetoresistance in ferromagnetically contacted single-wall carbon nanotubes," *Phys. Rev. B*, vol. 72, p. 035419, 2005.

[46] Johnson, M. and Silsbee, R. H., "Interfacial charge-spin coupling: injection and detection of spin magnetization in metals.," *Phys. Rev. Lett.*, vol. 55, p. 1790, 1985.

[47] Jones, D. H. and Srivastava, K. K. P. *J. Magn. Magn. Mat.*, vol. 78, p. 320, 1989.

[48] Jr., R. J. S., Byers, J. M., Osofsky, M. S., Nadgorny, B., Ambrose, T., Cheng, S. F., Broussard, P. R., Tanaka, C. T., Nowak, J., Moodera, J. S., Barry, A., and Coey, J. M. D., "Measuring the spin polarization of a metal with a superconducting point contact," *Science*, vol. 282, p. 85, 1998.

[49] Julliere, M., "Tunnelling between ferromagnetic films," *Phys. Lett. A*, vol. 54, pp. 225–226, 1975.

[50] Kawakami, R. K., McCreary, K., and Li, Y. in *Nanoelectronics and Photonics: From Atoms to Materials, Devices, and Architectures* (Korkin, A. and Rosei, F., eds.), Springer, 2008.

[51] Kirk, K. J. and andC. D. W. Wilkinson, J. N. C., "Switching fields and magnetostatic interactions of thin film magnetic nanoelements," *Appl. Phys. Lett.*, vol. 71, p. 539, 1997.

[52] Kittel, C., *Introduction to solid state physics*. John Wiley & Sons, Inc., 1953.

[53] Kleff, S. and von Delft, J., "Nonequilibrium excitations in ferromagnetic nanoparticles," *Phys. Rev. B*, vol. 65, p. 214421, 2002.

[54] Kleff, S., von Delft, J., Deshmukh, M. M., and Ralph, D. C., "Model for ferromagnetic nanograins with discrete electronic states," *Phys. Rev. B*, vol. 64, p. 220401, 2001.

[55] Knobel, M., Nunes, W. C., Socolovsky, L., Biasi, E. D., Vargas, J. M., and Denardin, J. C. *J. Nanosci. Nanotechnol.*, vol. 8, p. 2836, 2008.

[56] Konig, J. and Martinek, J., "Interaction-driven spin precession in quantum-dot spin valves," *Phys. Rev. Lett.*, vol. 90, p. 166602, 2003.

[57] Kouwenhoven, L. P., Marcus, C., McEuen, P., Tarucha, S., Westervelt, R., and Wingreen, N. in *Mesoscopic Electron Transport* (Kouwenhoven, L. P., Sohn, L. L., and Schon, G., eds.), p. 549, Elsevier and Amsterdam, 1997.

[58] Krause, S., Herzog, G., Stapelfeldt, T., Berbil-Bautista, L., Bode, M., Vedmedenko, E. Y., and Wiesendanger, R., "Magnetization reversal of nanoscale islands: How size and shape affect the arrhenius prefactor," *Phys. Rev. Lett.*, vol. 103, p. 127202, 2009.

[59] Kuo, W. and Chen, C. D., "Gate-controlled spin polarized current in ferromagnetic single electron transistors," *Phys. Rev. B*, vol. 65, p. 104427, 2002.

[60] Likharev, K. K., "Correlated discrete transfer of single electrons in ultrasmall tunnel junctions," *IBM J. Res. Develop.*, vol. 32, pp. 144–158, 1988.

[61] Lopez-Diaz, L. and Torres, L. *Phys. Rev. B*, vol. 65, p. 224406, 2002.

[62] Loss, D. and DiVincenzo, D. P., "Quantum computation with quantum dots," *Phys. Rev. A*, vol. 57, p. 120, 1998.

[63] Lounasmaa, O. V., *Experimental principles and methods below 1K.* Academic Press, London, 1974.

[64] Mailly, D. and Vieu, C. in *Nanoscience - nanotechnologies and nanophysics* (Dupas, C., Houdy, P., and Lahmani, M., eds.), 2004.

[65] Majumdar, K. and Hershfield, S., "Magnetoresistance of the double-tunnel-junction coulomb blockade with magnetic metals," *Phys. Rev. B*, vol. 57, p. 11521, 1998.

[66] Matveev, K. A., Glazman, L. I., and Larkin, A. I., "g-factors of discrete levels in nanoparticles," *Phys. Rev. Lett.*, vol. 85, p. 2789, 2000.

[67] M.Bauer, Fassbender, J., and Hillebrands, B., "Switching behavior of a stoner particle beyound the relaxation time limit," *Phys. Rev. B*, vol. 61, p. 3410, 2000.

[68] McMichael, R. D. and Kunz, A., "Calculation of damping rates in thin inhomogeneous ferromagnetic films due to coupling to lattice vibrations," *J. Appl. Phys.*, vol. 91, pp. 8650–8652, 2002.

[69] Meservey, R. and Tedrow, P. M., "Spin-polarized electron tunneling," *Phys. Rep.*, vol. 238, pp. 173–243, 1994.

[70] Michalak, L. and Canali, C. M., "Electron-magnon coupling and nonlinear tunneling transport in magnetic nanoparticles," *Phys. Rev. Lett.*, vol. 97, p. 096804, 2006.

[71] Mitani, S., Nogi, Y., Wang, H., Yakushiji, K., Ernult, F., and K, K. T., "Current-induced tunnel magnetoresistance due to spin accumulation in au nanoparticles," *Appl. Phys. Lett.*, vol. 92, p. 152509, 2008.

[72] Moodera, J. S. and Mathon, G., "Spin polarized tunneling in ferromagnetic junctions," *Journal of Magnetism and Magnetic Materials*, vol. 200, pp. 248–273, 1999.

[73] Morrish, A. H., *The physical principles of magnetism.* 1965.

[74] Néel, L. *Compt. rend. (Paris)*, vol. 228, p. 604, 1949.

[75] Ono, K., Shimada, H., Kobayashi, S., and Outuka, Y., "Magnetoresistance of ni/nio/co small tunnel junctions in coulomb blockade regime," *Journal of the physical society of Japan*, vol. 65, p. 3449, 1996.

[76] Ono, K., Shimada, H., and Outuka, Y., "Enhanced magnetic valve effect and magneto-coulomb oscillations in ferromagnetic single electron transistor," *Journal of the physical society of Japan*, vol. 66, p. 1261, 1997.

[77] Park, B. G., Wunderlich, J., Williams, D. A., Joo, S. J., Jung, K. Y., Shin, K. H., Olejník, K., Shick, A. B., and Jungwirth, T., "Tunneling anisotropic magnetoresistance in multilayer-$(co/pt)/alo_x/pt$ structures," *Phys. Rev. Lett.*, vol. 100, no. 8, p. 087204, 2008.

[78] Parkin, S. S. P., Jiang, X., Kaiser, C., Panchula, A., Roche, K., and Samant, M., "Magnetically engineered spintronic sensors and mameory," *Proc. IEEE*, vol. 91, p. 661, 2003.

[79] Petta, J. R., Johnson, A. C., Taylor, J. M., Laird, E. A., A, A. Y., Lukin, M. D., Marcus, C. M., Hanson, M. P., and Gossard, A. C., "Coherent manipulation of coupled electron spins in semiconductor quantum dots," *Science*, vol. 309, pp. 2180–2184, 2004.

[80] Ralph, D. C., Black, C. T., and Tinkham, M., "Spectroscopic measurements of discrete electronic states in single metal particles," *Phys. Rev. Lett.*, vol. 74, p. 3241, 1995.

[81] Rossi, E., Heinonen, O. G., and MacDonald, A. H., "Dynamics of magnetization coupled to a thermal bath of elastic modes," *Phys. Rev. B*, vol. 72, p. 174412, 2005.

[82] Schelp, L. F., Fert, A., Fettar, F., Holody, P., Lee, S. F., Maurice, J. L., Petroff, F., and Vaures, A., "Spin-dependent tunneling with coulomb blockade," *Phys. Rev. B*, vol. 56, p. R5747, 1997.

[83] Seneor, P., Bernand-Mantel, A., and Petroff, F., "Nanospintronics: when spintronics meets single electron physics," *J. Phys.: Condens. Matter*, vol. 19, p. 165222, 2007.

[84] Shinde, S. R., Ogale, S. B., Higgins, J. S., Zheng, H., Millis, A. J., Kulkarni, V. N., Ramesh, R., Greene, R. L., and Venkatesan, T., "Co-occurrence of superparamagnetism and anomalous hall effect in highly reduced cobalt-doped rutile $tio_{2-\delta}$ films," *Phys. Rev. Lett.*, vol. 92.

[85] Stoner, E. C. and Wohlfarth, E. P. *Phil. Trans. Roy. Soc. (London)*, vol. A-240, p. 599, 1948.

[86] Suhl, H., "Theory of the magnetic damping constant," *IEEE Trans. Magn.*, vol. 34, pp. 1834–1838, 1998.

[87] Takahashi, S. and Maekawa, S., "Effect of coulomb blockade on magnetoresistance in ferromagnetic tunnel junctions," *Phys. Rev. Lett.*, vol. 80, p. 1758, 1998.

[88] van der Molen, S. J., Tombros, N., and van Wees, B. J., "Magneto-coulomb effect in spin-valve devices," *Phys. Rev. B*, vol. 73, p. 220406(R), 2006.

[89] Varpula, T. and Poutanen, T., "Magnetic field fluctuations arising from thermal motion of electric charge in conductors," *J. Appl. Phys.*, vol. 55, pp. 4015–4021, 1984.

[90] Wei, Y. G., Malec, C. E., and Davidovic, D., "Saturation of spin-polarized current in nanometer scale aluminum grains," *Phys. Rev. B*, vol. 76, p. 195327, 2007.

[91] Wei, Y. G., Malec, C. E., and Davidovic, D., "Modeling electron-spin accumulation in a metallic nanoparticle," *Phys. Rev. B*, vol. 78, p. 035435, 2008.

[92] Wernsdorfer, W., Orozco, E. B., Hasselbach, K., Benoit, A., Barbara, B., Loiseau, N. D. A., Pascard, H., and Mailly, D., "Experimental evidence of the neel-brown model of magnetization reversal," *Phys. Rev. Lett.*, vol. 78, pp. 1791–1794, 1997.

[93] Wesselinowa, J. M. and Apostolova, I., "Size and anisotropy effects on static and dynamic properties of ferromagnetic nanoparticles," *Journal of Physics: Condensed Matter*, vol. 19, no. 21, p. 216208, 2007.

[94] Wetzels, W., Bauer, G. E. W., and Grifoni, M., "Exchange effects on electron transport through single-electron spin-valve transistors," *Phys. Rev. B*, vol. 74, p. 224406, 2006.

[95] Weymann, I. and Barnas, J., "Effect of intrinsic spin relaxation on the spin-dependent cotunneling transport through quantum dots," *Phys. Rev. B*, vol. 73, p. 205309, 2006.

[96] Weymann, I., Konig, J., Martinek, J., Barnas, J., and Schon, G., "Tunnel magnetoresistance of quantum dots coupled to ferromagnetic leads in the sequential and cotunneling regimes," *Phys. Rev. B*, vol. 72, p. 115334, 20053.

[97] Wolf, S. A., Awschalom, D. D., Buhrman, R. A., Daughton, J. M., von Molnar, S., Roukes, M. L., Chtchelkanova, A. Y., and Treger, D. M., "Spintronics: A spin-based electronics vision for the future," *Science*, vol. 294, p. 1488, 2001.

[98] Zutic, I., Fabian, J., and Sarma, S. D., "Spintronics: Fundamentals and applications," *Rev. Mod. Phys.*, vol. 76, p. 323, 1969.

VITA

Felipe Tijiwa Birk grew up in São Paulo, Brazil, on September 26^{th} of 1979. After graduating from the technical High School, ETE "Lauro Gomes" in 1997, with a degree in electronics, he spent three years in the work force. He then decided to continue his education, moving to the city of Campinas, where he obtained his B.S. degree in Physics from "Universidade Estadual de Campinas" (Unicamp) in 2005. During his stay at Unicamp, he met a young lady named Sara and they have been married since 2003. After graduation, they moved to the US, in 2005, where he joined the School of Physics at Georgia Tech in the Fall of 2006.